Study and Characterization of Nano-structured Electron Sources Using Photoemission Electron Microscope

by

Alimohammed Samina Hussain Kachwala

A Dissertation Presented in Partial Fulfillment
of the Requirements for the Degree
Doctor of Philosophy

Approved April 2024 by the
Graduate Supervisory Committee:

Siddharth Karkare, Chair
Robert Kaindl
Robert Nemanich
Maxim Sukharev

ARIZONA STATE UNIVERSITY

August 2024

ABSTRACT

Photoinjectors, renowned for producing electron beams of unparalleled brightness, are pivotal to numerous high-impact scientific endeavors, including free electron lasers, ultrafast electron diffraction and microscopy experiments, and inverse Compton scattering x-ray sources. Among the critical components of the photoinjector, the photocathode plays a central role, as its quantum efficiency, mean transverse energy, response time, electron energy spread of emitted electrons, and lifetime/robustness collectively determine the quality of the electron bunch generated for the aforementioned applications. Notably, a Photoemission Electron Microscope emerges as a standout instrument capable of simultaneously measuring these parameters. This study marks the inaugural utilization of PEEM as a tool for characterizing nanostructured electron sources developed for next-generation accelerator applications.

Chapter two discusses characterization techniques using photoemission electron microscope. In this chapter, the various capabilities of PEEM which includes imaging in real space, *k*-space and measuring the kinetic energy distribution of the emitted photoelectrons was discussed.

Chapter three presents a detailed investigation and photoemission characterization of nitrogen-incorporated ultrananocrystalline diamond, (N)UNCD, a novel semiconductor photocathode which has garnered attention for its potential application in photoinjectors aimed at high peak current extraction.

Chapter four presents a detailed photoemission characterization measurements from low electron affinity cesium antimonide (Cs_3Sb) photocathode films. In this work, for the first time, thermal limit mean transverse energy from Cs_3Sb photocathode was demonstrated.

Chapter five presents non-linear photoemission studies from the (N)UNCD pyramid tip cathode. In this work for the first time, the photoemission electron energy spectra from

the (N)UNCD pyramid tip cathode was measured.

In Chapter six using plasmonic Archimedean spiral photocathode, an emission spot (σ_x) of $\sim$50 nm rms resulting in a *record low* emittance of less than 40 pm-rad - at least an order of magnitude smaller compared to the best of the Åmittance previously demonstrated from a geometrically flat photocathode was demonstrated.

Lastly, in Chapter seven, using PEEM, a new mode, ‘evanescent mode’ photoemission from novel photonics integrated cathodes was demonstrated. Photoemission confined in the transverse direction as small as 1 μm using a nanofabricated Si_3N_4 waveguide under a $\sim$5 nm thick Cs_3Sb photoemissive film was demonstrated. This work demonstrates a proof of principle feasibility of such photonics-integrated photocathodes and paves the way to integrate the advances in the field of photonics and nanofabrication with photocathodes to develop next-generation high-brightness electron sources for various accelerator applications.

To Imam Hussain (AS) and the Martyrs of Karbala

ACKNOWLEDGMENTS

I would like to express my profound gratitude to those who have played a significant role in my life. In order to ensure that I acknowledge each one, I plan to express my in the following order: spiritually, personally and professionally.

On the *spiritual* front, I express my deepest gratitude, firstly, to the Almighty for His continuous blessings and guidance in my life. I am profoundly thankful to His Prophet, Rasulallah (SAW), for his prayers, guidance, and teachings, which have greatly enriched my life. Following him, I extend my gratitude to his true successor, Moula Ali (AS), for his prayers and teachings that have been a source of immense spiritual enlightenment. Next, I offer my thanks to Moulatona Fatema (AS), the daughter of the Prophet (SAW), whose prayers and blessings have contributed to our well-being and prosperity. Additionally, I express gratitude to Imam Hasan (AS) and Imam Hussain (AS) and their progeny for their boundless love and affection. The journey of Imam Hussain (AS) towards Karbala and beyond serves as a profound lesson in faith, patience, and perseverance. It has deeply influenced and shaped every aspect of my life, instilling in me invaluable principles that continue to guide me on my professional as well as spiritual journey. Furthermore, I would like to express my gratitude to His Holiness Dr. Syedna Taher Saifuddin (RA), Dr. Syedna Mohammed Burhanuddin (RA), and Dr. Syedna Mufaddal Saifuddin (TUS) for their prayers and teachings, which have uplifted me in every aspect of my life.

On the *personal* front, I begin by expressing my deepest gratitude to my mother, who was truly an angel in my life. Her boundless love, affection, and prayers have been the guiding light that has led me to success in every aspect of my life. Her unwavering support and blessings have played a pivotal role in shaping the person I am today, and I will forever cherish her memory. Miss you *Maa*. I am also profoundly grateful to my father for his tireless hard work and sacrifices, which have paved the way for me to pursue my dreams and aspirations. His dedication and commitment have been a constant source of inspiration for me. I cannot overlook the immense contribution of Nidhi Kulkarni in my life. For the past eight years, her unwavering support, care, and motivation have been instrumental in my journey. I am forever indebted to her for the profound impact she has had on my life. Next, I extend my heartfelt thanks to Nisha Singh, whose presence has brought vibrancy and joy into my life. Her unwavering support and unconditional care have been a source of strength for me, and I am truly grateful for her. Lastly, I want to express my gratitude to my friends, who are more like brothers to me - Shabbir, Burhanuddin, Yusuf, and Hussain. Our two-decade-long journey together has been filled with unforgettable memories and experiences. Their unconditional love, support, and camaraderie have been the pillars of strength that have helped me navigate life's challenges. I am forever grateful for their friendship and companionship.

On the professional front, I am immensely grateful for the invaluable guidance and support of my advisor and mentor, Prof. Siddharth Karkare. His unwavering dedication to uplifting his students and his passion for scientific exploration have been truly inspiring. I feel incredibly fortunate to have been mentored by him, and I thank the Almighty for this opportunity. The standards of patience and perseverance that he has set in pursuing scientific endeavors are qualities that I will always strive to emulate. I extend my heartfelt thanks to the members of my PhD supervisory committee - Prof. Robert Kaindl, Prof. Robert Nemanich, and Prof. Maxim Sukharev - for their time, valuable inputs, and feedback throughout my doctoral journey. I am also grateful to my fellow graduate students Pallavi, Gevork, and Chris for their unwavering support and camaraderie. Our shared experiences in the lab, from the early days of setting up equipment to the final stages of data analysis, will be cherished memories. Special acknowledgment goes to the post-docs, Oksana Chubenko and Mansoure Rizi, whose mentorship and guidance have been instrumental in my professional growth. Mentoring undergraduate student Endy has been a rewarding experience that has helped me evolve as a researcher. I am deeply appreciative

of the collaborations I have had with Dr. Evgenya Simakov, Dr. Dongsung Kim, Dr. Christopher Pierce, Dr. Daniele Filippetto, Prof. Jared Mason, Prof. Rehan Kapadia, Dr. Ragib Ahsan, Dr. Hyun Uk Chae, as well as Kevin Hilgers and Kevin Nordquist from the ASU nanofab facility. Their expertise and support have been indispensable in the success of the research endeavors presented in this thesis.

Finally, I would like to express my gratitude for the funding support from the U.S. National Science Foundation and the Department of Energy. The financial assistance has been instrumental in facilitating the various aspects of research activities presented in this thesis and has enabled me to pursue my academic and scientific endeavors, and I am deeply thankful for their contributions to my research journey.

TABLE OF CONTENTS

APPENDIX

LIST OF FIGURES

Chapter 1

INTRODUCTION

High brightness electron beams generated from photocathode-based electron sources determines the performance of various accelerator-based applications. For instance, enhanced brightness from photocathodes would enable X-ray Free Electron Lasers (XFELs) to operate at higher photon energies with increased pulse energies, facilitating the development of compact XFELs making it accessible to small-scale industry and universities and thereby advancing the scientific discovery [Emma *et al.* (2010)]. Brighter electron beams would allow for the study of macro-molecular assemblies in their native form without the need of crystallization using Ultrafast Electron Diffraction (UED) and Scattering experiments, benefiting material science and biology [Kim *et al.* (2020b)]. For particle colliders applications that involves studying the fundamental building blocks of matter, higher brightness electron beams can enhance the cooling of hadron beams, leading to increased electron-ion-collider luminosity which will help to further unravel the mysteries of nuclear structure. Brighter electron beams can enable more cost-effective designs for future linear colliders making it significantly cheaper [Harrison *et al.* (2002); Aschenauer *et al.* (2014); Benson *et al.* (2020); Larson (2011)]. Higher brightness electron beams can result in major advancements in inverse Compton Scattering experiments [Graves *et al.* (2014)]. The electron beam required for the above mentioned applcations are typically produced using photoinjectors. Photoinjectors essentially consist of a photoemissive material (photocathode) placed in a large accelerating field, which is typically in the range of 1-100 MV/m depending on the design of the photoinjector. The metric of a photocathode to be used in a photoinjector is evaluated by its quantum efficiency (QE), response time, mean transverse energy (MTE) or equivalently intrinsic emittance of the photocathode, its lifetime/robustness when operated under high accelerating field gradients as well as the kinetic energy spread of the emitted electrons. Each of these parameters is discussed in detail in the following sections.

1.1 Quantum Efficiency

The theoretical derivation of QE is given by the Dowell-Schmerge (DS) model [Dowell and Schmerge (2009a)] which derives QE using the the free electron gas theory and Spicer's three step model for photoemission [Spicer (1958)]. According to Spicer's model, an electron is emitted from the photocathode by means of three sequentially independent steps. The first step involves absorption of photon by the electron. The electron can absorb either one (linear emission) or more photons (non-linear emission). The second step involves migration of electron to the cathode-vacuum interface which includes scattering with other electrons. For the case of metal photocathodes, once the photon is absorbed, the electrons transport to the metal's surface with some scattering against the valence electrons and loses enough energy to remain bound. Only those electrons which do not suffer from electron-electron scattering escape from the metal surface. Lastly, the third step involves emission of electrons from the photocathode surface overcoming the surface potential barrier. According to the DS model, for photoemission near threshold, the QE of the material scales as the square of excess energy and is given by the following equation:

$$\mathrm{QE} \propto (\hbar\omega - \Phi_{effective})^2, \tag{1.1}$$

where $\Phi_{effective}$ is the effective work function of a photocathode and the excess energy is given by the difference between the photon energy and the work function of a photocathode.

For practical purposes, the QE of the photocathode is calculated using the number of electrons extracted per incident photon on the photocathode material and is given by the following expresssion:

$$\mathrm{QE} = \frac{I\hbar\omega}{P}, \tag{1.2}$$

where I is the average photocurrent , $\hbar\omega$ is the photon energy and P is the average laser power.

Typically metal photocathodes such as Copper (Cu) have QE in the range of $10^{-5}-10^{-7}$ under UV illumination near threshold and are mostly used for applications which require low average currents [Davis *et al.* (1993)]. The low QE in metals is attributed to electron-electron scattering within the metal photocathode. Once the photon is absorbed, the electrons transport to the metal's surface with some scattering against the valence electrons and loses enough energy to remain bound. Only those electrons which do not suffer from electron-electron scattering escape from the metal surface. Low electron affinity semiconductor photocathodes (in which the work function is less than two times the band-gap) such as negative electron affinity (NEA) GaAs [Biswas *et al.* (2021)] or alkali antimonides [Saha *et al.* (2022)] have QE in the range of 10^{-2} and 10^{-1} respectively in the visible range, and are used for high average current applications. For low electron affinity semiconductor photocathodes, the scattering of electron happens with the phonons in the conduction band minimum before emission. The electrons on scattering with phonons loses only a small fraction of their energy escaping from the semiconductor-vacuum interface. As a result, they have higher QE when compared to metal photocathodes.

1.2 Response Time

The response time of a photocathode is given in terms of the extracted electron bunch length when compared to the incoming laser pulse and is generally expressed in terms of root mean square (rms) length of the electron bunches (σ_t) [Musumeci *et al.* (2018)]. Many photoinjector applications require a fast response time ($<$ 1 ps) to temporally shape the initial electron distribution and maintain the beam quality during acceleration in the photoinjector. A fast response time implies that the electrons are emitted quickly after the absorption of incident photon energy. For the case of metals, the response time is on the femtosecond time scales and the temporal shape of the emitted electron bunch follows the temporal shape of the incoming laser pulse.

In low electron affinity semiconductor photocathodes such as NEA-GaAS, very close to the photoemisison threshold, the electron bunch is emitted with the temporal spread of hundred of picoseconds. This is because the electrons are emitted from deep within the semiconductor surface at photon energies close to the band-gap due to the low absorption depths ranging beyond a few micrometer. For most of the applications, response time with sub-picosecond to picosecond timescales is desirable [Lessner *et al.* (2017)].

1.3 Intrinsic Emittance and Mean Transverse Energy

The electron beam emitted from the photocathode is contained within a phase space volume, known as the emittance and is expressed in terms of the following equation:

$$\varepsilon_{n,x} = \frac{\sqrt{\langle x^2\rangle\langle p_x^2\rangle - \langle x p_x\rangle^2}}{m_e c}, \tag{1.3}$$

where $\varepsilon_{n,x}$ is the normalized transverse emittance in the one of the two transverse directions (x), $\sqrt{\langle x^2\rangle} \equiv \sigma_x$ is the root mean square (rms) electron spot size in the x-direction, $\sqrt{\langle p_x^2\rangle} \equiv \sigma_{p_x}$ is the rms electron momentum spread in the x-direction, $\langle x p_x\rangle$ is the correlation term between the location of emission and the transverse momentum, m_e is the mass of an electron and c is the speed of light [Dowell and Schmerge (2009b)].

If we further assume that there is no correlation between the location of emission and the transverse momentum, then the cross term is zero and one obtains the following equation for the rms normalized emittance:

$$\varepsilon_{n,x} = \sigma_x \frac{\sigma_{p_x}}{m_e c}, \tag{1.4}$$

For the case of photocathodes, σ_{p_x} is expressed in terms of mean transverse energy (MTE) of the emitted electrons expressing emittance by the following equation:

$$\varepsilon_{n,x} = \sigma_x \sqrt{\frac{\text{MTE}}{m_e c^2}}, \tag{1.5}$$

Minimizing the emittance of emitted electron beams holds paramount significance across various photoinjector applications due to its profound impact on beam brightness relative to current levels. In high UED/M (Ultrafast Electron Diffraction/Microscopy) applications, the normalized transverse emittance of the electron bunch dictates the spatial resolution of the instrument [Musumeci *et al.* (2018)]. Moreover, for high repetition rate UED/M applications exceeding 100 kHz, achieving a normalized transverse emittance below 1 nm-rad is imperative to advance the frontiers of such applications. Nevertheless, as of now, no photocathode has attained a normalized transverse emittance below 1 nm-rad.

As we can see from equation 1.4 and 1.5, the normalized transverse emittance of the electron beam can be reduced by either reducing the spot size of the cathode or by reducing the MTE (or rms momentum spread) of the emitted electrons. The MTE of the electrons depends on the cathode material, its surface morphology as well as the laser photon energy and fluence used for excitation. For the case of metal photocathodes, the MTE of the emitted electrons follow the DS model which says that the MTE of the electrons scales as one third of the excess energy (difference between the photon energy and work function) as shown by the following equation.

$$\mathrm{MTE} = \frac{\hbar\omega - \Phi_{effective}}{3} = \frac{\Delta E}{3}, \tag{1.6}$$

where ΔE is the excess energy. At the threshold, MTE is limited by the Fermi tail of the electron distribution to k_BT, where k_B is the Boltzmann constant and T is the lattice temperature of the cathode. For example, the smallest MTE of 25 meV was demonstrated for antimony films when operated near the threshold at room temperature [Feng *et al.* (2015)]. More recently, it has been shown that the MTE of 5 meV can be achieved by cooling Cu(100) photocathode to cryogenic temperatures [Karkare *et al.* (2020)]. On the other hand, low electron affinity semiconductor photocathodes such as GaAs activated to negative electron affinity using Cs and NF_3 as well as alkali antimonide such as Cs_3Sb, the observed value of MTE is $\sim$40 meV at threshold when operated at the room temperature [Bazarov *et al.* (2008); Cultrera *et al.* (2011, 2015)].

The MTE of the electrons emitted from the cathode also depends on its surface morphology. The surface morphology of the cathode can be characterized by two parameters: first, the physical roughness and second, work function variation (also termed as chemical roughness) of a photocathode. Nano-scale physical roughness on the cathode results in increase in MTE and this can be attributed to two effects. First is the 'slope effect' where the electrons are emitted from the local surface normal of the photocathode as opposed to its global surface normal. The second, known as the 'field effect', arises due to generation of a transverse local electric field due to the roughness on the photocathode surface. In general, the field effect dominates as compared to the slope effect and ergo the slope effect is usually ignored in the analysis. The detailed analysis of MTE increase due to physical roughness has been previously reported [Zhang and Tang (2015); Qian *et al.* (2012); Feng *et al.* (2017); Smedley *et al.* (2015)]. Assuming the sinusoidal variation in the surface roughness profile, the scaling of MTE to the first order is given by the following equation:

$$\mathrm{MTE}_{field} \propto \frac{Ea^2}{\lambda}, \tag{1.7}$$

where E is the applied electric field, a is the amplitude and λ is the period of the physical roughness profile. As we can see, the contribution to MTE due to physical roughness increases with increasing accelerating field gradient. The chemical roughness arises due to lateral potential variations which is the result of the varying work function. It has been shown that the effect of chemical roughness becomes less prominent with increasing accelerating field gradient [Karkare and Bazarov (2015)]. In general, for practical photocathodes with physical and chemical roughness, the MTE of the emitted electrons is given by:

$$\mathrm{MTE} = \mathrm{MTE}_{kT} + \mathrm{MTE}_{field} + \mathrm{MTE}_{WF}, \tag{1.8}$$

where MTE_{kT} is the contribution due to thermal limit which is ~25 meV at room temperature, MTE_{field} is the contribution due to the physical roughness and MTE_{WF} is the contribution due to the work function variation or chemical roughness of the photocathode. For most photoinjectors applications, the MTE extracted from photocathodes is in the range of 0.1 - 1 eV [Dowell *et al.* (2010)].

1.4 Kinetic Energy of Photo-electrons

The kinetic energy spread of the photoemitted electrons holds significant promise for applications in ultrafast electron energy loss spectroscopy (EELS) where rapid changes in material properties require high temporal and energy resolution [Egerton (2008)]. By generating electrons with narrow energy spread by operating photocathode at the threshold, we can push the boundaries of ultrafast spectroscopy, facilitating advances in fields such as materials science, surface chemistry, and condensed matter physics.

1.5 Electron Beam Brightness

The emittance, the QE (or emitted current) and the kinetic energy spread of the photoemitted electrons can be combined into one figure of merit, the 6D-Brightness given by [Filippetto *et al.* (2022)]:

$$\mathrm{B}_{6\mathrm{D}} = \frac{I_{rms}}{\varepsilon^2_{n,rms}\frac{\sigma_E}{m_e c}}, \tag{1.9}$$

where we assume no time-energy correlation in the bunch and σ_E is the rms kinetic energy distribution of emitted electrons, $I_{rms} = Ne/\sigma_t = \eta I_{peak}$, with I_{peak} being the maximum current within the pulse, N the number of electrons in the bunch, e is the charge of an electron and η a numerical value depending on the shape of the temporal distribution ($\eta =$

$\sqrt{2\pi}$ for a Gaussian temporal profile). $\varepsilon_{n,rms}$ is the geometric mean value of the emittance along the x-and y-directions.

Depending on the specific application, different brightness definitions are often introduced to better encapsulate the key properties of the electron beam. In typical ultrafast electron diffraction experiments, it's the electron beam's transverse emittance, rather than the energy spread, that predominantly influences the minimum beam size at the sample and the resolution in reciprocal space. In such cases, the five-dimensional brightness, denoted as $\mathrm{B}_{5\mathrm{D}}$, is considered more representative of the electron beam's effectiveness for conducting an experiment and is given by the following equation.

$$\mathrm{B}_{5\mathrm{D}} = \frac{I_{rms}}{\varepsilon_{n,rms}^2}, \tag{1.10}$$

Longitudinal beam compression can increase $\mathrm{B}_{5\mathrm{D}}$ by boosting the beam peak current at the expense of energy spread of the electrons.

Further reducing the number of dimensions, one can define a brightness specific to the transverse planes, known as the four-dimensional brightness, denoted as $\mathrm{B}_{4\mathrm{D}}$ given by the following equation.

$$\mathrm{B}_{4\mathrm{D}} = \frac{Q}{\varepsilon_{n,rms}^2}, \tag{1.11}$$

Here $Q = Ne$ is the total bunch charge. This metric proves particularly valuable when balancing trade-offs between temporal and spatial resolution in time-resolved photoinjector applications. Higher values of $\mathrm{B}_{4\mathrm{D}}$ leads to improved diffraction pattern contrast and enhanced spatial resolution in UED/M experiments. Assuming no coupling between longitudinal and transverse planes, the $\mathrm{B}_{4\mathrm{D}}$ is determined at emission and remains constant throughout transport and acceleration of the electron bunch in an accelerator.

The performance of a photocathode hinges on the quality of the electron bunch it generates, a metric determined by several factors including QE, emittance, MTE, energy spread, and electron bunch brightness. Typically, these characteristics are assessed using various instruments or measurement procedures. For example, electron energy analyzers or complex MTE measurement procedures are employed to measure the MTE and energy spread of emitted electrons [Karkare *et al.* (2019); Cultrera *et al.* (2015)]. Emittance, on the other hand, is gauged using techniques such as solenoid scan, pepper-pot, or slit wire methods, among others [McDonald and Russell (2005)]. Alternatively, emittance can be measured by assessing the electron emission area from the cathode alongside the transverse momentum spread (or MTE) of emitted electrons. A Photoemission Electron Microscope (PEEM) stands out as an instrument capable of simultaneously measuring these parameters. Additionally, PEEM can ascertain the number of electrons emitted from the photocathode by recording counts per second on the Microchannel Plate (MCP) detector and utilizing a predetermined calibration factor to convert these counts into emitted electrons, facilitating QE calculation. Moreover, commercially available PEEM models like the FOCUS-IS-IEF PEEM can also determine the kinetic energy distribution of emitted electrons [Foc (2024)]. Consequently, PEEM emerges as a potent tool for characterizing photocathodes not only in terms of QE, emittance, MTE, and electron bunch brightness but also for evaluating the uniformity of electron emission areas. Additionally, it can also be used for determining the chemical roughness of a photocathode material. Remarkably, despite its potential, PEEM has not been utilized for photocathode characterization to date. In this study, we present, for the first time, the utilization of PEEM as a tool for characterizing nanostructured electron sources developed for next-generation accelerator applications.

Chapter Two discusses characterization techniques using photoemission electron microscope (PEEM). In this chapter, we discuss the various capabilities of PEEM which includes imaging in real space, *k*-space and measuring the kinetic energy distribution of the emitted photo-electrons.

Chapter Three serves as the first-author journal publication [Kachwala *et al.* (2022b)] detailing the investigation of nitrogen-incorporated ultrananocrystalline diamond, (N)UNCD, as a novel semiconductor photocathode. This material has garnered attention for its potential application in photoinjectors aimed at high peak current extraction. Our study focuses on the spectral response in QE, photoemission energy spectra, and MTE of the (N)UNCD photocathode utilizing a PEEM. Notably, the observed OE demonstrated comparability to that of copper photocathodes. Analysis of the photoemission spectra revealed evidence of electron scattering preceding emission. This relaxation phenomenon, is also evident in the spectral response of the MTE, which is limited to approximately 70 meV at the threshold due to attributed to the physical and chemical roughness of the (N)UNCD photocathode

While (N)UNCD serves as a robust semiconductor photocathode, its low QE restricts its utility in accelerator applications necessitating large average currents. To compensate for the low QE, higher laser fluences are often employed to extract the required charge densities, leading to non-linear photoemission processes [Maxson *et al.* (2017); Bae *et al.* (2018)]. These nonlinear processes contribute to an increase in the MTE to a few hundred meV, consequently diminishing the brightness of the emitted electron bunches. One strategy to mitigate the degrading effect of non-linear photoemission on MTE is through the utilization of high QE, low electron-affinity semiconductor cathodes, such as alkali antimonides like Cs_3Sb.

Chapter Four is based on *first author* journal publication [Kachwala *et al.* (2023b)], wherein we present comprehensive MTE, Photoemission Electron Energy Spectra (PEES), and QE measurements from Cs_3Sb films in the spectral range of 1.45-2.33 electron volts (eV) photon energy. This spectral range is broader compared to previous studies [Sakata (1953); Cultrera *et al.* (2011, 2015)]. Our PEES measurements conclusively demonstrate that the work function of CsSb cathodes is approximately 1.5 eV. Furthermore, we illustrate that at the threshold of 1.5 eV, for the first time, the MTE does reach the thermal limit ($k_B T$) value at the room temperature.

The emittance and thereby the brightness of the electron bunch from such large area cathode is limited σ_x or σ_{p_x} (or MTE) or both. MTE of the electrons from a photocathode when operated at the threshold is limited by thermal limit (k_BT) value. As a result, to reduce the emittance further, necessary for various photoinjector applications, we need to reduce σ_x. σ_x is limited by the diffraction limit of light and the ability to focus the laser to a small spot size [Silfies *et al.* (2019); Musumeci *et al.* (2018)].

σ_x of the electron bunch can be reduced to the nanometer scale by laser assisted photoemission from photocathodes with the nanometer sized tips. *Chapter Five* is based on *first author* journal publication [Kachwala *et al.* (2024)], wherein we present non-linear photoemission studies from the (N)UNCD pyramid tip cathode. In this work for the first time, we measured the PEES that show electrons with energies as high as $\sim$10 eV. Based on the shape of the electron energy spectra, we conclude that the high-energy electrons are thermally emitted electrons due to ultrafast laser heating at the tip of the (N)UNCD pyramid tip cathode.

Many accelerator based applications require relativistic electron beams to mitigate the effects of Coulomb repulsion. In addition for UED/M applications, RF guns used to obtain mega electron volt (MeV) scale energy electron bunches for reduced jitter owing to their relativistic speeds and larger signal in higher-order diffraction peaks due to the shorter electron wavelength [Siddiqui *et al.* (2023); Ji *et al.* (2019); Weathersby *et al.* (2015); Carter and Williams (2016)]. Tip-based photoemitters cannot be used in high electric field RF environment to achieve MeV scale electron energies due to catastrophic failure modes and one requires a photocathode which is geometrically flat to withstand high electric field in RF environment.

In *Chapter Six* we demonstrate an emission spot (σ_x) of $\sim$50 nm rms resulting in a *record low* emittance of less than 40 pm-rad - more than three orders of magnitude smaller compared to the best emittance of <50 nm-rad previously demonstrated from a photocathode [Li *et al.* (2012)]. The small emission area has been achieved using a combination of non-linear photoemission and focusing of light to sub-diffraction limited areas using plasmonic Archimedean spirals.

Lastly, in *Chapter Seven*, using PEEM, we demonstrate a new mode, ‘evanescent mode’ photoemssion from novel photonics integrated cathodes. Here, we demonstrate photoemission confined in the transverse direction as small as 1 μm using a nanofabricated Si_3N_4 waveguide under a $\sim$5 nm thick cesium antimonide (Cs_3Sb) photoemissive film. This work demonstrates a proof of principle feasibility of such photonics-integrated photocathodes and paves the way to integrate the advances in the field of photonics and nanofabrication with photocathodes to develop next-generation high-brightness electron sources for various accelerator applications.

Chapter 2

PHOTOEMISSION ELECTRON MICROSCOPE: A TOOL TO CHARACTERIZE PHOTOCATHODES

Photocathodes play an important role in present and future photoinjector applications which require electron sources having high quantum efficiency (QE), low mean transverse energy (MTE), a quick response time as well as low kinetic energy spread of the emitted electrons. In addition, the electron kinetic energy spectra can give insights into the understanding of electron emission mechanisms which can aid in the development of next generation photocathodes. In this chapter, we discuss about the excitation light sources used in this thesis as well as photoemission electron microscope (PEEM) which was used to characterize photocathodes in terms of its QE, photoemission electron energy spectra, MTE and electron emission area. In section 2.1, I talk about the excitation sources used throughout this thesis for photoemission experiments. In section 2.2, I discuss the general operation of Photoemision electron microscope (PEEM) [Model:FOCUS-IS-IEF PEEM] and the various electrostatic lenses associated with it. In section 2.3 I discuss about the real space imaging capabilities of PEEM and the best possible imaging resolution that can be achieved using using Hg lamp ($\hbar\omega = 5.2$ eV) and a 500 kHz repetition rate femtosecond pulsed laser with a pulse length of 150 fs from a pulsed Optical Parametric Amplifier (Light Conversion Orpheus pumped by Light Conversion Pharos). In section 2.4, I discuss about the *k*-space imaging capabilities of PEEM and the best possible imaging resolution that can be achieved. In this section I also discuss about measuring MTE of the emitted electrons from *k*-space images and the best possible resolution that can be achieved while measuring MTE of the emitted electrons. This is followed by section 2.5 which discusses about measuring the kinetic energy distribution of the emitted photoelectrons. Lastly, in section 2.6, I conclude by summarizing the the best possible resolution that can be obtained using PEEM which will be used for measuring QE, photoemission electron energy spectra and MTE of the emitted electrons.

2.1 Light Sources

Light sources are an essential part of photoemission experiments. In this section, I will talk about light sources and their relevant features used in this thesis.

2.1.1 Continuous Wave Source

The FOCUS-IS-IEF PEEM is equipped with a continuous wave high-pressure mercury (Hg) lamp with a luminance of 1700 $\mathrm{cd/mm^2}$. Compared to the pulsed laser source the lamp has a wide spot size which nearly homogeneously illuminates the sample and is therefore used for overview imaging. The Hg-lamp has a broader spectrum at its high-energy edge with a maximum at $\hbar\omega = 4.9$ eV and its tail extending upto $\hbar\omega = 5.2$ eV Foc (2024). The infrared part of the spectrum is cut-off by the use of heat filter enclosed within the casing of the Hg-lamp to prevent heating of the sample. The light is made incident on the sample using in-vacuum lens assembly at 65° angle of incidence (AOI) with respect to the normal of the sample.

2.1.2 Pulsed Laser

The pulsed laser used for the photoemission characterization in this thesis was derived from a pulsed 200-2000 nm wavelength tunable optical Parametric Amplifier (Light Conversion Orpheus pumped by Light Conversion Pharos). The repitition rate was 500 kHz with a pulse length of 150 fs and the full width half maximum bandwidth of 2 nm. The laser can be made incident on the sample at vaious angle of incidence viz.65°, 45°, 4°(from the top after refletion from in-vacuum 45° mirror) and 0° (from the bottom) with respect to the normal of the sample as shown in Fig. 2.1.

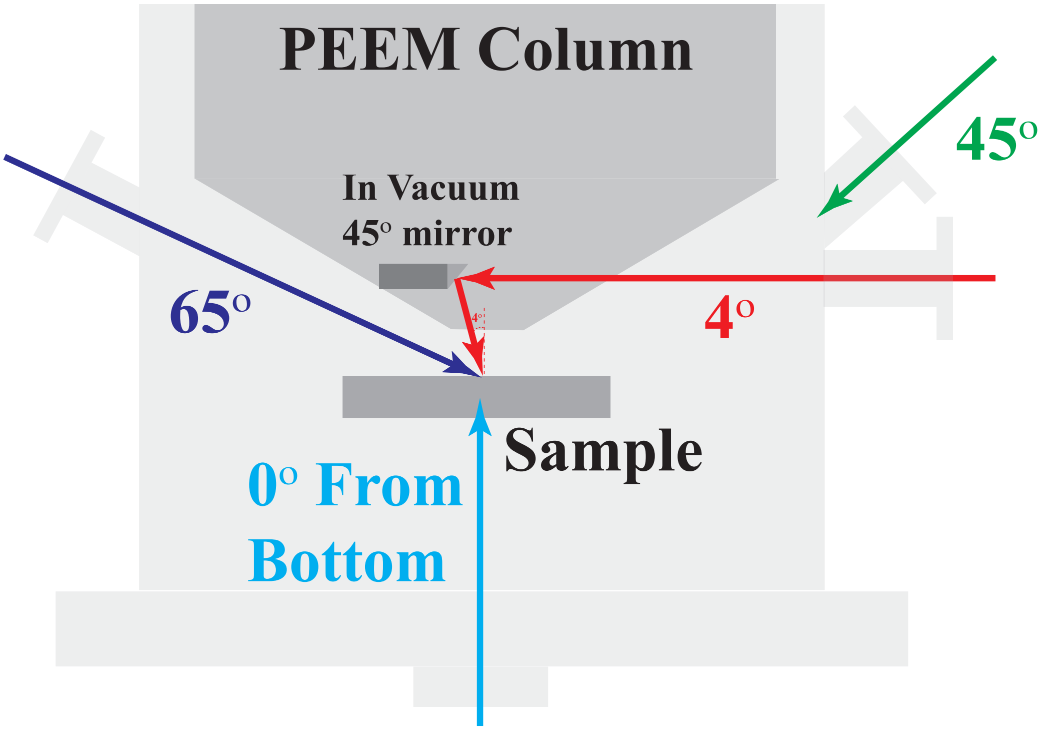

Figure 2.1: Cartoon schematic of ultra high vacuum chamber of PEEM showing various possible angle of incidences with respect to the normal of the sample.

2.2 Instrumentational Aspects of Photoemission Electron Microscope

The FOCUS-IS-IEF PEEM is one of the representatives of the commercially available PEEM which consists of an integrated sample stage and an imaging energy filter along with various different electrostatic lens system. The basic layout of the PEEM instrument is shown in Fig. 2.2. To begin with, it consists of an integrated sample stage which is equipped with a piezoelectric sample positioning. The integrated sample stage reduces the relative motion/vibration between the sample and the microscope column. The microscope column consists of an *objective* lens, which like any microscope is used to magnify the image of the sample. The *objective* lens is a tetrode, i.e. it is made up of four lenses, namely *sample*, *extractor*, *focus* and *column*. The *sample* potential is mostly grounded

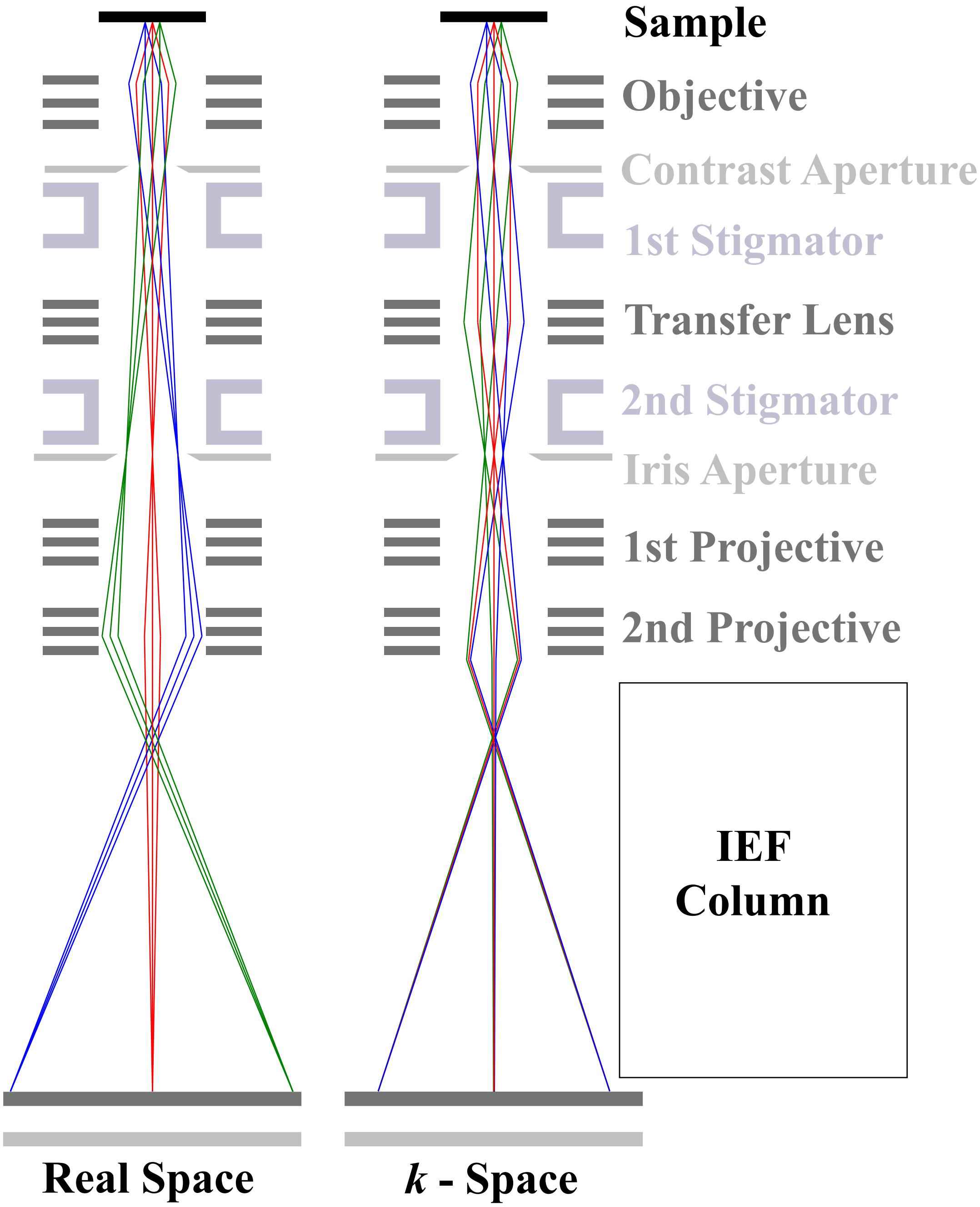

Figure 2.2: Basic layout of PEEM instrument showing various electrostatic lens system and the electron trajectories when operated in real space and *k*-space mode. Figure adapted from Foc (2024)

except in the case of acquiring energy filtered images. The *column* voltage is usually fixed and kept at 1 kV. The *extractor* voltage, on the other hand is used to obtain the desired magnification in the microscope. For high magnification mode, the extractor voltage is varied between 6-13 kV and the optimum is achieved when the extractor voltage is at 12 kV. For extensive overview of the sample region, the extractor voltage is kept low and the microscope is operated in low magnification mode. The *focus* voltage is used to focus the image obtained. Alternatively, the image can also be focused by varying the distance between the *objective* lens and the sample stage. A *contrast aperture* is placed at the back-focal plane of the objective lens which reduces the angular spread of the emitted electrons. Limiting the angular spread increases the resolution of the image but at the same time reduces the transmission of the microscope. *contrast apertures* with five different diameters are available, namely 1750, 500, 150, 70 and 30 μm. Figure 2.3 shows typical transmission of different contrast apertures for the column voltage of 1.2 kV. A variable *iris aperture* is placed in the first intermediate image plane of the PEEM column while imaging in the real space mode. The iris aperture can be closed so that only a defined part of the spatially resolved photoelectron distribution can pass further into the microscope. Another application of *iris aperture* is for studying *k*-space distribution of the emitted photoelectrons from the definite region of the sample. The octupole *stigmators/deflectors* are used to correct for astigmatism and improve the resolution of the microscope. The *transfer lens* is an optional element and is used while obtaining the momentum distribution of the emitted electrons. There are two *projective lenses* which are used to project the first intermediate image onto the 2D detector. They can be used for additional magnification.

The microscope column is followed by the subsequent energy filter which preserves the PEEM image during energy filtering process. It consists of two pre-retardation lens and two retardation grids that forms the retarding field analyzer (RFA). The retarding field acts as the high pass energy filter that allows for energy filtered imaging.

The photoemitted electron distribution from the photocathode can be imaged onto the imaging unit at the end of the instrument column in a spatially resolved real space or as

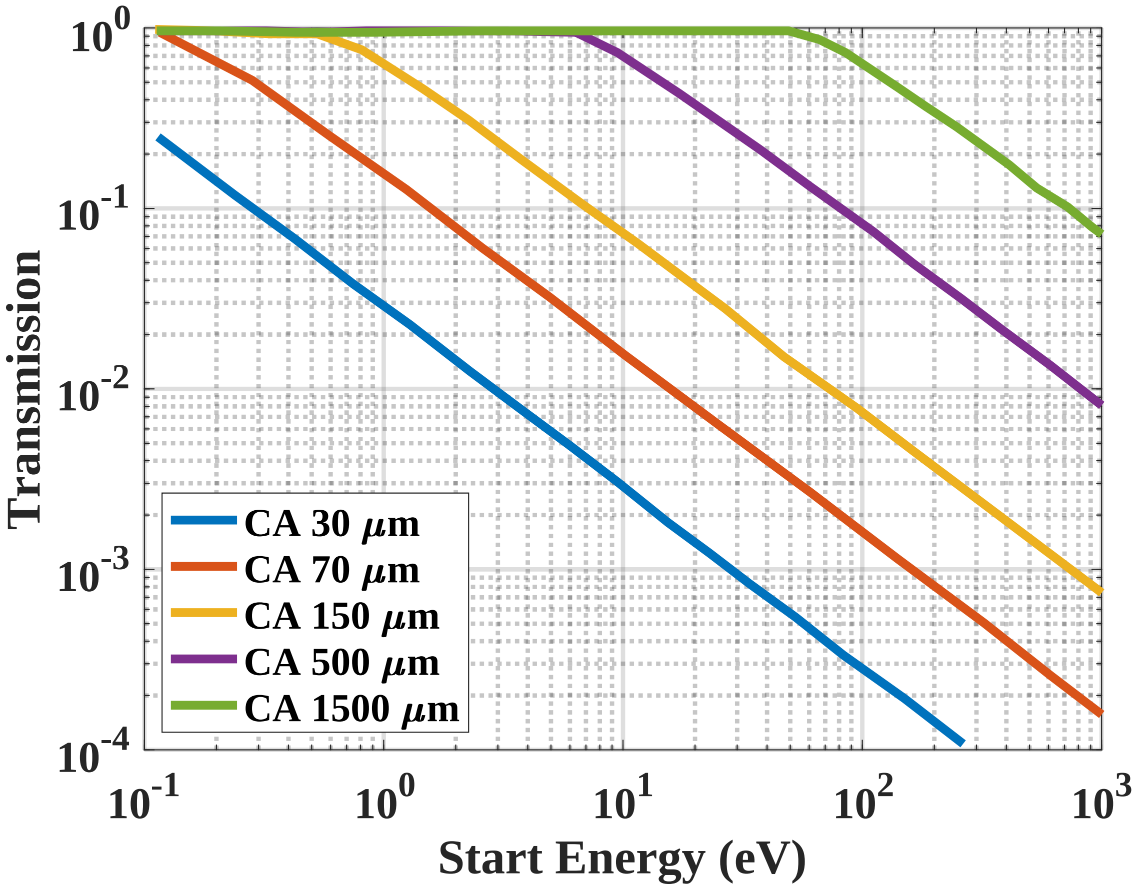

Figure 2.3: Transmission of *Objective lens* for different *contrast aperture* size and different kinetic energies of emitted electrons at 1.2 kV *column voltage* assuming cosine distribution of emitted electrons. Figure data and caption adapted from Foc (2024)

the reciprocal momentum space distribution image. In addition, both spatially resolved real space and the reciprocal space momentum distribution images can be imaged using integrated imaging energy filter and thus obtain energy filtered images. The detailed description of different imaging modes using PEEM is discussed below.

2.3 Real Space Imaging

The schematic of experimental set up while imaging in real space mode is shown in Fig. 2.4 (a). The photoemitted electrons from the sample are imaged by the *objective lens* as the first intermediate image at the location of the *iris aperture*. At the back focal plane of the

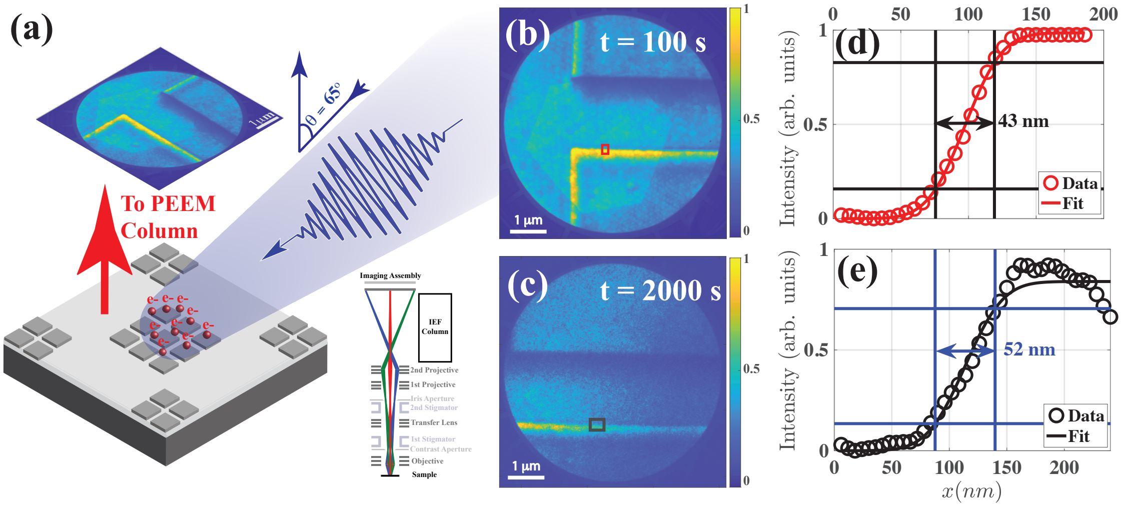

Figure 2.4: (a) Schematic of experimental set up showing Ag/Si-grid ("SgS-28") test sample illuminated by femtosecond laser with the pulse length of 150 fs and central wavelength of 300 nm. The laser was was made incident onto the sample at 65° with respect to the axis of the sample. The electrons emitted are accelerated towards the PEEM column. The inset shows the electron trajectories while imaging in real space mode. Real space (b) Hg lamp image with a total acquisition time (t) of 100 s, (c) Image obtained using a femtosecond laser with the pulse length of 150 fs and central wavelength of 300 nm with a total acquisition time (t) of 2000 s. Experimental data points with error function fit showing the real space resolution (16/84 % profile) of (d) 43 nm obtained with Hg lamp and (e) 52 nm obtained with pulsed femtosecond laser.

objective lens, the *contrast aperture* limits the angular distribution of emitted electrons. To obtain high resolution images, a smaller c*contrast aperture* is selected whereas to image all the emitted electrons, a larger *contrast aperture* is selected. The *transfer lens* is not used while imaging in the real space mode. The *projective lenses*, P1 and P2, project the first intermediate image onto the second intermediate image plane magnified further on the detector. If the energy filter is turned on, the electrons are retarded by the IEF system and energy filtered real space images are obtained on the detector. The schematic of electron trajectories while imaging in real space mode is shown in the inset of Fig.2.4 (a). The test of the spatial resolution of the microscope was performed with a specifically designed sample which consisted of Ag/Si-grid, small squares with 10 μm pitch arrayed into large squares with 500 μm pitch ("SgS-28"). The real space images were acquired using Hg lamp ($\hbar\omega = 5.2eV$) (Fig. 2.4 (b)) as well as femtosecond laser with the pulse length of

150 fs and central wavelength of 300 nm (Fig. 2.4 (c)). To determine the resolution, a line profile was fitted with a convolution of Gaussian and step function (for details see appendix A) which is expressed as:

$$C(x) = \{ \begin{array}{ll} \frac{I_0}{2}\left(1+erf\left(\frac{x+b}{\sqrt{2}\sigma}\right)\right), & \text{for } Rising\ Edge \\ \frac{I_0}{2}\left(1-erf\left(\frac{x-b}{\sqrt{2}\sigma}\right)\right), & \text{for } Falling\ Edge \end{array} \tag{2.1}$$

The best possible resolution obtained was 43 nm using Hg lamp ($\hbar\omega = 5.2eV$) and 52 nm using a pulsed femtosecond laser as shown in Fig. 2.4 (d-e). The fluence of the laser pulses incident on the sample was be kept small enough to ensure linear electron counts and avoid effects of space charge and non-linear photoemission that leads to degradation of image resolution. As a result, the acquisition time of images acquired using pulsed laser is approx. 20 times that of the image acquired using Hg lamp.

2.4 Momentum (k) Space Imaging

In momentum space imaging mode, the distribution of the parallel momenta of the photoelectrons detected by the PEEM corresponds to the momenta of the final states in the sample as shown in Fig. 2.5. In order to maintain correct angular distribution in all the image points in the PEEM column, a telescopic image is needed in the first intermediate image plane. This is achieved by using an additional transfer lens behind the objective lens. The telescopic image obtained in the first intermediate image plane can also be projected as a real space image onto the detector. Hence, it is extremely easy to switch between a real-space and momentum space imaging mode. In both the cases, the electron distributions in the back focal plane and in the first image plane remain equal (see Fig. 2.2. This is important as one can select a certain region of the sample in the real space mode using the variable *iris aperture* and image the same region in the momentum space mode. If the energy filter is turned on, the electrons are retarded by the IEF system and energy filtered momentum space images are obtained on the detector. The best possible resolution

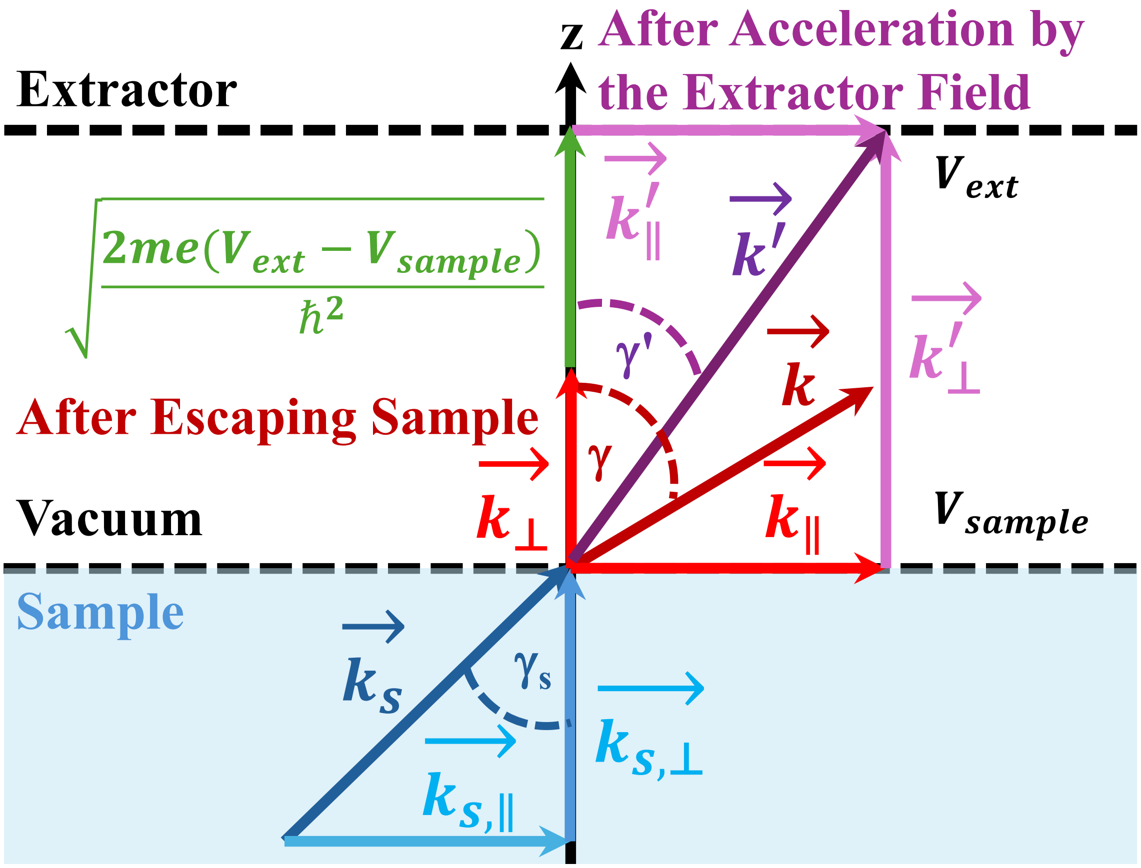

Figure 2.5: The final state wave vector $\overrightarrow{k_s}$ of an electron inside the sample is diffracted by the surface potential at the sample vacuum interface and leaves the sample with a momentum vector $\overrightarrow{k}$.The momentum vector parallel to the surface is conserved during this transition i.e. $\overrightarrow{k_{s,\parallel}} = \overrightarrow{k_\parallel}$. After emission, the electron is accelerated by the extractor electric field perpendicular to the surface which only changes the perpendicular component of the electron momentum. The transverse component imaged by the microscope equals the parallel final state momentum in the sample.

obtained while imaging in k-space mode is 7.4 $m\text{Å}^{-1}$.

2.4.1 *MTE Measurements from Momentum Space Images*

MTE measurements were performed by operating PEEM in k - space mode with a sub 8 - $m\text{Å}^{-1}$ k - space resolution. Micrometer region of the sample was selected by the adjustable iris aperture that is placed in the first intermediate image plane of the PEEM column while imaging in the real space mode. After limiting the area under investigation

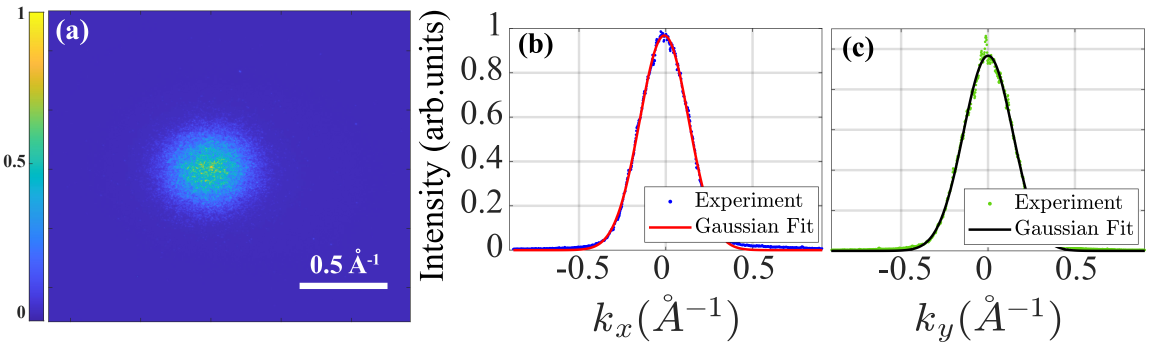

Figure 2.6: (a) k - space image taken for the (N)UNCD sample at $\lambda = 240$ nm with filed of view of 1.9 Å^{-1}. Gaussian fit applied to the (b) k_x distribution and (c) k_y distribution obtained from (a).

in the real space mode by adjutable iris aperture, its counterpart in the k - space mode is imaged by changing the projective settings of the PEEM. After obtaining k - space distribution of the emitted electrons shown in Fig. 2.6 (a), a Gaussian fit is applied to the k_x and k_y distributions as shown in Fig. 2.6 (b) and (c). The MTE is then calculated using the second moment obtained from the Gaussian fit applied to the measured k - space distribution of the emitted electrons using the following equation:

$$\mathrm{MTE} = \frac{\hbar^2\sigma^2}{2m_e}. \tag{2.2}$$

Here, $\hbar$ is the reduced Planck's constant, m_e is the mass of an emitted electron and $\sigma = \sqrt{\sigma_{k_x}{}^2 + \sigma_{k_y}{}^2}$, where σ_{k_x} and σ_{k_y} are the second moments obtained from the Gaussian fit applied to k_x and k_y distributions of the emitted electrons. The contrast aperture (CA) of diameter 1750 μm placed in the back focal plane of the objective lens in the PEEM column is selected to ensure transmission of all the emitted electrons from the sample surface. The resolution for MTE measurement is determined by the convolution of two Gaussian distributions: 1) Gaussian distribution corresponding to k - space resolution and 2) Gaussian distribution corresponding to MTE measurement. This results in the resolution of 0.2 meV corresponding to MTE value of 25 meV.

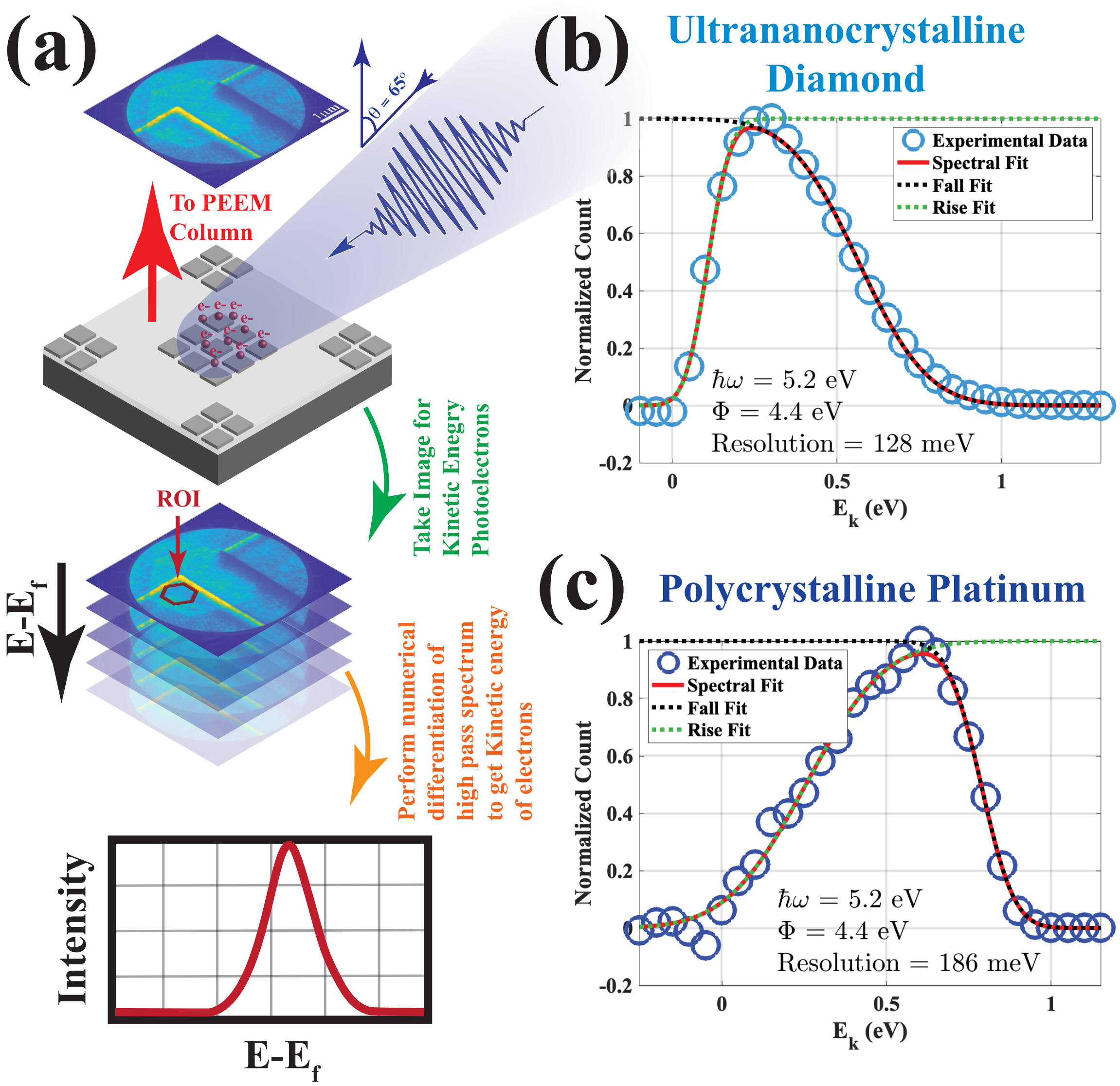

Figure 2.7: (a) The schematic shows the operation modes of energy-filtered photoemission electron microscopy and the process of data acquisition. Real space spatially resolved energy filtered images are acquired from the specimen. Micrometer region of interest (ROI) can be selected by the adjustable iris aperture and the energy filtered images can also be obtained in the *k* - space mode. The measured width using spectral fit from the (b) rising edge of the photoemission spectra obtained from (N)UNCD sample showing the rising width of 128 meV and (c) falling edge (Fermi edge) of the photoemission spectra obtained from the polycrystalline platinum sample showing the falling width of 186 meV.

The photoemission electron energy spectra was determined by performing a numerical differentiation of high pass spectrum obtained using IEF column of the PEEM after acquiring the background subtracted energy filtered images, either in real space mode or momentum space mode. The experimental energy resolution of the PEEM was determined by fitting a model function (for details see appendix A) shown below.

$$S(x) = \frac{I_0}{4}\left(1 + erf\left(\frac{x + b_{wr}}{\sqrt{2}\sigma_{wr}}\right)\right)\left(1 - erf\left(\frac{x - b_{wf}}{\sqrt{2}\sigma_{wf}}\right)\right) \tag{2.3}$$

The experimental energy resolution was determined from the *rising edge* when scattering of electrons was involved (see chapter 3 for details on electron scattering in photoemission electron energy spectra) and was determined from the Fermi edge in case of metal photocathodes. Fig. 2.7 (b) shows energy resolution of 128 meV when determined from the rising edge of the energy spectra of ultrananocrystalline diamond photocathode. Fig. 2.7 (b) shows energy resolution of 186 meV determined from the Fermi edge of the energy spectra of poly-crystalline platinum photocathode. Both the spectra were obtained using pulse laser with central wavelength of 240 nm. It is worth mentioning that for the case of single crystalline photocathodes, the experimental energy resolution is given by,

$$(\Delta E) = \sqrt{(\Delta E_{instrument})^2 + (\Delta(\hbar\omega))^2 + (4k_BT)^2} \tag{2.4}$$

where, $\Delta E_{instrument}$ is the energy resolution of the instrument, $\Delta(\hbar\omega)$ is the bandwidth of the excitation source, T is the effective operating temperature and k_B is the Boltzman constant. Using single crustalline Ag (111) sample, after correcting for operating temperature and the source bandwidth, the best possible resolution $(\Delta E_{instrument})$ obtained was 62 meV [Foc (2024)].

2.6 Summary and Conclusion

The best possible resolution achieved in real space mode was 43 nm using Hg-lamp and 52 nm using a pulsed laser. The fluence of the laser pulses incident on the sample was kept small enough to ensure linear electron counts and avoid effects of space charge and non-linear photoemission that leads to degradation of image resolution. As a result, the acquisition time of images acquired using laser is approx. 20 times that of the image acquired using Hg lamp. The best possible resolution obtained is 7.4 $m\text{Å}^{-1}$ in k-space mode. For MTE measurements, the best possible resolution obtained is 0.2 meV corresponding to the MTE value of 25 meV. Lastly, for imaging energy filter, the best possible resolution obtained is 62 meV.

Chapter 3

QUANTUM EFFICIENCY, PHOTOEMISSION ENERGY SPECTRA AND MEAN TRANSVERSE ENERGY OF ULTRANANOCRYSTALLINE DIAMOND PHOTOCATHODE

This chapter was published in Ref. [Kachwala *et al.* (2022b)]

3.1 Abstract

The quantum efficiency and mean transverse energy of electrons emitted from a cathode determine the quality of beams generated from photoinjectors. The nitrogen-incorporated ultrananocrystalline diamond, (N)UNCD, is a new class of robust semiconductor photocathodes which has been considered in photoinjectors for high peak current extraction. In this work, we measure the spectral response in quantum efficiency, photoemission energy spectra and mean transverse energy of the (N)UNCD photocathode using a photoemission electron microscope. The observed quantum efficiency was comparable to that of copper photocathodes. Photoemission spectra showed the evidence of scattering of electrons before emission. This relaxation of electrons due to scattering is also observed in the spectral response of the mean transverse energy. The mean transverse energy is limited to $\sim$ 70 meV at the threshold. We attribute this to the physical and chemical roughness of the (N)UNCD photocathode and hence, smoother films will be required to further reduce the mean transverse energy obtained from the (N)UNCD photocathode.

3.2 Introduction

High-density bunched electron beams required for accelerators in X-ray Free Electron Lasers (XFELs), [Emma *et al.* (2010)] Ultrafast Electron Diffraction and Microscopy experiments, [Kim *et al.* (2020b)] Inverse Compton Scattering X-ray sources [Graves *et al.* (2014)] etc. are typically produced using photoinjectors. Photoinjectors essentially consist of a photoemissive material (photocathode) placed in a large accelerating field which is typically in the range of 5 - 100 MV/m depending on the design of the photoinjector. The performance of a photocathode is usually characterized by the emitted charge or, equivalently, the quantum efficiency (QE). The cathode must also have a long lifetime, fast response time and low intrinsic emittance. QE is defined as the number of electrons emitted per incident photon. High-QE photocathodes are desirable for applications that require high average current or high bunch charges and to mitigate the effects of non-linear photoemission.

The response time of a photocathode is given in terms of the extracted electron bunch length when compared to the incoming laser pulse. Photocathodes require a fast response time to temporally shape the initial electron distribution and maintain the beam quality during acceleration in the photoinjector. A fast response time implies that the electrons are emitted quickly after the absorption of incident photon energy. However, electrons excited deep within the cathode surface can take tens of pico-seconds to escape into the vacuum leading to undesirable temporal structure. A fast response time ($<$1 ps) is desirable for various photoinjector applications [Lessner *et al.* (2017)]

The intrinsic emittance of a photocathode is expressed in terms of rms laser spot size and a mean transverse energy (MTE) of the emitted electrons and is given by the following equation:

$$\varepsilon_{n,x} = \sigma_{l,x}\sqrt{\frac{\mathrm{MTE}}{m_e c^2}}, \tag{3.1}$$

where $\varepsilon_{n,x}$ is the normalized transverse emittance in the x-z plane, $\sigma_{l,x}$ is the rms laser spot size in the x-direction, m_e is the mass of an electron and c is the speed of light. The MTE of the electrons depends on the cathode material, its surface morphology as well as the laser photon energy and fluence used for excitation [Dowell *et al.* (2010)]. For the case of metal photocathodes, the MTE of the emitted electrons follow the Dowell-Schmerge model which says that the MTE of the electrons scales as one-third of the excess energy (difference between the photon energy and work function) and at the threshold is limited by the thermal limit [Dowell and Schmerge (2009a)]. For example, the smallest MTE of 25 meV was demonstrated for antimony films when operated near the threshold at room temperature [Feng *et al.* (2015)]. For the semiconductor photocathode such as GaAs activated to negative electron affinity using Cs and NF_3, the observed value of MTE is 40 meV at room temperature [Bazarov *et al.* (2008)]. However, in most photoinjectors, the MTE extracted from photocathodes is in the range of 0.1 - 1 eV [Dowell *et al.* (2010)].

Another parameter that determines the MTE of the emitted electron beam is the physical roughness and work function variation (also termed as chemical roughness) of a photocathode. Nano-scale physical roughness on the cathode results in increase in MTE and this can be attributed to two effects. First is the ‘slope effect’ where the electrons are emitted from the local surface normal of the photocathode as opposed to its global surface normal. The second, known as the ‘field effect’, arises due to generation of a transverse local electric field due to the roughness on the photocathode surface. In general, the field effect dominates as compared to the slope effect and ergo the slope effect is usually ignored in the analysis. The detailed analysis of MTE increase due to physical roughness has been previously reported [Zhang and Tang (2015); Qian *et al.* (2012); Feng *et al.* (2017); Smedley *et al.* (2015)]. Assuming the sinusoidal variation in the surface roughness profile, the scaling of MTE to the first order is given by the following equation:

$$\mathrm{MTE}_{\mathit{field}} \propto \frac{Ea^2}{\lambda}, \tag{3.2}$$

where E is the applied electric field, a is the amplitude and λ is the period of the physical roughness profile. As we can see, the contribution to MTE due to physical roughness increases with increasing accelerating field gradient. The chemical roughness arises due to lateral potential variations which is the result of the varying work function. It has been shown that the effect of chemical roughness becomes less prominent with increasing accelerating field gradient [Karkare and Bazarov (2015)]. The combined effect of physical and chemical roughness has been calculated by Gevorkyan et al. by decomposition of electric field components close to the cathode surface and numerically tracking the trajectory of the emitted electron in the applied electric field [Gevorkyan *et al.* (2018)].

Another factor that determines the choice of a photocathode in a photoinjector is its lifetime/robustness. Many emerging applications such as Free Electron Lasers (FELs), Linear Accelerators (LINACs) and Relativistic Heavy Ion Collider (RHIC) experiments require high peak current along with high-quality electron beams [Drees (2006)]. High-brightness photocathodes such as GaAs, which have low MTE and high QE, tend to have a longer lifetime when operated at low peak currents. However, it degrades very quickly when operated at high peak currents [Grames *et al.* (2011); Suleiman *et al.* (2018)]. For high peak current applications, one requires a photoemissive material with high conductivity. A wide-bandgap semiconductor such as diamond is a promising candidate for such applications because of its mechanical, thermal, and electrical stability along with an intrinsically fast response time ($\sim$100 fs) [Liu *et al.* (2014); Schneider (2022)]. Moreover, its vacuum robustness allows it to work under harsh conditions and thus makes it a promising candidate for photoinjector applications. A comparison between the emission properties of single-, micro-, nano-, and graphite-like nano-crystalline diamond films suggests that graphite-like nano-crystalline diamond has better performance compared to the others. The QE of graphite-like nano-crystalline diamond was reported to be 10^{-4} at 200 nm [Nitti *et al.* (2008)]. However, none of these films showed a good performance above 200 nm.

One way to improve the performance of diamond at wavelengths $>$200 nm, is to take advantage of the negative electron affinity (NEA) of the diamond. A way to do so would be by *n*-doping of the diamond films and surface treatment in a hydrogen environment [van der Weide *et al.* (1994)]. Recently, *n*-doping of micro, nano and ultrananocrystalline diamond (UNCD) films using nitrogen has been performed by many groups [Pinault *et al.* (2007); Mengui *et al.* (2015); Shen and Chen (2007)]. It has been shown that addition of nitrogen to UNCD films increased its electrical conductivity upto 1854 S cm^{-1} and the maximum current density to 8 mA cm^{-2} [Yuan *et al.* (2016)]. This is advantageous for high peak current photoinjector applications. Such films with nitrogen incorporation are termed as nitrogen-incorporated ultrananocrystalline diamond (N)UNCD. (N)UNCD typically consists of sp^2 as well as sp^3 bonded carbon atoms. The sp^2 bonded carbon phase, also known as the graphitic phase, resides in the grain boundary region of sp^3 bonded carbon phase, also known as the diamond phase. It has been reported that the photemission of electrons from such materials originates from the sub-nm scale grain boundaries which are predominantly composed of sp^2 bonded carbon atoms [Harniman *et al.* (2015)]. In addition, the NEA can be introduced in (N)UNCD after synthesis via surface hydrogenation treatment leading to the surface C–H dipole formation. Such cathodes are known as hydrogen-terminated nitrogen-incorporated ultrananocrystalline diamond [(N)UNCD:H].

The QE of (N)UNCD:H as well as (N)UNCD has been reported by many groups. It was observed that the QE of (N)UNCD:H was two orders of magnitude higher than the QE of (N)UNCD which was $\sim 10^{-5}$ at 254 nm [Pérez Quintero *et al.* (2014)]. However, not many experimental measurements of the MTE of (N)UNCD have been reported. A recent experimental measurement of MTE of (N)UNCD:H by Chen et al. using solenoid scan technique at the electric field of 0.45 MV/m suggests that the MTE of (N)UNCD:H is constant at 266 meV with decreasing photon energy [Chen *et al.* (2019)]. Another experimental measurement of MTE of an (N)UNCD was performed in an RF gun environment at the electric field of 30 MV/m. The normally incident 262 nm laser had a Gaussian longitudinal distribution with a full width at half maximum pulse length of 300 fs. The measured MTE was reported to be $\sim$ 1000 meV [Chen *et al.* (2020)].

In this work, we report proof-of-concept QE, photoemission spectra and MTE measurements for the (N)UNCD photocathode grown on a molybdenum substrate. The measurements were carried out in the near UV range of 200 – 300 nm, standard for many photocathode applications. Further, the measurements were performed for (N)UNCD photocathode prior to bakeout and after the bakeout of the sample. The bakeout was performed at 120° C for 24 hours. The QE of the baked sample was higher than the QE of the unbaked sample by an order of magnitude for the same range of photon energies. In the photoemission energy distribution spectra, the sum of work function and kinetic energy corresponding to the maxima in the emission spectra does not match the excitation energy. This indicates that the scattering of electrons influence the emission. The measured MTE approximately scales as the one sixth of the excess energy. It is proposed that this trend in MTE is due to the relaxation of electrons possibly via phonon scatterings in the conduction band before emission. The MTE of $\sim$ 70 meV close to the threshold is attributed to the physical and chemical roughness of the (N)UNCD photocathode.

3.3 Experimental Section

The diamond deposition process for synthesis of (N)UNCD films was performed by Advanced Diamond Technologies. Details of different steps for the preparation of (N)UNCD are reported elsewhere [Kim *et al.* (2018)]. Typically, it has 1 μm layer of conductive (N)UNCD film, followed by a layer of 15 μm microcrystalline diamond. Diamond film is brazed to a polished Mo substrate using the brazing material TiCuSil. Figure 3.1 shows the Raman spectrum of an (N)UNCD sample measured using a custom built Raman spectrometer in a 180° geometry. The sample was excited using a 150 mW Coherent Sapphire SF laser with a 532 nm laser wavelength. The laser power was controlled using a neutral density filters wheel and an initial laser power of 100 mW. The laser was focused onto the sample using a 50X super long working distance plane APO Mitutoyo objective with a numerical aperture of 0.42. The signal was discriminated from the laser excitation using an Ondax® SureBlock™ ultranarrow-band notch filter combined with two optigrate notch filters. The broad peaks at 1350 cm^{-1} and 1550 cm^{-1} correspond to the D and G bands of diamond and graphite, respectively.

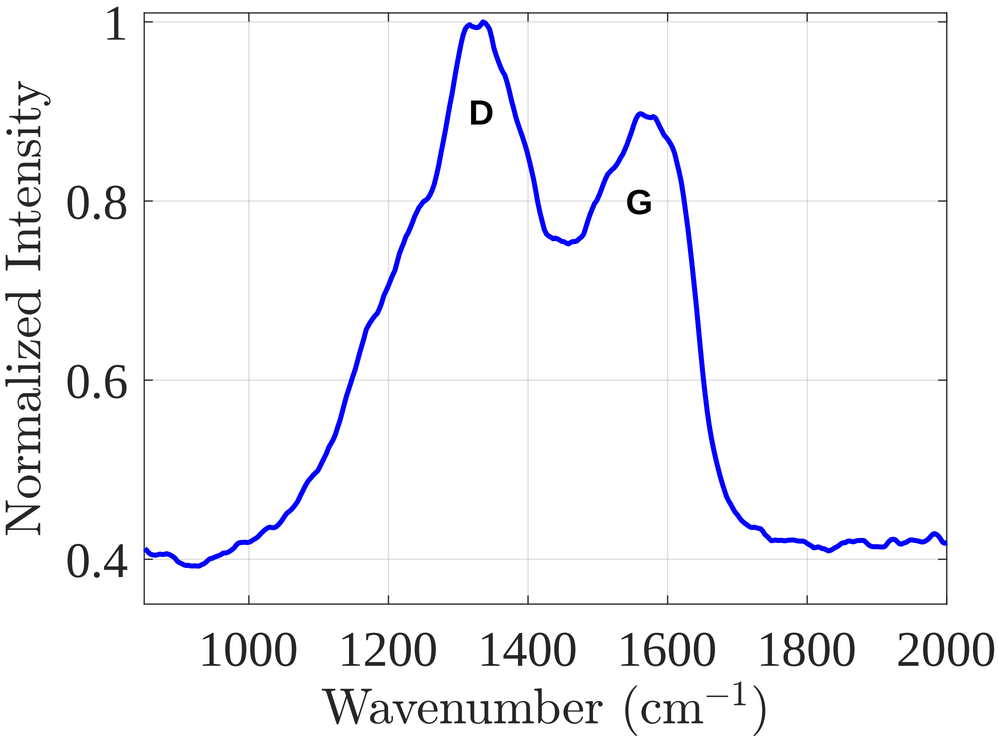

Figure 3.1: Raman spectrum of the (N)UNCD sample showing a characteristic disordered diamond (D) peak and graphite (G) peak.

QE, photoemission spectra and MTE measurements of the (N)UNCD sample were performed using a photoemission electron microscope (PEEM) [Foc (2024)]. The base pressure of the PEEM chamber was in the low 10^{-10} torr range during the measurements.

QE measurements were performed using a 500 kHz repetition rate femtosecond pulsed laser with a pulse length of 150 fs from a pulsed Optical Parametric Amplifier (Light Conversion Orpheus pumped by Light Conversion Pharos). The LASER was made incident onto the sample at 65° angle of incidence with respect to the normal of the sample surface and was focussed by a lens down to the spot size of 100 μm × 250 μm. One millimeter real space field of view (significantly larger than the LASER spot size) was selected to image all the emitted photo-electrons using a double micro channel plate (MCP) detector at the end of the PEEM column. The photoelectron current was determined by recording counts/second on the MCP detector and using a predetermined calibration factor to convert it into photocurrent at each wavelength.

The photoemission spectra were obtained by using the imaging energy filter (IEF) capability of the PEEM. The IEF unit is placed after the PEEM column and before the imaging unit of the microscope. It consists of two pre-retardation lens and two retardation grids that forms the retarding field analyzer (RFA). The retarding field acts as the high pass energy filter that allows for energy filtered imaging. Background subtracted energy filtered images were obtained for the (N)UNCD sample using RFA of the PEEM with sub 65 meV energy resolution. The contrast aperture (CA) of diameter 1750 μm placed in the backfocal plane of the objective lens in the PEEM column was selected to ensure transmission of all the emitted electrons from the sample surface. After acquiring the energy filtered images, a numerical differentiation of high pass spectrum of the RFA was performed and the normalized counts were plotted against the kinetic energy of emitted electrons for each photon energy for both, baked and unbaked samples.

MTE measurements were performed by operating PEEM in k - space mode with a sub

8 - $m\text{Å}^{-1}$ k - space resolution. A 35±5 μm region of the sample was selected by the adjustable iris aperture that was placed in the first intermediate image plane of the PEEM column while imaging in the real space mode. After limiting the area under investigation in the real space mode by adjutable iris aperture, its counterpart in the k - space mode was imaged by changing the projective settings of the PEEM. Figure 3.2 shows k - space images taken at 240 nm with FOV of 1.9 Å^{-1} and 3.9 Å^{-1} and the Gaussian fit applied to the k_x and k_y distributions obtained from 1.9 Å^{-1} FOV. The MTE was then calculated using the second moment obtained from the Gaussian fit applied to the measured k - space distribution of the emitted electrons using the following equation:

$$\mathrm{MTE} = \frac{\hbar^2 \sigma^2}{2m}. \tag{3.3}$$

Here, $\hbar$ is the reduced Planck's constant, m is the mass of an emitted electron and $\sigma = \sqrt{{\sigma_{k_x}}^2 + {\sigma_{k_y}}^2}$, where σ_{k_x} and σ_{k_y} are the second moments obtained from the Gaussian fit applied to k_x and k_y distributions of the emitted electrons as shown in Figures 3.2 (c) and 3.2 (d).

For all the measurements, the fluence of the laser pulses incident on the sample was kept small enough to ensure linear electron counts and avoid effects of space charge and non-linear photoemission. The QE was measured at the extraction field of 0.005 MV/m and the photoemission spectra and MTE were measured at the extraction field of 0.5 MV/m. For the case of semiconductor, according to Stratton, [Stratton (1962)] the Schottky work function lowering is given by the following equation:

$$\Delta\Phi = \sqrt{\alpha \hbar c e E (K_s - 1)/(K_s + 1)}, \tag{3.4}$$

where α is the fine structure constant, e is the electron charge and K_s is the dielectric constant. Assuming $K_s = 5.7$, typical for diamond, [Die (2024)] and the maximum extraction field of 0.5 MV/m on the (N)UNCD photocathode surface in the PEEM,

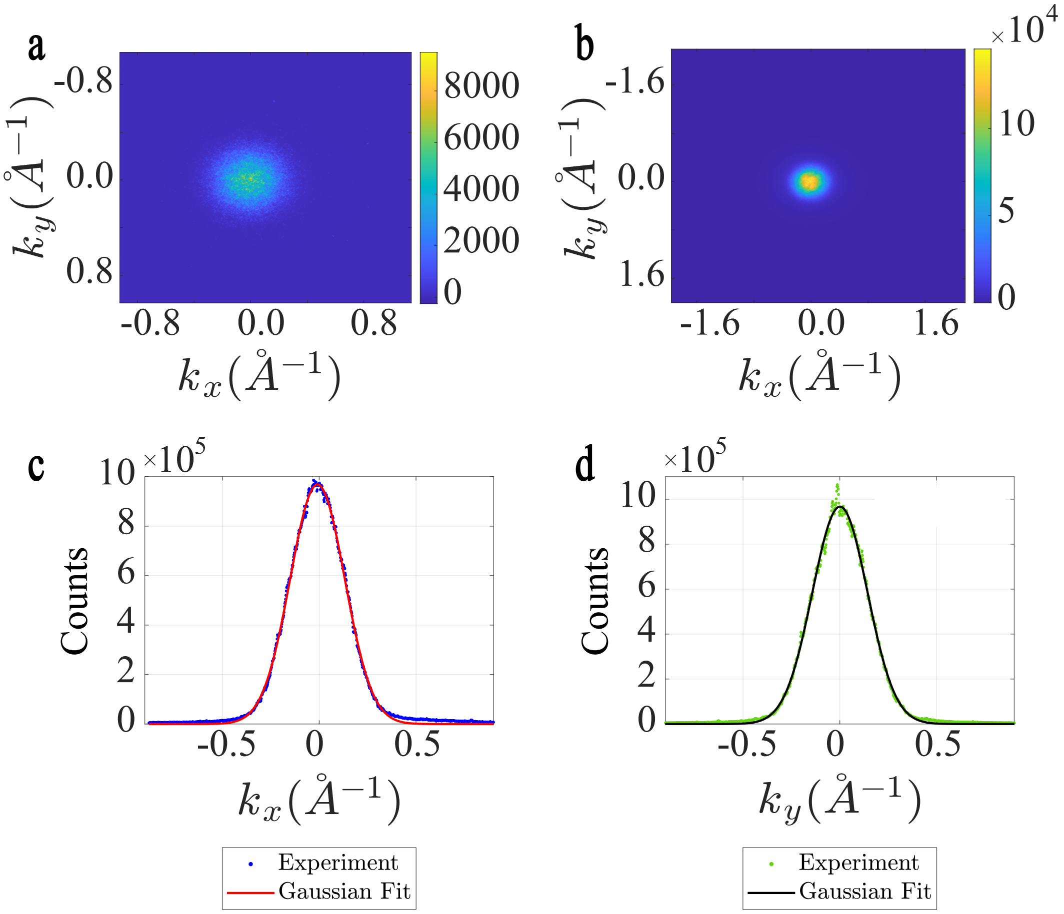

Figure 3.2: k - space images taken at 240 nm with FOV of (a) 1.9 $\AA^{-1}$ and (b) 3.9 $\AA^{-1}$. (c) Gaussian fit applied to the k_x distribution obtained from 1.9 $\AA^{-1}$ FOV and (d) Gaussian fit applied to the k_y distribution obtained from 1.9 $\AA^{-1}$ FOV.

equation 3.4 results in a Schottky work function lowering effect of only 22.47 meV that is comparable to the thermal energy at the room temperature. QE, photoemission spectra and MTE measurements were performed in the near UV range of 200 – 300 nm standard for many photocathode applications.

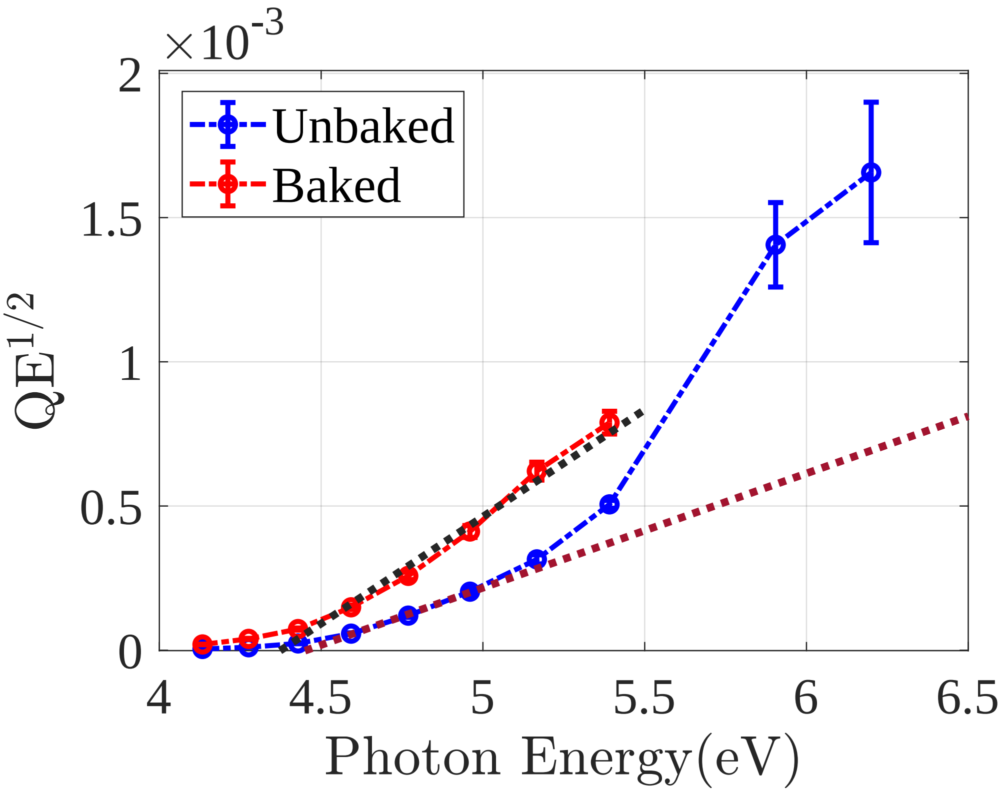

Figure 3.3: Experimentally determined QE from the (N)UNCD samples: for the unbaked sample and baked sample which was baked at 120° C for 24 hours. Dotted line is a linear fit indicating 4.4±0.1 eV threshold from the unbaked (brown) and baked (black) sample.

3.4 Results and Discussions

3.4.1 QE Measurements

According to the Dowell-Schmerge model [Dowell and Schmerge (2009a)], for photoemission near threshold, the quantum efficiency is given by the following equation:

$$\mathrm{QE} \propto (\hbar\omega - \Phi)^2, \tag{3.5}$$

where $\hbar\omega$ is the photon energy and Φ is the work function of a photocathode. Hence on plotting the square root of QE vs photon energy, the x-intercept gives the work function of a photocathode sample. Figure 4.3 shows experimentally determined square root of QE values for the (N)UNCD sample. There are four main features in Figure 4.3. First, the QE of the baked sample is higher than the QE of the unbaked sample for the same range of photon energies. This enhancement in QE can be attributed to the desorption of contaminant layers from the (N)UNCD surface during the bake-out. Second, the QE of the unbaked (N)UNCD sample is of the order of 10^{-8} and that of the baked sample is of the order of 10^{-7} at 4.9 eV photon energy. These values are comparable to the previously reported values [Pérez Quintero *et al.* (2014)]. Third, the photoemission threshold for both unbaked and baked sample is observed at the photon energy of 4.4 ± 0.1 eV. This is comparable to the previously reported values [Chen *et al.* (2019, 2020)]. Last, there is significant rise in QE beyond 5.4 eV photon energy. Since the band gap of diamond is 5.4 eV [Wort and Balmer (2008)], this increase in QE can be attributed to a higher number of electrons being excited in the conduction band when the photon energy is greater than the band gap of diamond.

3.4.2 Photoemission Spectra

Figure 4.1 shows experimentally determined photoemission spectra for the (N)UNCD sample before and after the bakeout of the sample. For a given photon energy, the energy spectra appear identical for both baked and unbaked sample. For both baked and unbaked sample, the photoemission spectra broaden in kinetic energy with the increasing photon energy. The top x-axis in Figure 4.1 shows the sum of kinetic energy (E_k) of the emitted electrons and the work function (Φ) of the (N)UNCD photocathode. Considering the work function of the (N)UNCD to be $\sim$4.4 eV, as obtained from the QE spectral response in Figure 4.3, the sum of the maximum kinetic energy of the emitted electrons and the work function approximately equals to the photon energy. Also, from the top x-axis in Figure 4.1, we can see that the sum of the work function and the kinetic energy corresponding to the maximum of the energy distribution curves does not coincide with that of the photon energy. This indicates that the electrons are scattered possibly by phonons before being emitted from the (N)UNCD sample. A similar electron scattering mechanism is observed for nitrogen-doped diamond films [Sun *et al.* (2011)] and other semiconductor photocathodes [Karkare *et al.* (2013)]. In the case of an unbaked sample, at 4.13 eV photon energy, the emission spectrum is broadened due to non-linear photoemission. This non-linear photoemission is also reflected in the MTE plot shown in Figure 4.2 which results in an increase in MTE at 4.13 eV photon energy [Knill *et al.* (2021)]

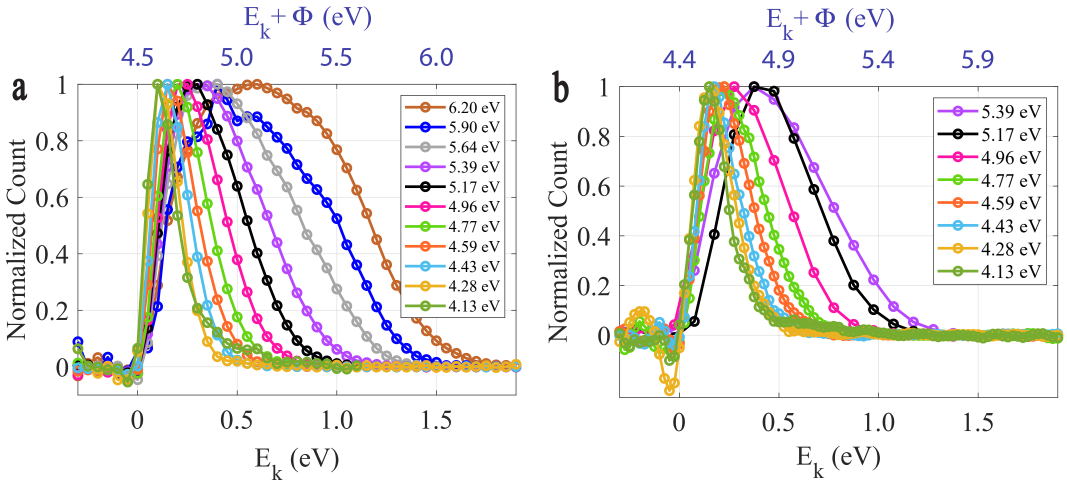

Figure 3.4: Photoemission spectra at different incident photon energies for the (N)UNCD samples: for (a) unbaked sample and (b) baked sample which was baked at 120 °C for 24 hours. The bottom x-axis represents the kinetic energy of the emitted electrons and the top x-axis represents the sum of the kinetic energy of the emitted electrons and the work function (Φ) of the photocathode sample.

3.4.3 MTE Measurements

MTE spectral response

Figure 4.2 shows experimentally determined MTE values for the (N)UNCD samples. There are three main features in Figure 4.2. First, the MTE of the (N)UNCD decreases with decrease in excess energy and shows a flat trend close to the threshold which is observed at a photon energy ∼4.4 eV. This is in contrast to the constant MTE of 266 meV for (N)UNCD:H reported by Chen et al [Chen *et al.* (2019)]. for a similar spectral range.

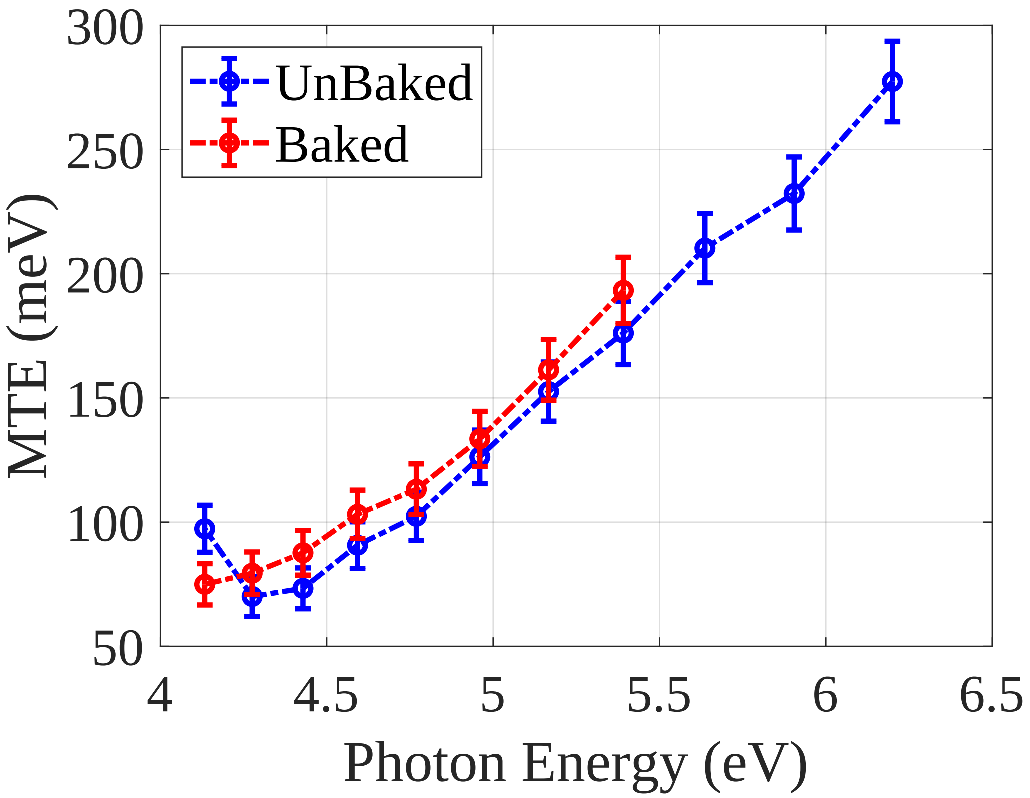

Figure 3.5: Experimentally determined MTE from the (N)UNCD samples: for unbaked sample and baked sample which was baked at 120° C for 24 hours.

Also, the MTE at 260 nm (4.76 eV photon energy) was observed to be ∼100 meV. This is an order of magnitude smaller when compared to the MTE observed by Reference [Chen *et al.* (2020)] at 262 nm and 30 MV/m electric field gradient on the surface of the cathode. Second, the scaling of MTE with excess energy is not in accordance with the Dowell-Schmerge model [Dowell and Schmerge (2009a)]. This behaviour can be attributed to the relaxation of electrons possibly with phonon scattering in the conduction band before emission. A similar behaviour is observed for other semiconductor photocathodes [Karkare *et al.* (2013)]. Last, the MTE at the threshold does not reach 25 meV (thermal limit) but flattens at ∼70 meV. This is attributed to the physical and chemical roughness of (N)UNCD photocathodes and is discussed in detail in the following section.

Dependence of MTE on physical and chemical roughness

A detailed discussion of the effect of physical and chemical roughness of the photocathode on the MTE of the emitted electrons is done in Section 3.2. The effect of physical roughness on the MTE due to the applied electric field is given by Equation 3.2. For the case of UNCDs, the amplitude of physical roughness varies between 5 - 10 nm [Booth *et al.* (2011); Gujrati *et al.* (2021); Auciello *et al.* (2022)] and the period of the roughness corresponds to the grain size which is generally reported to be in the range of 5 - 15 nm [Tóth *et al.* (2018); Rani *et al.* (2018); Chubenko *et al.* (2019)]. The contribution of MTE_{field} as a function of surface rougness is plotted for different periods typical of UNCD photocathodes in Figure 3.6. The MTE_{field} was plotted for two values of the electric field. First, 30 MV/m, which was the field gradient at the surface of the (N)UNCD reported in Reference [Chen *et al.* (2020)]. Second, 0.5 MV/m (inset of Figure 3.6) which was the field gradient at the surface of the (N)UNCD films during our measurements of MTE. The MTE_{field} obtained at 30 MV/m is larger than the thermal limit ($\sim$25 meV) and is comparable to the previously reported value [Chen *et al.* (2020)]. In addition, the contribution of MTE_{field} at 0.5 MV/m shown in the inset of Figure 3.6 is $\sim$25 meV for $a = 10$ nm and $\lambda = 10$ nm.

As discussed in Section 3.2, another source of increase in MTE is the chemical roughness of the photocathode. From Figure 3.1, there are two phases present in the (N)UNCD sample. First, the diamond phase and second, the graphite phase. These two phases can have work function difference of several 100s meV. If we consider $\sim$1 nm graphite regions between $\sim$10 nm diamond grains, the variation of several 100s meV in surface potential can have additional contribution to the MTE at 0.5 MV/m electric field [Karkare and Bazarov (2015); Gevorkyan *et al.* (2018)].

In general, for practical photocathodes with physical and chemical roughness, the MTE

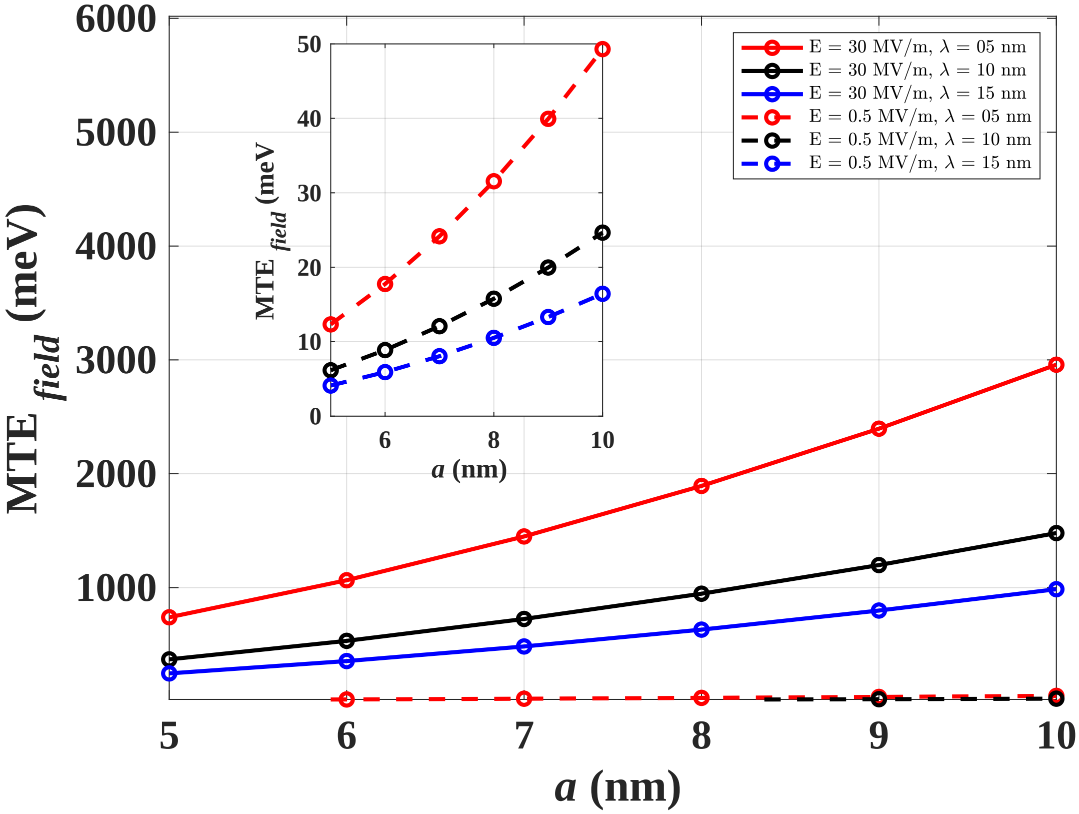

Figure 3.6: Variation of MTE$_{field}$ with a. The calculations are done for λ = 5, 10 and 15 nm and electric field gradients of 30 MV/m and 0.5 MV/m (inset figure).

of the emitted electrons is given by:

$$\text{MTE} = \text{MTE}_{kT} + \text{MTE}_{field} + \text{MTE}_{WF}, \tag{3.6}$$

where MTE$_{kT}$ is the contribution due to thermal limit which is ∼25 meV at room temperature. Assuming a = 10 nm and λ = 10 nm, which is typical for UNCDs, the contibution of MTE$_{field}$ at 0.5 MV/m is ∼25 meV. And lastly, MTE$_{WF}$ is the contribution due to the chemical roughness arising from several 100s meV variation in surface potential due to the presence of graphite phase and diamond phase in the (N)UNCD sample. Hence, the total MTE which is the sum of MTE$_{kT}$, MTE$_{field}$ and MTE$_{WF}$ is ∼70 meV at the threshold for the (N)UNCD photocathodes which is in agreement with what is shown in Figure 4.2.

3.5 Summary and Conclusion

We measured the QE, photoemission spectra and MTE of a (N)UNCD photocathode in the UV range of 200 nm - 300 nm for unbaked and baked samples. The QE was measured to be $\sim 10^{-7}$ for a baked sample and $\sim 10^{-8}$ for an unbaked sample at 250 nm. From the photoemission spectra we observed that the sum of work function and kinetic energy corresponding to the maxima in the emission spectrum does not match the excitation energy. This indicates that the scattering of electrons influence the emission. The MTE decreased with the decrease in excess energy and showed a flat trend near the threshold. This behaviour is in contrast to the constant MTE of 266 meV reported for an (N)UNCD:H for a similar spectral range [Chen *et al.* (2019)]. The MTE at 260 nm (4.76 eV photon energy) was observed to be $\sim$100 meV. This is an order of magnitude smaller than the MTE reported by Reference [Chen *et al.* (2020)]. We attribute this difference to the physical roughness of the (N)UNCD photocathode. The scaling of MTE with excess energy is not in accordance with the Dowell-Schmerge model [**?**. This observed trend in MTE is attributed to the relaxation of electrons possibly with phonon scattering in the conduction band before emission [Karkare *et al.* (2013)]. This scattering of electrons before emission is also evident in the photoemission spectra shown in Figure 4.1. Furthermore, the MTE at the threshold does not go to 25 meV (thermal limit) but flattens at $\sim$70 meV. This is attributed to the physical roughness due to the fabrication process and chemical roughness which is a result of the work function variation due to the presence of graphite phase and diamond phase in the (N)UNCD sample [Karkare and Bazarov (2015); Gevorkyan *et al.* (2018)]. The work function of the (N)UNCD obtained from the spectral response of QE and MTE was 4.4±0.1 eV. This is in agreement with the previously reported values [Chen *et al.* (2019, 2020)].

In summary, we have reported the spectral responses of QE, photoemission spectra and MTE of the (N)UNCD photocathode. With the QE comaparable to that of metal photocathodes and MTE of 70 meV at the threshold, (N)UNCD photocathodes are suitable for various high peak current photoinjector applications. However, use of these photocathodes at high electric field gradients can significantly increase the MTE of the emitted electrons owing to their surface roughness. Consequently, it can lead to decrease in brightness of the emitted electron beams. Even at low electric fields, the contribution to MTE due to physical and chemical roughness is significant enough to increase MTE beyond the thermal limit at the threshold. One way to reduce MTE and consequently increase the brightness of (N)UNCD photocathodes is by optimizing the growth techniques to produce a smoother film. One way to do this would involve growing (N)UNCD films via tungsten interlayers [Naguib *et al.* (2006)]. As a result, future work would involve growing (N)UNCD films with reduced surface roughness and additional fundamental understanding of their emission mechanism.

Chapter 4

DEMONSTRATION OF THERMAL-LIMIT MEAN TRANSVERSE ENERGY FROM CESIUM ANTIMONIDE PHOTOCATHODES

This chapter was published in Ref. [Kachwala *et al.* (2023b)]

4.1 Abstract

The mean transverse energy (MTE) of electrons emitted from cathodes is a critical parameter that determines the brightness of electron beams for applications such as x-ray free electron lasers, particle colliders, and ultrafast electron scattering experiments. Achieving a MTE close to the thermal limit is a key step toward realizing the full potential of electron sources in these applications. Cesium antimonide (Cs_3Sb) is a technologically important material with a long history of use in photon detection and electron sources. The smallest MTE of electrons photoemitted from Cs_3Sb has always been appreciably greater than the thermal limit and was attributed to surface non-uniformities. In this work, we present comprehensive measurements of the photoemission electron energy spectra (PEES), quantum efficiency (QE) and MTE from Cs_3Sb in a wide photoexcitation energy range from 1.5 eV to 2.3 eV. Our PEES measurements demonstrate a notably low photoemission threshold of around 1.5 eV, which is in contrast with the previously perceived threshold of 1.8-2.0 eV. Moreover, we show that the MTE at this threshold of 1.5 eV, nearly converges to the thermal limit at 300 K. At 1.8 eV, the MTE measured is 40 meV, which is comparable to the previously reported value. We conclude that this MTE value at 1.8 eV photon energy is not due to surface roughness effects as previously believed, but is a direct consequence of the excess

4.2 Introduction

A wide range of linear-accelerator applications like x-ray free electron lasers (XFEL) [Emma *et al.* (2010)], ultrafast electron diffraction (UED) [Sciaini and Miller (2011)] and energy recovery linacs (ERL) Gruner *et al.* (2002) require dense and coherent electron beams for their operation. High-density-bunched electron beams required for the operation of the above-mentioned instruments are typically produced using photoinjectors. Photoinjectors essentially consist of a photoemissive material (photocathode) placed in a large accelerating field gradient, which is typically in the range of 1-100 MV/m, depending on the design of the photoinjector [Power (2010); Russell (2003)].

The performance of the photocathode used for photoinjector applications is dependent on the quality of the electron-bunch generated from it. A figure of merit that determines the quality of electron-bunch is given by the the brightness of the electron bunch. The maximum achievable brightness of the electron bunch in a photoinjector scales according to the following relation [Bazarov *et al.* (2009)]:

$$B \propto \frac{\mathscr{E}^n}{\mathrm{MTE}}, \tag{4.1}$$

where n is the real number between 1 and 2, $\mathscr{E}$ is the applied electric field at the cathode surface and MTE is the mean transverse energy of the emitted electrons. The maximum possible electric field is set by the design of a photoinjector and is limited by the maximum charge density that can be extracted from a photocathode without degrading the brightness. Therefore, achieving the minimal possible MTE is a significant milestone in the ongoing efforts to optimize the performance of electron sources in the aforementioned applications.

The MTE is a property of a cathode material, its surface morphology, the drive laser wavelength and laser fluence [Dowell *et al.* (2010)]. The MTE from the cathodes is typically proportional to one-third of the excess energy when the emitted electron bunch is not space charge dominated. [Dowell and Schmerge (2009b); Saha *et al.* (2023)] Here, the excess energy is defined as the difference in energy between the incident photon energy and the work function of the material. For photon energies close to the threshold i.e. low or negative excess energies, the MTE gets limited by the Fermi tail of the electron distribution to k_BT [Vecchione *et al.* (2013)], where k_B is the Boltzmann constant and T is the lattice temperature of the cathode. The thermal limit of k_BT has been experimentally demonstrated for polycrystalline Sb thin films at room temperature [Feng *et al.* (2015)]. There has also been experimental demonstration of a record low MTE of 5 meV from cryo-cooled surface of Cu(100) [Karkare *et al.* (2020)] and a low MTE of 10 meV at 77 K from graphene-coated Cu(110) [Knill *et al.* (2023b)]. However, metal cathodes due to their very low quantum efficiency (QE) in the range of 10^{-6}-10^{-8} at threshold energies, are inefficient electron sources for many photoinjector applications [Dowell *et al.* (2010); Musumeci *et al.* (2018)]. Given the low QE, higher laser fluences need to be used to extract the required charge densities, resulting in non-linear photoemission processes [Maxson *et al.* (2017); Bae *et al.* (2018)]. Such non-linear processes increase the MTE to few 100's of meV, thereby significantly reducing the brightness of the emitted electron bunches.

One way of circumventing the MTE degrading effect of non-linear photoemission is by the use of high QE, low electron-affinity semiconductor cathodes like alkali and bi-alkali antimonides such as Cs_3Sb, K_2CsSb, Na_2KSb etc. Due to their relatively high QE exceeding 1% in the visible wavelength range, this class of semiconductor photocathodes has emerged as potential candidates for the next generation light sources for accelerator applications. The intrinsic property of high QE of alkali-antimonides has been leveraged to generate the highest average current [Dunham *et al.* (2013)]. A low MTE has been achieved from alkali-antimonide photocathodes by illuminating them with near-threshold photons, at room and cryogenic temperatures [Cultrera *et al.* (2015)] However, alkali-antimonide are typically grown as polycrystalline thin films with nanoscale surface roughness. The roughness and the resulting work function variations along with material defect states can limit the smallest achievable MTE from alkali-antimonides [Gevorkyan *et al.* (2018); Saha *et al.* (2023)]

Of all the high QE alkali-antimonides, Cs_3Sb has the least number of constituent elements, which makes its growth process the easiest. Therefore, Cs_3Sb photocathodes have been studied extensively in order to investigate their photoemission properties and achieve smooth, well-ordered surfaces. Using the co-deposition technique on single crystalline strontium titanate substrates, atomically flat and uniform surfaces of Cs_3Sb have been achieved [Saha *et al.* (2022)]. Recently, growth of a single crystal film of Cs_3Sb on 3C-SiC has been demonstrated [Parzyck *et al.* (2022a)]. It was expected that such surfaces would result in the MTE limited by k_BT at the threshold along with a high QE (0.01%).

Based on the knee observed in the log plot of the QE spectral response, previous works have deduced the photoemission threshold of the Cs_3Sb cathodes to be 1.8-2.0 eV [Cultrera *et al.* (2011, 2015); Saha *et al.* (2022)]. At this perceived threshold, the MTE from the Cs_3Sb cathodes was measured to be 40 meV at 300 K and 22 meV at 90 K, significantly larger than the thermal limit of 26 meV and 8 meV, respectively. This larger MTE has been attributed to the surface roughness effects [Feng *et al.* (2017); Smedley *et al.* (2015); Karkare and Bazarov (2015); Gevorkyan *et al.* (2018)] and bulk defect density of states [Spicer (1958); Saha *et al.* (2023)].

In this paper, we present detailed MTE, photoemission electron energy spectra (PEES) and QE measurements from Cs_3Sb films in the spectral range of 1.45-2.33 eV photon energy. This is a wider spectral range when compared with the previous works [Sakata (1953); Cultrera *et al.* (2011, 2015)]. Our PEES measurements conclusively show that the work function of Cs_3Sb cathodes is around 1.5 eV. Further, we show that at the threshold of 1.5 eV, the MTE does reach the k_BT value at room temperatures. Moreover, our measurements show that the higher than k_BT value of MTE measured and reported in previous works at 1.8 eV is not due to roughness/ surface non-uniformity effects and defect density of states, but is simply an effect of the excess energy at 1.8 eV. Our measurements also show that the MTE doesn't follow the (excess energy)/3 trend as was previously thought to be the case based on a threshold of 1.8-2.0 eV. The values of MTE measured are significantly lower owing to the energy losses due to strong scattering effects during the transport of the excited electrons to the surface before emission [Karkare *et al.* (2013)].

4.3 Experimental Details

The Cs_3Sb cathodes studied in this paper were grown on 2 substrates: doped silicon (Si) and Nb-doped strontium titanate (STO). Prior to the growth, the substrates were rinsed with isopropyl alcohol and annealed at 450 °C for 2-3 hours in an ultra-high-vacuum (UHV) chamber with a base pressure in the low 10^{-10} torr range. The Cs_3Sb cathodes were grown via co-deposition of Cs and Sb on the Si and STO substrates. By shining a green laser ($\lambda = 532nm$) at low enough power to prevent space charge and non-linear photoemission effects and keep the emitted current below 1 μA, the photocurrent emitted from the cathode was measured during the growth to calculate the QE. This serves as a feedback to monitor the growth and performance of the cathodes. The growth of the cathodes was terminated by turning down the source heaters once the QE began to plateau/drop. The final QE of the Cs_3Sb cathodes was between 3-4 % in green (λ = 530 nm). The two cathodes grown on Si and STO substrates were estimated to have a thickness of $\sim$ 40 nm.

Further details of the growth process can be found in Ref. [Saha *et al.* (2022)]. Based on previous AFM measurements, the film on Si is expected to have an rms roughness of $\sim$ 1.4 nm, whereas the growth on STO is expected to be significantly different and smoother with an rms roughness of $\sim$ 0.3-0.6 nm. The work function variations in Cs_3Sb cathode on STO are also smoother than that on Si [Saha *et al.* (2022)].

After growth, the two Cs_3Sb cathodes on Si and STO substrates were transported via a UHV transfer line into the photoemission electron microscope (PEEM), using which the QE, PEES and MTE measurements of the Cs_3Sb cathodes were performed [Foc (2024)]. The pressure in the transfer line was in 10^{-10} torr range and no QE degradation was observed during the transfer. The base pressure of the PEEM chamber was also in the low 10^{-10} torr range during the measurements. A detailed description of the measurement procedure can be found in Ref. [Kachwala *et al.* (2022b)]. All the measurements were performed using a 500 kHz repetition rate femtosecond pulsed laser with a pulse length of 150 fs generated from Optical Parametric Amplifier (Light Conversion Orpheus pumped by Light Conversion Pharos). The fluence of the laser pulses incident on the sample was kept small enough to ensure linear electron counts and avoid effects of space charge and non-linear photoemission.

4.4 Results and Discussion

Figure 4.1 shows an experimentally determined PEES for the Cs_3Sb cathodes on (a) Si and (b) Nb-doped STO substrates. For both the cathodes, the PEES broaden in kinetic energy with the increasing photon energy. The maximum kinetic energy of the emitted electrons was taken to be 1% of the maxima of the energy distribution curve. The value of 1% was chosen as it is the least value above the noise floor of the PEES. Taking the maximum kinetic energy to be 1% of the maxima of the energy distribution curve, the x-intercept from the plot of maximum kinetic energy vs photon energy gives us the work function (Φ) of the photocathode. This is shown in the inset of Figure 4.1. The value of Φ obtained from the PEES data is 1.5 eV, with an uncertainty of $\sim$ 0.1 eV (due to the resolution of the PEEM in measuring the PEES) in the measurement. This is in contrast to the work function of 1.8-2.0 eV that is typically assumed based on the QE spectral response [Cultrera *et al.* (2015); Saha *et al.* (2022)]. Such a low value of the work function has also been reported based on energy distribution measurements in the literature by Sakata [Sakata

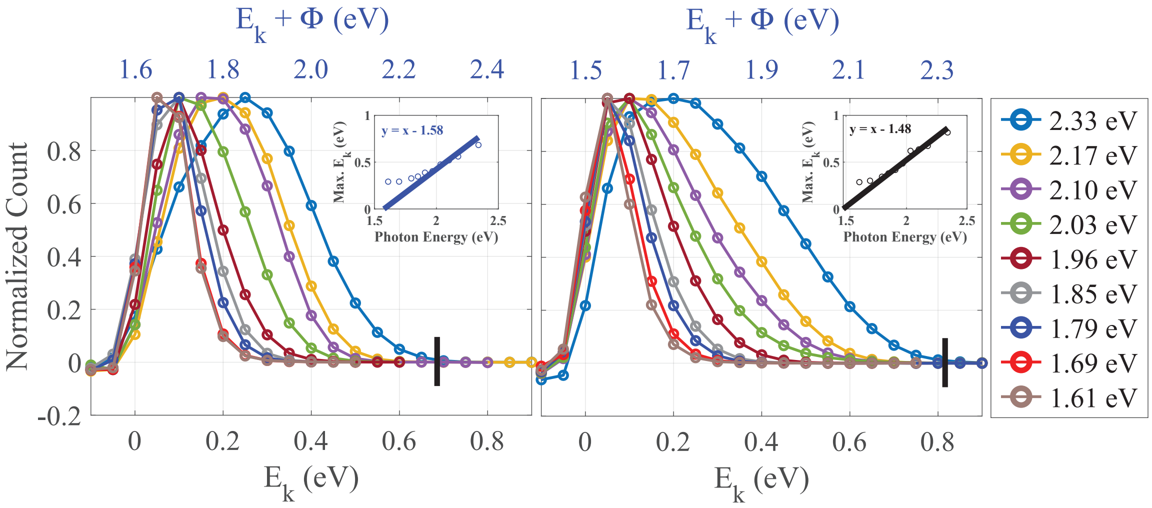

Figure 4.1: Photoemission electron energy spectra (PEES) at different incident photon energies for the Cs_3Sb film grown on: (a) Si and (b) doped STO substrates. The bottom *x*-axis represents the kinetic energy of the emitted electrons and the top *x*-axis represents the sum of the kinetic energy (E_k) of the emitted electrons and the work function (Φ) of the photocathode sample. The inset in each figure shows the plot of maximum kinetic energy vs photon energy. The maximum kinetic energy was taken at 1% of the maxima of the PEES. The black vertical tick on the x-axis corresponds to 1% of the maxima of the PEES for the photon energy of 2.33 eV. The 1% of the maxima of the PEES is different for different photon energies.

(1953)].

The low work function $\Phi \sim (1.5 \pm 0.1)$ eV has been further corroborated by the MTE data measured from the Cs_3Sb cathodes. Figure 4.2 shows the spectral response of the MTE measured at room temperature from the Cs_3Sb cathodes grown on Si and STO substrates under electric fields $\sim$ 0.5 MV/m. The MTE was measured to be $\sim$ 30 meV at photon energies equal to the work function of the Cs_3Sb cathodes. Within the limit of instrumental error, the experimentally measured value of MTE thus, nearly converges to the thermal limit of $k_B T$, which is 25 meV at room temperature.

At a photon energy of 1.75 eV, which was earlier reported to be the photoemission threshold, the MTE is measured to be $\sim$ 40 meV which is consistent with previously reported data [Cultrera *et al.* (2015)]. Based on the results that we have obtained, we claim that the higher than $k_B T$ values of MTE are not due to surface non-uniformities and

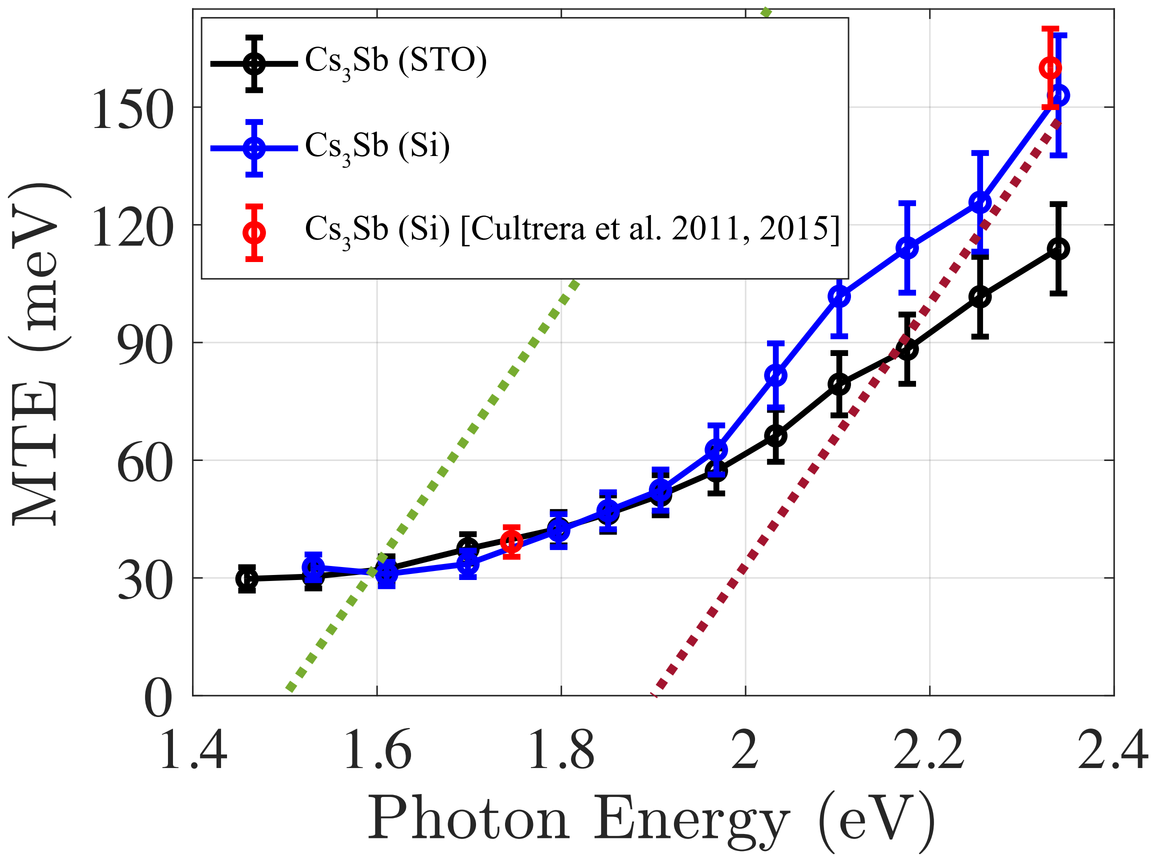

Figure 4.2: Spectral response of MTE measured from Cs_3Sb films grown on Si and doped STO substrates. The MTE approaches k_BT at the threshold. At higher photon energies, MTE does not scale as one-third of the excess energy owing to the scattering losses, which the electrons suffer before emission. The red dots show measurements of MTE from Cs_3Sb (Si) reported by previous authors. The dotted line is the plot for (excess energy)/3 considering $\Phi = 1.5$ eV (green) and $\Phi = 1.9$ eV (brown). Our results are in perfect agreement with previous results. The experimental MTE data marked by red red dots have been reproduced with permission from Cultrera *et al.* (2011), App. Phys. Lett. 99, 152110 (2011) [Copyright 2011 AIP Publishing LLC.] and Cultrera *et al.* (2015), Phys. Rev. Spec. Top. Accel. Beams. 18, 113401 (2015) [Copyright 2015 Author(s), licensed under a Creative Commons Attribution (CC BY) license].

defect density of states, it is a consequence of excess energy.

At photon energies away from the photoemission threshold, it can be seen in Figure 4.2 that the MTE does not scale as one-third of the excess energies. This can be explained by the scattering losses which the electrons suffer with different charge carriers and defects during transport to the surface before getting emitted. Also, at higher photon energies the Cs_3Sb film grown on the STO substrate exhibits a lower value for MTE than the corresponding cathode grown on the Si substrate. Previous studies have shown that the growth on these two substrates leads to very different surfaces in terms of roughness [Saha *et al.* (2022)]. The roughness will have a maximum impact on the MTE close to the threshold. In our measurements, we see that the near-threshold MTE is the same whereas the away-from-threshold MTEs differ. Hence, the difference in MTEs cannot be attributed to roughness. It is possible that the two films have a very different grain/defect structure, which can potentially result in higher scattering and therefore, larger electron energy losses in the film grown on the STO substrates as compared to films grown on Si.

Furthermore, the scattering as evidenced by the deviation of the MTE values from the (excess energy)/3 curve, is reflected in the PEES data. The top *x*-axis in Figure 4.1 shows the sum of the kinetic energy (E_k) of the emitted electrons and the work function (Φ) of the photocathodes. The sum of the maximum kinetic energy of the emitted electrons and the work function approximately equals the photon energy. If electrons do not scatter before emission or if the scattered electrons lose enough energy to not get emitted, like in the case of metallic photocathodes, the maximum in the energy distribution curves corresponds to the Fermi edge drop. This fermi edge drop occurs at nearly the photon energy on the kinetic energy (E_k) + work function (Φ) axis [Sun *et al.* (2011)]. In Figure 4.1, we can see that the sum of the work function and the kinetic energy corresponding to the maximum of the energy distribution curves does not coincide with that of the photon energy. This indicates that the electrons are scattered during transport, before being emitted from the Cs_3Sb

cathodes. A similar electron scattering mechanism is observed for other semiconductor photocathodes [Sun *et al.* (2011); Kachwala *et al.* (2022b)].

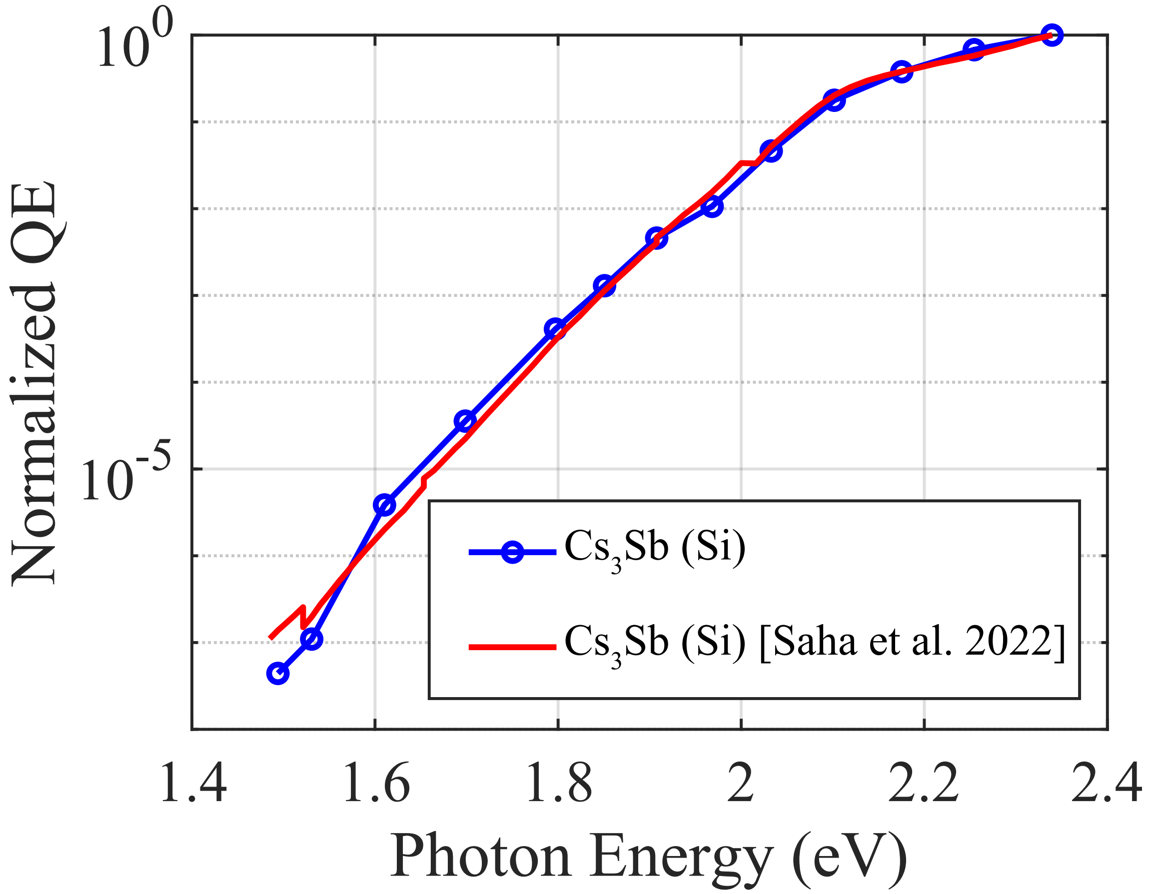

Figure 4.3: Comparison of the spectral response of QE from Cs_3Sb cathodes on Si, measured using PEEM and compared to cathode reported in Ref. 15. The QE is normalized to the maximum QE obtained from the Cs_3Sb cathode in green. The experimental QE data corresponding to the red curve has been reproduced from Saha *et al.* (2022), Appl. Phys. Lett. 120, 194102 (2022). Copyright 2022 AIP Publishing LLC.

Lastly, the spectral response of QE was measured with PEEM from the Cs_3Sb cathode on the Si substrate and compared with previously reported data in Figure 4.3.

At the photoemission threshold of 1.5 eV (as concluded from our PEES measurements), the QE measured is of the order of 10^{-7}, making it impractical to operate Cs_3Sb cathodes at the threshold for large charge density applications, without encountering non-linear photoemission effects. v

A knee-like feature is also observed in the QE spectral response at ~ 2.1 eV. This feature in the QE spectral response of Cs_3Sb cathodes has been previously reported in several works [Cultrera *et al.* (2011, 2015); Saha *et al.* (2022)] and had been attributed to the work function [Spicer (1958)]. However, our PEES measurements show that the actual work function is 1.5 eV. This implies that the knee-like feature in the QE spectral response does not correspond to the work function, but instead, could be an effect of band-bending close to the surface or could be caused by another feature in the electronic structure of the Cs_3Sb.

Given the polycrystalline nature of the Cs_3Sb films, it is extremely non-trivial to interpret the effects of band-bending, if any. The electronic structure of Cs_3Sb is also non-trivial. A recent study based on ab-initio calculations has shown that Cs_3Sb is thermodynamically unstable in its $D0_3$ cubic structure [Nangoi *et al.* (2022)], and a distorted superlattice is required for Cs_3Sb to exist in the stable form. This distorted superlattice structure exhibits an electronic structure that has a conduction band with a very small density of states close to the band-gap of ~ 1.18 eV [Nangoi *et al.* (2022)]. The knee-like feature could correspond to the point at which the density of states in the conduction band increases significantly. Determining the exact cause of the knee-like feature in the QE spectral response will require further investigation into the band structure and optical properties of Cs_3Sb cathodes. The use of detailed Monte Carlo simulations will be essential to model the scattering effects during transport and fully explain the measured photoemission properties.

Cs_3Sb is composed of only two elements. This makes its growth process significantly easier compared to other alkali-antimonides. However, due to the unstable nature of Cs_3Sb in the $D0_3$ form, it is much more complex in terms of lattice and electronic structure compared to other high QE alkali-antimonides like K_2CsSb and Na_2KSb. Consequently, their near-threshold photoemission properties could significantly differ from those of

Cs_3Sb and warrant exploration. Furthermore, the photoemission and optical properties of single crystalline Cs_3Sb [Parzyck *et al.* (2022a)] could also be very different from the polycrystalline films measured here and warrant further exploration.

4.5 Conclusion

In conclusion, we measured PEES, MTE and QE of Cs_3Sb photocathodes in the photon energy range of 1.45-2.33 eV. The PEES indicate that the work function of the Cs_3Sb cathodes is 1.5 ± 0.1 eV, significantly lower than the ~ 2.1 eV value that was previously reported based on the QE spectral response. The value of MTE at this work function of 1.5 eV was observed to be $\sim$ 30 meV - very close to the 25 meV at 300 K within instrumental error. Despite the low MTE, it might not be feasible to operate these cathodes at this photon energy given their low QE of the order of 10^{-7} (comparable to metal cathodes). As a result, the cathodes may need to be operated at photon energies away from the threshold, which would lead to higher MTE as a consequence of higher excess energy. Epitaxial, single-crystalline Cs_3Sb cathodes and other alkali-antimonides may, however, exhibit different photoemission features when operated at the threshold. It would be worthwhile to pursue photoemission studies of these cathodes to pave the way for brighter electron beams.

Chapter 5

ULTRAFAST LASER TRIGGERED ELECTRON EMISSION FROM THE ULTRANANOCRYSTALLINE DIAMOND PYRAMID TIP CATHODE

This chapter was published in Ref. [Kachwala *et al.* (2024)]

5.1 Abstract

Nitrogen-incorporated ultrananocrystalline diamond [(N)UNCD] pyramid tip cathode has been considered as a next generation high peak current electron source for dielectric laser accelerators as well as other high peak current particle accelerator applications. In this work we study non-linear photoemission from (N)UNCD pyramid tip cathode using an ultrafast laser with the pulse length of 150 femtoseconds with the central wavelength of 800 nm in the peak intensity range of $10^9 - 10^{10}$ W/cm^2. We demonstrated that as the incident laser intensity increases, the current emitted from the nano-tip first increases as a power function with an exponent of about 5, then starts to roll over to an exponent of 3. This roll over is attributed to the Coulomb interaction between electrons emitted from the tip also known as the space charge. We also measured the photoemission electron energy spectra which shows electrons with energies as high as $\sim$10 eV. Based on the shape of the electron energy spectra we conclude that the high energy electrons are thermally emitted electrons due to ultrafast laser heating at the tip of the (N)UNCD pyramid tip cathode.

5.2 Introduction

The widespread use of particle accelerators for basic research [Amaldi (2000)], ultrafast electron diffraction and microscopy [Kim *et al.* (2020b)] as well as medicine [Silari (2011)] calls for the need to develop compact accelerators with table top dimensions. A novel approach for downsizing particle accelerators and achieving higher acceleration gradient involves utilizing the interaction between charged particles and laser fields. Several techniques fall under this category, including laser-wakefield acceleration [Sprangle *et al.* (1988); Amiranoff *et al.* (1998); Tajima *et al.* (2020)], direct laser acceleration through the longitudinal component of radially focused laser light [Graves *et al.* (2017)], and dielectric laser acceleration (DLA) [England *et al.* (2014); McNeur *et al.* (2018)]. Dielectric and semiconductor materials have damage thresholds that correspond to acceleration fields in the range of 1 to 10 GV/m [Breuer and Hommelhoff (2013); Andonian (2012)], significantly higher than those in conventional metallic cavity-based accelerators [Holzer (2017)]. DLAs are microstructures made of dielectric materials powered by lasers with wavelengths between 800 nm and 2 microns [Simakov *et al.* (2017); England *et al.* (2022)]. Recent experiments have demonstrated the acceleration of relativistic electrons using dielectric grating microstructures, achieving accelerating gradients of 690 MV/m, which is ten times greater than traditional metallic cavity-based accelerators [Wootton *et al.* (2016)]. It is believed that the DLA can achieve the accelerating gradient of as high as $\sim$1 GV/m, which would enable the development of next generation compact accelerators.

A critical element of any particle accelerator, including the DLA, is the electron source known as the cathode. Due to the compact nature of DLA's transverse structure, typically ranging a few micrometers, there is a demand for exceptionally small, high-current density electron sources that can be triggered by a laser. This laser triggered photoemission simplifies the challenges associated with synchronizing the electron beam and the acceleration system. In addition, a DLA also requires a source with low emittance (sub 100 nm-rad), guaranteeing small divergence of the beam along the path of acceleration [Simakov *et al.* (2017)].

Ultrananocrystalline diamond (UNCD) is a promising candidate for such applications because of its mechanical and electrical stability along with an intrinsically fast response time ($\sim$100 fs) [Liu *et al.* (2014); Schneider (2022)]. Moreover, its vacuum robustness makes it a promising candidate for DLA and other high peak current accelerator applications. To improve the photoemission performance of UNCD and thereby extract more current, negative electron affinity (NEA) of the diamond can be exploited. A way to do so would be by *n*-doping of the UNCD and surface treatment in a hydrogen environment [van der Weide *et al.* (1994)]. Recently, *n*-doping of micro, nano and ultrananocrystalline diamond films using nitrogen has been performed by many groups [Pinault *et al.* (2007); Mengui *et al.* (2015); Shen and Chen (2007)]. In UNCDs, the nitrogen predominantly enters the grain boundaries and does not form trapped states within the diamond gap. It has been shown that the addition of nitrogen to UNCD films increases its electrical conductivity upto 1854 S cm^{-1} and the maximum current density to 8 mA cm^{-2} [Yuan *et al.* (2016)]. This is advantageous for DLA as well as other high peak current accelerator applications. Such films with nitrogen incorporation are termed as nitrogen-incorporated ultrananocrystalline diamond (N)UNCD.

Another advantage of (N)UNCD is that it can be molded into a pre-defined shape, even at nano-scale. To meet the transverse dimension, current density and emittance requirements of DLA, (N)UNCD can be molded into micron-scale diamond pyramid with sharp tip at the apex [Kim *et al.* (2018)]. These (N)UNCD pyramid tip cathodes (PTCs) can be triggered by a laser to simplify the issues of synchronization of the electron beam and the accelerating structure. When used in non-linear photoemission regime with infra-red light, the sharp tip at the apex can enhance the optical electric field of the incident laser thereby resulting in nanometer scale emission area and hence achieve sub-micron scale normalized transverse emittance. These photoemission properties make the (N)UNCD PTC a promising candidate for DLA applications. In addition, the (N)UNCD PTC can also be used for electron microscopy, nano-electronics as well as high peak current accelerator applications.

The field emission studies of (N)UNCD PTC have been performed by many groups [Kim *et al.* (2020a); Huang *et al.* (2019b,a); Nichols *et al.* (2020); Andrews *et al.* (2020); Chubenko *et al.* (2019)]. In the field emission mode, using (N)UNCD PTC, the maximum single tip current measured was as high as 18 μA [Jarvis *et al.* (2010)]. Further, (N)UNCD PTC have demonstrated an effective emission area of 400 nm^2 with an average emission current as high as 2 μA [Nichols *et al.* (2020)]. However, in order to have sub-picosecond electron bunch lengths required for DLA as well as other particle accelerator applications, the (N)UNCD PTC need to be operated in the photoemission regime. The linear photoemission mechanism, where the operating photon energy is higher than or at the work-function of the (N)UNCD, as well as (N)UNCD PTC is very well understood and performed by many groups [Chen *et al.* (2019); Pérez Quintero *et al.* (2014); Chen *et al.* (2020); Kachwala *et al.* (2022b); Simakov *et al.* (2019)].

In order to have a nanometer scale emission area from (N)UNCD PTC, they need to be operated in the non-linear photoemission regime. Operating in non-linear photoemission regime results in the optical field enhancement at the tip of (N)UNCD PTC and thereby result in electron emission only from the nanometer scale tip of the cathode. Non-linear photoemission studies from (N)UNCD PTC using infrared wavelengths have been performed by two groups [Pavlenko *et al.* (2019); Simakov *et al.* (2019)]. Both of them observe the characteristic change in non-linearity in electron count with increasing laser intensity. However, the mechanism responsible for this change in non-linearity is not very well understood. In certain studies, the non-linear photoemission measurements were done for (N)UNCD PTC at different infrared wavelengths ranging from 800 nm to 2000 nm with peak laser intensities in the range of $10^9 - 10^{10}$ W/cm^2 [Pavlenko *et al.* (2019); Simakov *et al.* (2019)]. At each of these wavelengths a characteristic change in non-linearity in electron count rate with increasing laser intensity was observed. They also observed increase in electron emission spot size at high laser intensities. As a result, the change in non-linearity was attributed to Coulomb interaction between electrons emitted from the (N)UNCD PTC or the space charge. In another study, the change in non-linearity was attributed to the strong field photoemission from (N)UNCD PTC [Pavlenko *et al.* (2021)]. In strong field photoemission, the emitted electron can re-scatter with the parent photocathode under the influence of electric field of the laser. These re-scattered electrons can have trajectories that can result in increase in the electron emission spot size. However, none of these studies measured the kinetic energy distribution of the emitted electrons which would explain the change in non-linearity and thereby aid in understanding of emission mechanism from (N)UNCD PTC.

In this work, we report the measurements of scaling of the electron count rate with incident laser intensity and the photoemission electron energy spectra (PEES) in the non-linear photoemission regime from (N)UNCD PTC using photoemission electron microscope (PEEM). The change in non-linearity was observed with increasing laser intensity which was consistent with the previously reported data. However, at low intensity regime, we observe 5^{th} order photoemission process as opposed to $8^{th} - 12^{th}$ order observed for previous works. We attribute this 5^{th} order photoemission process to above-threshold photoemission (ATP) which is regularly observed for needle tip photocathodes or to the emission from direct band gap of diamond. At high laser intensities, we observe the *kink* resulting in the change in non-linearity from 5 to 3. We also observe increase in electron emission spot size beyond the *kink*. To further understand the emission mechanism, we measured the PEES which shows electron with energies as high as $\sim$10 eV. Based on the shape of the PEES we conclude that the high energy electrons are not emitted due to strong field photoemission but instead are thermally emitted electrons due to laser heating at the tip of (N)UNCD PTC and the increase in spot size is attributed to the Coulomb interaction between electrons emitted from the (N)UNCD PTC.

5.3 Experimental Details

5.3.1 Sample Preparation

The diamond deposition process for synthesis of (N)UNCD films was performed by Advanced Diamond Technologies. Details of different steps for the preparation of (N)UNCD are reported elsewhere [Kim *et al.* (2018)]. Typically, it has 1 μm layer of conductive (N)UNCD film, followed by a layer of 15 μm microcrystalline diamond. Diamond film is brazed to a polished Mo substrate using the brazing material TiCuSil.

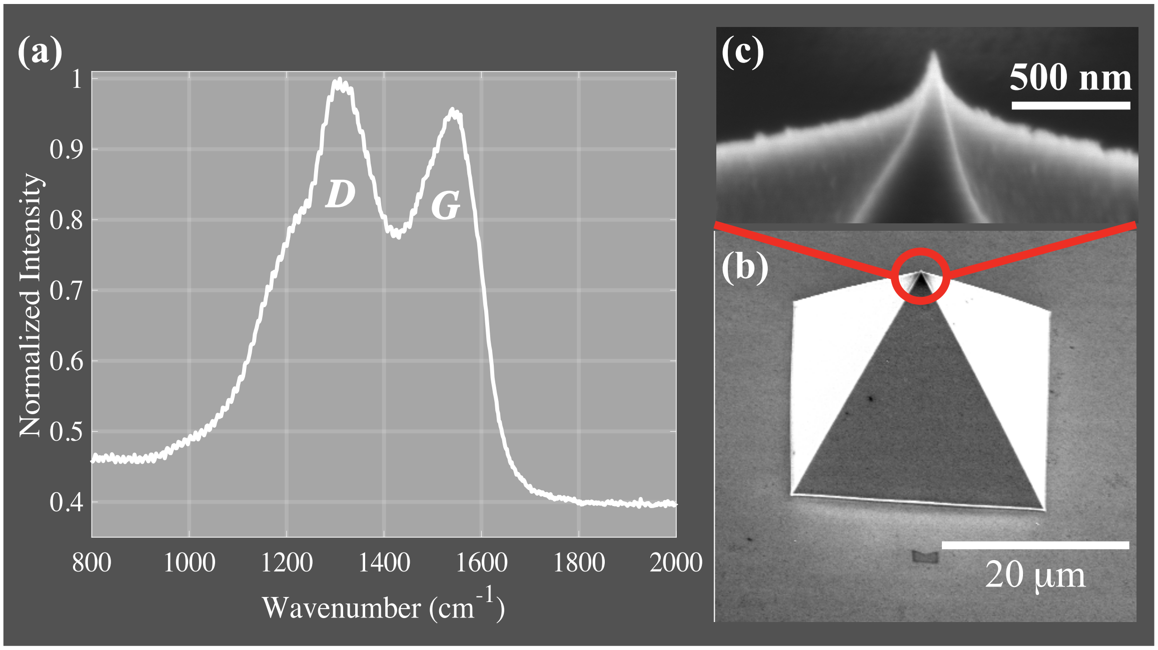

Figure 5.1: (a) Raman spectrum of the (N)UNCD sample showing a characteristic disordered diamond (D) peak and graphite (G) peak. Scanning Electron Microscope (SEM) image of (b) (N)UNCD PTC and (c) sharp tip with radius ~15 nm at the apex of (N)UNCD PTC.

Figure 5.1(a) shows the Raman spectrum of an (N)UNCD sample. The broad peaks at 1350 cm^{-1} and 1550 cm^{-1} correspond to the characteristic disordered diamond (D) peak and graphite (G) peak respectively. Figure 5.1(b) and (c) shows the scanning electron microscope image (SEM) of (N)UNCD PTC. As shown in the figure 5.1(b), the pyramid has a base of ~25 μm with the aspect ratio of 0.7. Figure 5.1(c) shows a sharp emitter tip at the apex of the pyramid. The radius of the tip was ~15 *nm*.

5.3.2 Measurement Details

The schematic of experimental set up is shown in Fig.5.2. The measurements were performed using a 500 kHz repetition rate femtosecond pulsed laser with a pulse length of 150 fs from a pulsed Optical Parametric Amplifier (Light Conversion Orpheus pumped by Light Conversion Pharos) and central wavelength of 800 nm. The laser was made incident onto the sample at 65° angle of incidence with respect to the axis of the (N)UNCD PTC and was focussed by a lens down to the spot size of 80 μm × 150 μm. The polarization of the electric field was as shown in Fig.5.2 and all the measurements were performed in this mode (p-polarized on the sample) of laser polarization. One millimeter real space field of view (significantly larger than the laser spot size) was selected to image all the photoemitted electrons using a double micro channel plate (MCP) detector at the end of a commercially available PEEM column from Focus gmbh [Foc (2024)]. The number of electrons emitted from the tip was determined by recording counts/second on the MCP detector and using a predetermined calibration factor to convert it into electrons per shot at different values of incident laser intensities.

The photoemission spectra were obtained by using the imaging energy filter (IEF) capability of the PEEM. Background subtracted energy filtered images were obtained for the (N)UNCD PTC sample with ~100 meV energy resolution. The contrast aperture (CA) of a 1750 μm diameter placed in the backfocal plane of the objective lens in the PEEM column was selected to ensure transmission of all the emitted electrons from the surface of the sample. After acquiring the energy filtered images, a numerical differentiation of high pass energy spectrum was performed and the normalized counts were plotted against the kinetic energy of emitted electrons for different incident laser intensities. A detailed description of the measurement procedure can be found in Ref. [Kachwala *et al.* (2022b)].

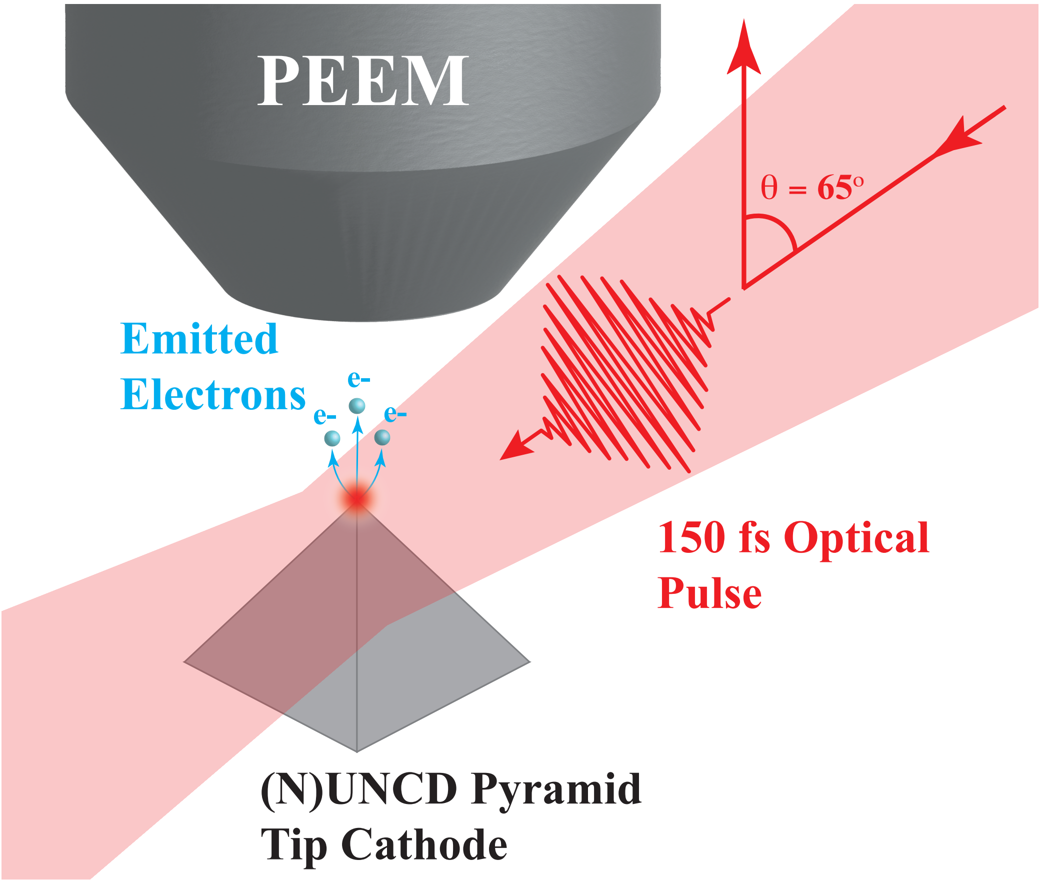

Figure 5.2: Schematic of experimental set up showing (N)UNCD PTC illuminated by femtosecond laser with the pulse length of 150 fs and central wavelength of 800 nm. The laser was was made incident onto the sample at 65° with respect to the axis of (N)UNCD PTC. The sharp tip at the apex of (N)UNCD PTC results in field enhancement of the incident laser field. The electron emitted from the sharp tip at the apex of (N)UNCD pyramid are imaged using photoemisison electron microscope (PEEM).

An electric field bias of 5 kV/m was applied between the cathode and the extractor of the PEEM. The bias was low enough so that there was no observed dark current in absence of the incident laser. Reliable spatial and *k*-space images could not be obtained due to the pyramids distorting the accelerating fields in the PEEM.

5.4 Results and Discussion

Figure 5.3 shows the the results of our measurements of the number of electrons emitted per shot from the (N)UNCD PTC plotted as a function of peak laser intensity on a double logarithmic scale. For the same value of peak laser intensity, the number of electrons emitted per shot from the (N)UNCD PTC was an order of magnitude higher than the corresponding emission from the (N)UNCD flat substrate [Kachwala *et al.* (2022b)]. This indicates that the enhancement of optical field is taking place at the tip of the (N)UNCD PTC and that results in more electrons being emitted per shot for the same range of peak laser intensity when compared to the (N)UNCD substrate. Considering the work function

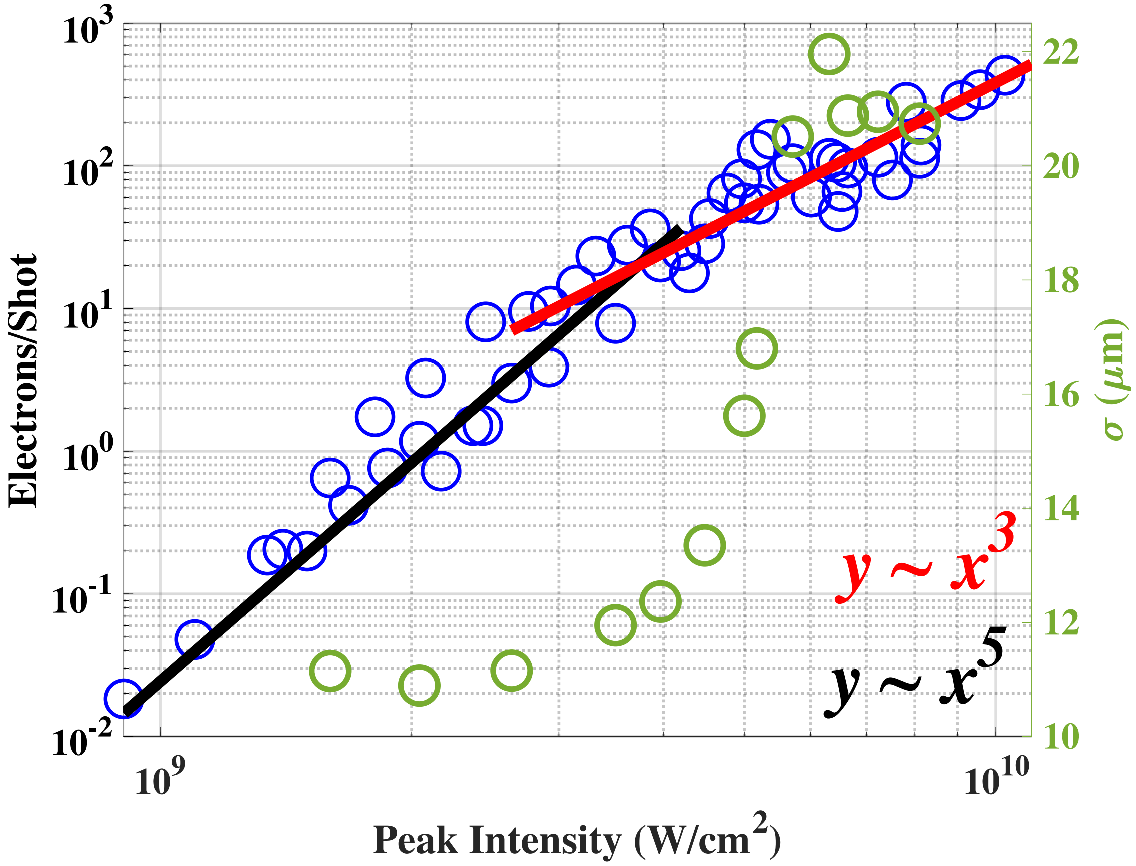

Figure 5.3: Logarithmic representation of electrons per shot (in blue) emitted from (N)UNCD PTC as the function of peak laser intensity. Semi-logarithmic representation of evolution of root mean square spot size (in green) of electrons detected on the micro-channel plate detector of the PEEM plotted as a function of peak laser intensity.

(Φ) of (N)UNCD to be ~4.4 eV [Kachwala *et al.* (2022b)], using 1.55 eV photon energy should result in 3^{rd} order photoemission. However, for the case of (N)UNCD PTC, at the peak intensities less than ~4 GW/cm^2, the exponent of the peak intensity dependence suggests a 5^{th} order photoemission process. The 5^{th} order of non-linearity which is quite different from the 8^{th} – 12^{th} orders observed in previous studies [Pavlenko *et al.* (2019); Simakov *et al.* (2019)] could be due to the different curvature of the (N) UNCD PTC as well as different doping concentration.Other than the tip shape and doping the angle of incidence and the polarization of the laser may also play a role. Previous studies have reported the angle of incidence to be 84° whereas we have a 65° angle of incidence. The angle of incidence could also make a difference in the order of emission from (N)UNCD PTC. In general, the lowest multiphoton order n_{min} dominates the photoemission rate in the multiphoton regime. However, at higher value of laser intensity there is a substantial contributions from higher multiphoton orders $n > n_{min}$. This emission mechanism is called above-threshold photoemission (ATP) [Reutzel *et al.* (2020); Krüger (2013)]. The 5^{th} order photoemission process could be a result of ATP. The 5^{th} order photoemission process could also be a result of electron emission from the direct band gap of diamond [Giustino *et al.* (2010)]. Electrons can be excited into the conduction band across the direct bandgap (7.1 eV [Giustino *et al.* (2010)]) of diamond. These electrons can migrate to the surface and emit into the vacuum. Using 1.55 eV photon energy, 5^{th} order photoemission process would correspond to $\sim$ 7.7 eV of photon energy being absorbed by the electrons which is above the photoemission threshold of emission from the direct band gap of diamond. A similar higher order photoemission mechanism has been observed from nanocrystalline diamond coated tungsten tips and was attributed to the electron emission from the direct band gap of diamond [Tafel *et al.* (2019)].

At $\sim$4 GW/cm^2, a soft *kink* followed by a change of slope in electrons per shot vs peak laser intensity plot is observed. This *kink* results in the change in non-linearity from 5 to 3. The transition from multiphoton electron emission to strong field photoemission is marked by a similar characteristic change in nonlinearity [Krüger (2013)]. The change of slope could also occur due to the Coulomb interaction between electrons emitted from the photocathode and screening of the electric field by the electron cloud also known as space charge or due to filling of the excited states prohibiting excitation.

To further elucidate this change in non-linearity, we measured the electron emission spot size measured on the MCP detector at the end of the PEEM column as the function of peak laser intensity. This root mean square electron emission spot size as a function of peak laser intensity is shown on a semi-log plot in Fig. 5.3. We can see that with increase in peak laser intensity, the electron emission spot size increases. A similar behaviour was also observed in Ref. [Pavlenko *et al.* (2019)]. Owing to this observation, at first glance it appears that the change in non-linearity is due to the Coulomb interaction between electrons emitted from the photocathode and screening of the electric field by the electron cloud. However, in strong field photoemission, the re-scattered electrons can have trajectories that can result in increase in the electron emission spot size.

One way to understand if the electron emission is due to strong field photoemission is by measuring the kinetic energy spectra of the emitted electrons. For the case of strong field emission, the local laser electric field steers the motion of a photoemitted electron and can cause the electron to return to the parent photocathode. The photoelectron then eventually scatters with the parent photocathode and recollision takes place. This is clearly observed in the electron kinetic energy spectra. The low kinetic energy spectrum is dominated by the direct electrons where the emitted electrons do not return back to the parent photocathode under the influence of strong laser field. This low energy part of the spectrum shows strong exponential decay of the electron count rate with increasing kinetic energy. At higher kinetic energy, the electron count rate doesn't change with the increasing kinetic energy and a plateau is observed in the electron kinetic energy spectra. The extent of this plateau region on the kinetic energy scale increases with increase in laser intensity. For the case of tungsten metal tip, with the radius of about 8 nm, this plateau region is observed in the electron kinetic energy range of 5-12 eV for the peak intensity range of 0.55×10^{11} W/cm^2

to 1.3×10^{11} W/cm^2 [Krüger (2013)]. At even higher kinetic energies, the count rate again drops dramatically. The energy position where this strong decay starts is called cut-off. Plateau and cut-off are formed by re-scattered electrons. If there is a strong field emission from (N)UNCD PTC, we should see the evidence of direct and rescattered electrons in the kinetic energy spectra.

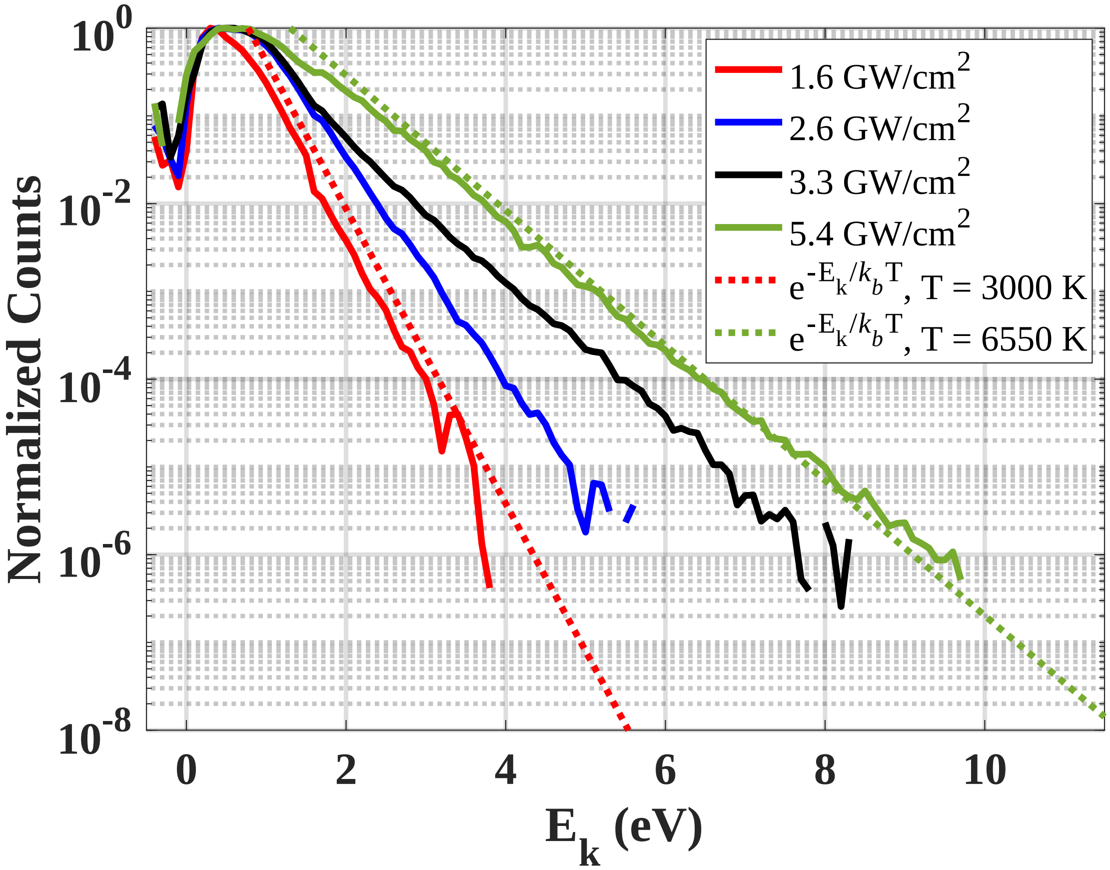

Figure 5.4: Photoemission electron energy spectra (PEES) at different incident peak laser intensities. The solid lines are the PEES spectra from (N)UNCD PTC. The dotted line is the plot of e^{-E_k/k_bT} with T = 3000 K (red) and T = 6550 K (green). The plot of e^{-E_k/k_bT} was shifted by a constant factor to align with the experimental energy spectrum.

Figure 5.4 shows the semi-logarithmic plot of the normalized electron count rate plotted against the kinetic energy of the emitted electrons. From the Fig. 5.4 we see that the kinetic energy spectrum broadens with increasing peak laser intensity. For the case of the 5^{th} order multiphoton emission process from (N)UNCD PTC, the maximum kinetic energy that the electrons can have is (5×1.55 eV) - $\Phi = 3.4$ eV, where $\Phi = 4.4$ eV. Even if we consider the electron emission from the direct bandgap of diamond (7.1 eV [Giustino *et al.* (2010)]), the kinetic energy spread of the emitted electrons should be ∼0.6 eV. However, we see electrons with energies as high as ∼10 eV. In the kinetic energy spectra we do not observe any plateau or cut-off which appears due to re-scattered electrons which is the characteristic feature of any strong field photoemission process.

The strong field photoemission regime is characterized using Keldysh theory [**?** and is characterized in terms of the Keldysh parameter γ which is given by the following equation.

$$\gamma = \sqrt{\frac{\Phi}{2U_p}}, \tag{5.1}$$

where Φ is the work function and the ponderomotive energy U_p is given by the following equation:

$$U_p = \frac{e^2\alpha^2{E_0}^2}{4m\omega^2}, \tag{5.2}$$

where e is the electron charge, m is the mass of the electron, α is the field enhancement factor, E_0 is the field strength and ω the angular frequency of the incident light. The strong field photoemission regime is governed by $\gamma << 1$.

To get the estimate of field enhancement at the (N)UNCD PTC, we performed a lumerical FDTD simulation [Lum (2024)]. The geometry of the tip was similar to the (N)UNCD tip used for experiment with the tip radius of 15 nm. A gaussian pulse with pulse length of 150 fs and central wavelength of 800 nm was made incident at an angle of 65° with respect to the axis of the (N)UNCD PTC. The refractive index parameters were taken from Ref. [Ficek *et al.* (2016)].

Figure 5.5 shows field enhancement factor $\alpha \approx 3$ (which is typical for semiconductor tip of the dimensions similar to (N)UNCD PTC in this study [Kealhofer *et al.* (2012)]), and for maximum peak laser intensity of 5.4 GW/cm^2 would result in ponderomotive energy of ∼0.3 μeV. Taking $\Phi = 4.4$ eV, this would result in $\gamma \sim 3900$ which is nearly 4 orders of magnitude higher than the value of γ where strong field photoemission is expected to be observed.

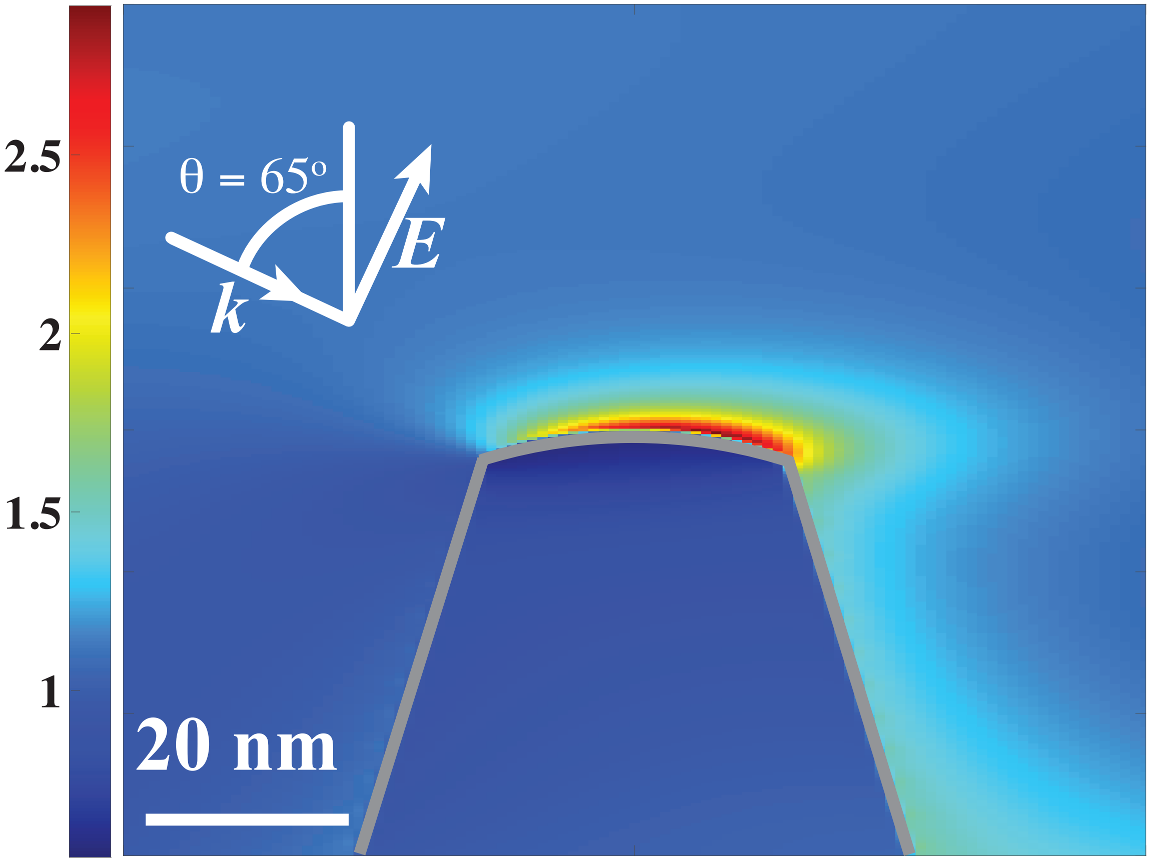

Figure 5.5: Time-average of the optical electric field in vicinity of a sharp (N)UNCD PTC calculated using lumerical FDTD method. The color encodes the ratio of the local field average and the amplitude of the incident light. The field is enhanced at the surface of the apex by a factor of up to ~3.

When operating photocathodes with ultrafast (~100 fs) laser pulses and very large laser intensities (~ GW/cm^2), the temperature of electronic distribution is effectively isolated from the lattice and as a result can increase to several thousands of Kelvin [Elsayed-Ali *et al.* (1987); Fann *et al.* (1992)]. This is in part due to large difference in electron and lattice heat capacities. These laser excited electrons scatter with other non-excited electrons repeatedly, eventually transferring all the laser energy into the thermal energy of electrons, thus heating them. This occurs at sub to few pico-second time scales. As a result, the thermalized electron emission occurs which is not prompt and long tails of high energy electrons are present in the kinetic energy spectra of emitted electrons. Such long tails of high energy energy electrons are present in the kinetic energy spectra shown in Fig.5.4. Such thermalized electron emission has also been reported previously for carbon nanotube based nanotip [Bionta *et al.* (2015)] as well as silver nanotip when operated with high repetition rate laser [Bionta *et al.* (2016)]. For laser intensity of 1.6 GW/cm^2 and 5.4 GW/cm^2, electron temperature as high as 3000 K and 6550 is reached respectively. Such high electron temperatures in photoemission have also been reported previously from copper [**?**, silver nanotips [Bionta *et al.* (2016)], tungsten and carbon nano-tube based nanotip [**?**.

After this initial rise in electron temperature, the equilibrium between electron and lattice is reached via electron-phonon scattering and can happen over pico-seconds to tens of pico-second timescale [Maxson *et al.* (2017)]. Diamond possesses the highest thermal conductivity of $\sim$2000 W/mK in all bulk materials (5 times the thermal conductivity of the best metals such as copper), owing to low phonon scattering in diamond [Che *et al.* (2000)]. Since phonon scattering is drastically enhanced by grain boundaries, the thermal conductivity of polycrystalline diamond films is strongly dependent on the grain size. The grain size of UNCD films is of the order of less that 10 nm [Tóth *et al.* (2018); Rani *et al.* (2018); Chubenko *et al.* (2019)]. As a result this significantly reduces the thermal conductivity of UNCD films. The thermal conductivity of UNCD films is reported to be $\sim$16 W/mK and decreases to $\sim$8 W/mK with the addition of nitrogen into the film [Shamsa *et al.* (2008)]. Such poor thermal conductivity can significantly heat up (N)UNCD PTC lattice during the equilibrium process between the electrons and lattice over pico-seconds to tens of pico-second timescale via electron-phonon scattering.

As a result, after thermalization of electron gas and lattice via electron-phonon and phonon-phonon scattering a steady-state lattice temperature is reached which can be

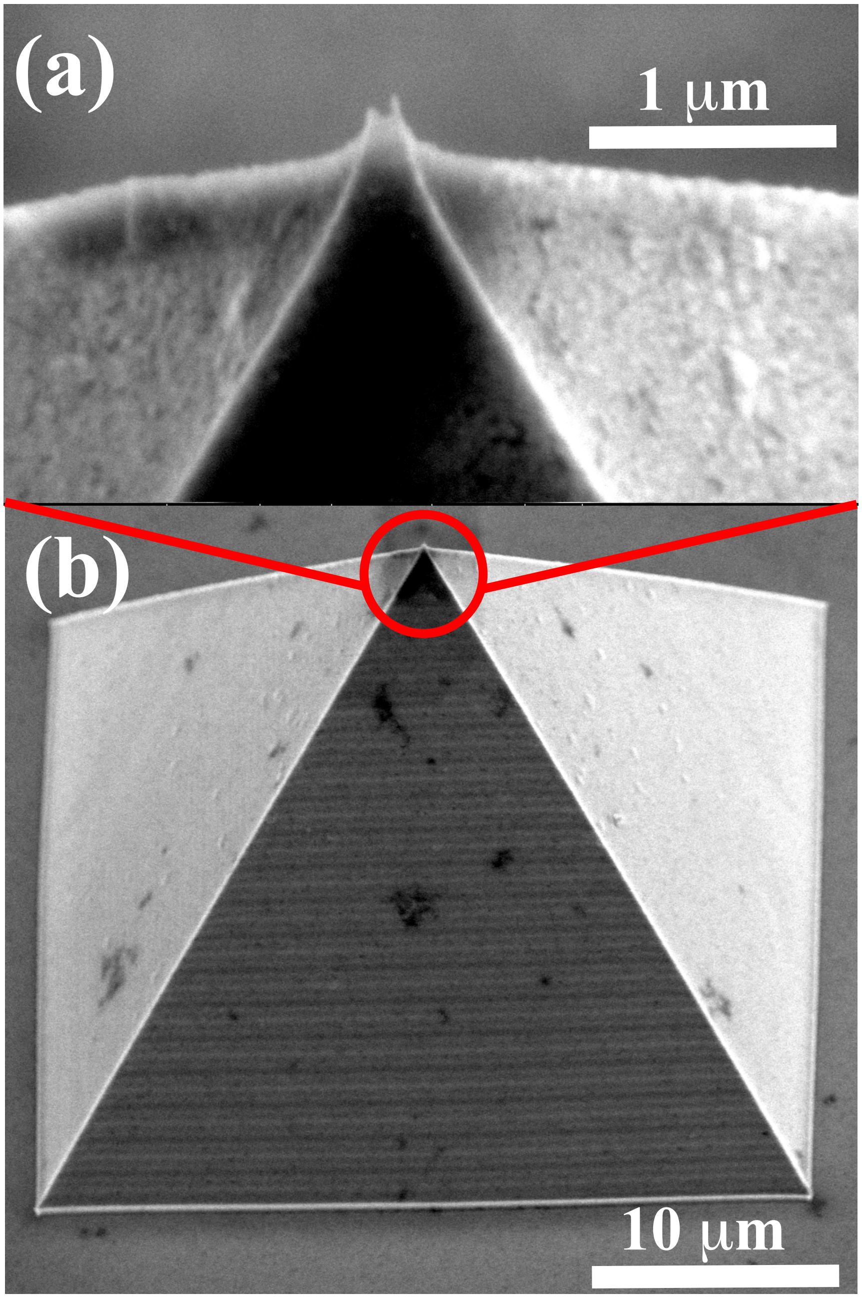

Figure 5.6: (a) Structural change in the tip at the apex of (N)UNCD PTC after irradiation with femtosecond laser with the pulse length of 150 fs and central wavelength of 800 nm (b) (N)UNCD PTC showing laser-induced periodic surface structures (LIPSS) on the pyramid face exposed to the incident laser. The LIPSS were oriented perpendicular to the direction of the electric field of the incident laser with spatial period of the order of ∼800 nm.

significantly higher than the room temperature. As a result, this can alter the shape of the tip of the (N)UNCD PTC due to heating process. Such a change is shape was clearly visible in the SEM of the tip performed after the photoemission experiments as shown in Fig.5.6 (a). The sharp protrusions on the tip can also be due to the carbon contamination present inside the SEM which cannot be discriminated from the diamond.

In addition, from Fig.5.6 (b),we see that the pyramid face where the laser was incident, shows coherent surface structuring after laser irradiation. Such coherent surface structuring was not present before laser irradiation. Such laser-induced periodic surface structures (LIPSS) have been reported on many materials including metals as well as semiconductors after ultrafast laser irradiation [Huang *et al.* (2022); Borowiec and Haugen (2003); Bonse *et al.* (2012)]. These LIPSS are oriented perpendicular to the direction of the electric field of the incident laser with spatial period of the order of wavelength of the incident radiation. LIPSS spaced on the order of wavelength and oriented perpendicular to the direction of the electric field of the incident laser were also observed for (N)UNCD PTC. Such LIPSS for (N)UNCD PTC have also been reported previously after irradiation with femtosecond laser [Simakov *et al.* (2019)].

5.5 Summary and Conclusion

We measured the scaling of the electron count rate with incident laser intensity and the PEES in the non-linear photoemission regime from (N)UNCD PTC. The measurements were performed with peak laser intensities in the rangde of $10^9 - 10^{10}$ W/cm^2. At low intensity regime, we observe 5^{th} order photoemission process. We attribute this 5^{th} order photoemission process to ATP or emssion from the direct band gap of diamond. At high laser intensities, we observe the *kink* resulting in the change in non-linearity from 5 to 3. We also observe increase in electron emission spot size beyond the *kink*. We attribute this increase in spot size to Coulomb interaction between electrons emitted from the (N)UNCD

PTC. We also measured the PEES which shows electron emitted with kinetic energies as high as $\sim$10 eV. Based on the shape of the PEES we conclude that the high energy electrons are not emitted due to strong field photoemission but instead are thermally emitted electrons due to laser heating at the tip of (N)UNCD PTC.

Chapter 6

ULTRACOHERENT ELECTRONS FROM NANOSTRUCTURED PLASMONIC SPIRAL PHOTOCATHODE

6.1 Abstract

In this work we demonstrate the generation of a record low root mean square normalized transverse electron emittance of less than 40 pm-rad from a photocathode – more than three orders of magnitude lower than the best the emittance that has been achieved before from a photocathode. This was achieved by using plasmonic focusing of light to a sub-diffraction regime using plasmonic Archimedean spiral structures resulting in a $\sim$50 nm root mean square electron emission spot. Such ultra-low emittance nanostructured electron sources exhibiting simultaneous spatio-temporal confinement to nanometer and femtosecond level can be used as an advanced electron source for the high repetition rate ultrafast electron diffraction and microscopy apparatus as well as next generation accelerator applications.

6.2 Introduction

High repetition rate ($>$100 kHz) sub-picosecond pulsed electron beams are critical to the studying of the ultrafast structural dynamics of atomic lattices as well as molecular species through techniques like stroboscopic ultrafast electron diffraction and microscopy (UED/M) [Sood *et al.* (2021); Siddiqui *et al.* (2023); Durham *et al.* (2020); Gliserin (2014); Ji *et al.* (2019); Ischenko *et al.* (1983, 1994); Kirchner (2013)]. Even though field emission tips can generate brighter electron beams resulting in sub-angstrom scale spatial resolutions in electron microscopes, they cannot be switched at sub-microsecond timescales, making femtosecond-laser triggered photoemission of electrons a preferred way of generating such sub-picosecond scale electron bunches [Siddiqui *et al.* (2023); Durham *et al.* (2020); Ji *et al.* (2019); Kirchner (2013)].

For UED/M applications, the normalized transverse emittance of the electron bunch determines the spatial resolution of the instrument [Musumeci *et al.* (2018); Li *et al.* (2022); Filippetto and Qian (2016)] and is expressed in terms of the following equation:

$$\varepsilon_{n,x} = \frac{\sqrt{\langle x^2 \rangle \langle p_x^2 \rangle - \langle x p_x \rangle^2}}{m_e c}, \tag{6.1}$$

where $\varepsilon_{n,x}$ is the normalized transverse emittance in the one of the two transverse directions (x), $\sqrt{\langle x^2 \rangle} \equiv \sigma_x$ is the root mean square (rms) electron spot size in the x-direction, $\sqrt{\langle p_x^2 \rangle} \equiv \sigma_{p_x}$ is the rms electron momentum spread in the x-direction, $\langle x p_x \rangle$ is the correlation term between the location of emission and the transverse momentum, m_e is the mass of an electron and c is the speed of light [Dowell and Schmerge (2009b)].

In addition to the smallest possible emittance UED/M instruments require a high enough current (or number of electrons per bunch) to achieve a good signal to noise ratio and collect data in a reasonable amount of time. Often pinholes can be used to collimate the electron beam to reduce the emittance at the cost of the current [Ji *et al.* (2019); Li *et al.* (2022); Feist *et al.* (2017); Siddiqui *et al.* (2023)].

The emittance and current (or electrons per bunch) can be combined into one figure of merit, the 4D-Brightness given by:

$$\mathrm{B}_{4\mathrm{D}} = \frac{Q}{\varepsilon_{n,rms}^2}, \tag{6.2}$$

where Q denotes the total bunch charge or number of electrons and $\varepsilon_{n,rms}$ is the geometric mean value of the emittance along the x-and y-directions [Li *et al.* (2022)].

Another important factor that often determines the temporal resolution of UED/M apparatus is the rms length of the emitted electron bunches (σ_t) [Filippetto *et al.* (2022);

Musumeci *et al.* (2018)]. To achieve the best temporal resolutions and mitigate the effects of electron-electron repulsion in a bunch, many UED/M setups rely on photoemisison from flat, large area (several mm scale) cathodes placed in an accelerating electric field in conjunction with radio frequency (RF) bunching cavities [Li *et al.* (2022); Chatelain *et al.* (2012)]. Such large area flat cathodes are also required for UED/M instruments based on RF guns used to obtain mega electron volt (MeV) scale energy electron bunches for reduced jitter owing to their relativistic speeds and larger signal in higher-order diffraction peaks due to the shorter electron wavelength [Siddiqui *et al.* (2023); Ji *et al.* (2019); Weathersby *et al.* (2015); Carter and Williams (2016)].

Electron beams from such flat cathodes have been collimated using pinholes [Li *et al.* (2022); Siddiqui *et al.* (2023); Ji *et al.* (2019)] to result in emittance of 120 pm-rad with a current of 100-200 fA ($\sim$1 electron/shot) and rms electron bunch length of $<$100 fs. Further improvements in emittance or brightness in such setups requires improvement of brightness at the cathode. For high repetition-rate UED/M experiments where only single to few electrons per bunch are enough, emittance can be reduced either by σ_x or σ_{p_x} or both. σ_{p_x} depends on the cathode materials, its surface and the laser fluence [Parzyck *et al.* (2022b); Galdi *et al.* (2021); Saha *et al.* (2022); Feng *et al.* (2017); Cultrera *et al.* (2016); Kachwala *et al.* (2023b); Saha *et al.* (2021); Knill *et al.* (2023c); Knill (2023); Soomary *et al.* (2021); Knill *et al.* (2023a); Karkare *et al.* (2014)]. σ_{p_x} as low as 50 eV$/c$ (which corresponds to the mean transverse energy of 5 meV) has been achieved by cryo-cooling of a copper photocathode with an atomically ordered surface and operating it at the photoemission threshold in the ultra-low charge regime [Karkare *et al.* (2020)]. σ_x is limited by the diffraction limit of light and the ability to focus the laser to a small spot size [Silfies *et al.* (2019); Musumeci *et al.* (2018)]. σ_x as small as 1 um has been achieved by operating the cathode in the transmission mode geometry and placing the final focusing lens very close $\sim$1 cm behind the cathode [Li *et al.* (2022, 2012); Wen-Xi *et al.* (2009)].

In this article we demonstrate an emission spot (σ_x) of 50 nm rms resulting in an emittance of less than 40 pm-rad - more than three orders of magnitude smaller compared to the best emittance of <50 nm-rad previously demonstrated from a photocathode [Li *et al.* (2012)]. The small emission area has been achieved using a combination of non-linear photoemission and focusing of light to sub-diffraction limited areas using plasmonic Archimedean spirals [Chen *et al.* (2010)]. This Archimedean spiral photocathode (ASP) uses circularly polarized light that excites the surface plasmon polaritons (SPP) along the groves of the spiral. These SPPs interfere constructively at the center of the spiral as shown in Fig. 6.1 resulting in a sub-diffraction limited spot [Guo *et al.* (2017); Gramotnev and Bozhevolnyi (2010); Tan *et al.* (2017)].

6.3 Finite Difference Time Domain Simulation

Figure 6.2 (a) shows the intensity enhancement due to constructive interference of the SPP's at the center of ASP calculated using finite difference time domain (FDTD) simulation using a commercial software suite (Lumerical) [Lum (2024)] (for details see Appendix B). The SPP focussed intensity (I_{spp}) has full width half maximum (FWHM) of ~260 nm. Considering 5^{th} order non-linearity in the electron emission process, the spatial extent of the electron emission spot will be propotional to I_{spp}^5 [Musumeci *et al.* (2010); Ferrini *et al.* (2009)]. This will further shrink the electron emission spot to ~120 nm FWHM or σ_x ~50 nm as shown in Fig. 6.2 (b).

6.4 Fabrication

The simulated ASP geometry was fabricated by electron-beam lithography (EBL) of double layered poly-methyl methacryalate (PMMA) on a silicon substrate followed by electron-beam evaporation of chromium and gold. The schematic of ASP fabrication is shown in Fig. 6.3 (a). Double-layered Poly methyl methacryalate (PMMA) (185 nm 495

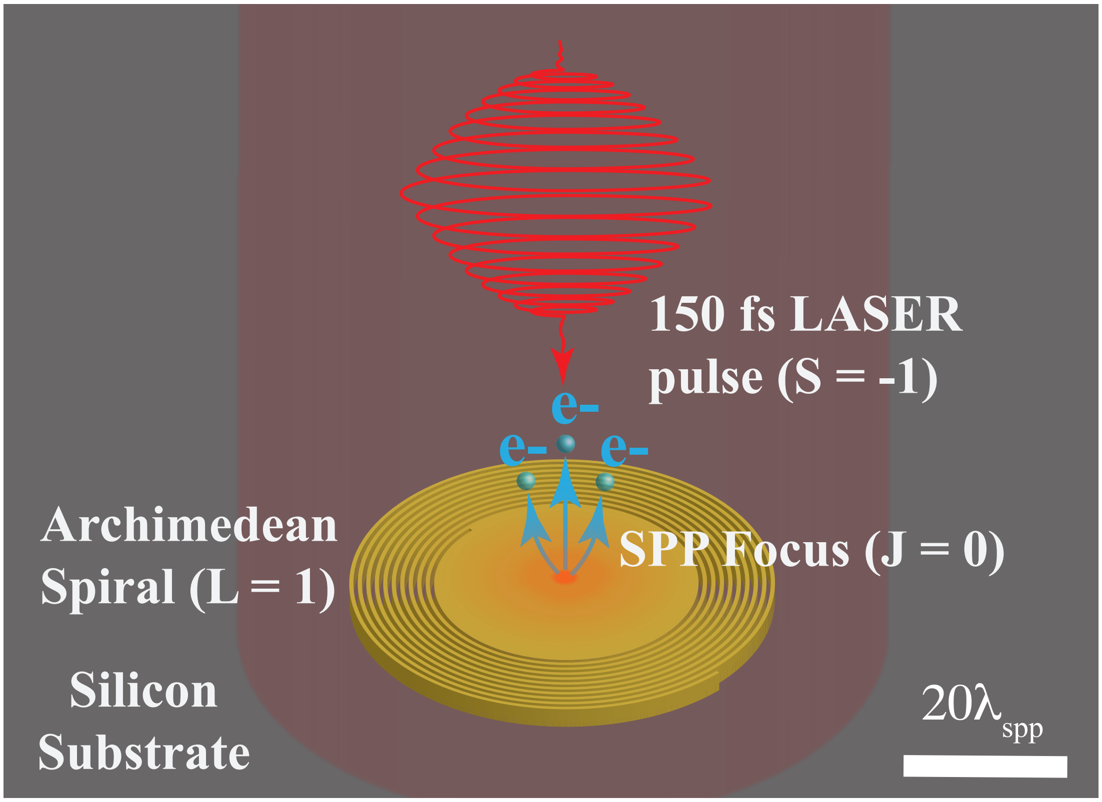

Figure 6.1: Schematic of gold Archimedean spiral photocathode with topological charge L = 1. This topological charge is compensated by illuminating it with a circularly polarized laser (S = -1) with a pulse length of 150 fs and central wavelength of 800 nm to yield an SPP pulse with vanishing orbital angular momentum J = L + S = 0. The laser was was made incident onto the sample at 4° with respect to the surface normal of gold Archimedean spiral photocathode. The plasmons generated interfere constructively at the center of the spiral resulting in the intensity enhancement. The electron emitted from the center of the spiral are imaged using photoemisison electron microscope (PEEM). Here $\lambda_{\text{spp}} = 783$ nm.

K + 200 nm 950 K) was spin-coated on a silicon (Si) substrate. Then the spiral patterns were written with EBL (JEOL JBX-6000FS). The samples were then developed in methy isobutyl ketone (MIBK) and iso-propyl alcohol (IPA) MIBK: IPA (1:3) solution for 90 s and rinsed with IPA. After that, the PMMA residue was removed with O_2 plasma (Plasma-Therm 790, O_2 10 sccm, 8 mT, 25W) for ~30 seconds. Next, chromium (Cr) adhesion layer of 5 nm followed by gold (Au) layer of 120 nm was deposited with e-beam evaporation. After that, the sample was lifted off in remover PG, and rinsed with IPA. After fabrication, the spirals were imaged using scanning electron microscope (SEM) (FEI Nova 200). Figure

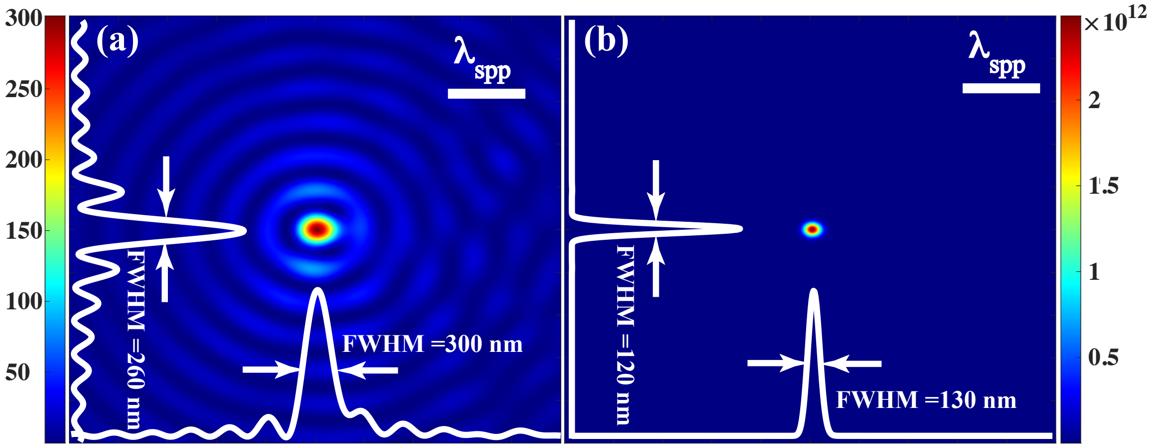

Figure 6.2: Time averaged (a) surface plasmon polariton intensity (I_{spp}) enhancement and (b) I_{spp}^5 enhancement at the center of gold Archimedean spiral photocathode obtained with finite difference time domain simulation using circularly polarized Gaussian pulse at 4° angle on incidence, central wavelength of 800 nm and pulse duration of 150 fs as the source of excitation. Here $\lambda_{\text{spp}} = 783$ nm.

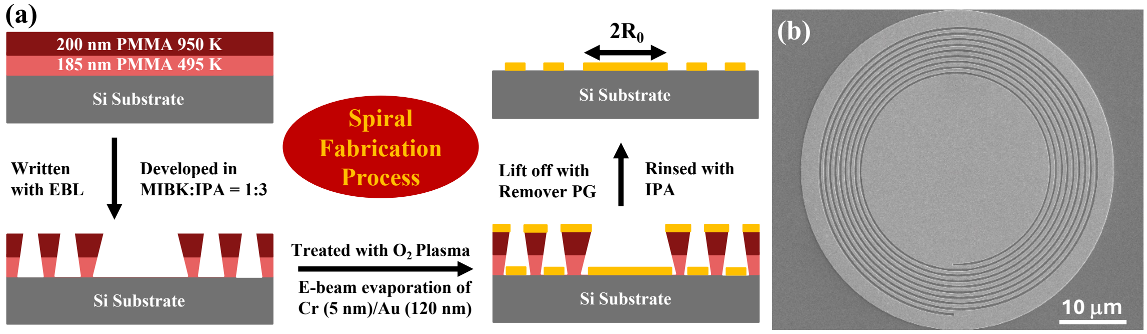

Figure 6.3: (a) Schematic of spiral fabrication process and (b) Scanning electron microscope (SEM) image of Archimedean gold spiral on the Si substrate with starting radius (R_0) = 12.5 μm.

6.3 (b) shows the scanning electron microscope (SEM) image of ASP on the Si substrate with starting radius (R_0) = 12.5 μm.

6.5 Results and Discussion

The fabricated ASP was transferred after a UHV bake-out at 120 °C for 1 day into a commercially available photoemission electron microscope (PEEM) with a 4° angle of incidence [Foc (2024)]. Initially, the ASP emitted only 0.001 electrons/shot with ∼2.5

kW of peak laser power from a $\sim$150 fs, 500 kHz, 800 nm pulsed laser focused down to $\sim$50 μm FWHM on the ASP. However, the electrons yield increased by several orders of magnitude in less than 5 minutes with peak laser power in the range of 0.7-2.5 kW incident on the ASP. After this initial ‘activation’ step, the enhanced electron emission stayed without any degradation for several days until the ASP was removed from the PEEM UHV environment of 10^{-10} torr into air. Upon re-insertion into the UHV PEEM after the UHV bake, the ASP required reactivation to get the previouly enhanced emisison. This indicates the above ‘laser activation’ process leads to cleaning of adsorbates from the atmosphere that were settled on the Au emisison surface enhancing the photoemisison current.

The real-space image was taken with Hg lamp and pulse femtosecond laser after the activation of the ASP. As we can see in Fig. 6.4, the Hg lamp image shows the structure of the spiral. The bright spot at the center of the spiral with $\sigma_x \sim 50$ nm is due to 5^{th} order non-linear electron emission due to focusing of light to sub-diffraction limited areas using plasmonic ASP. Please note that all the characterization measurements reported in this chapter were performed only with the pulsed femtosecond laser.

After *activation*, spatial distribution of non-linear electron emission spot size was measured as shown in Fig. 6.5 (a) at the peak pulse power of $\sim$1.8 kW. As we can see, the rms electron emission spot size is $\sim$50 nm suggesting 5^{th} order non-linearity in the photoemission process. The 5^{th} order non-linearity is further corroborated by measuring electrons/shot as a function of peak laser pulse power plotted on a double logarithmic scale as shown in Fig. 6.5 (b). Considering the work function (ϕ) of Au to be $\sim$5.4 eV, at least four quanta of SPP, each with energy $\hbar\omega = 1.58$ eV are required to overcome the the work function of Au making 4^{th} order as the lowest possible order of photoemission [Pierce *et al.* (2023, 2022); Dreher *et al.* (2023)]. However, for the case of Au, the large density of *d*-band initial states about 2 eV below the Fermi energy may result in enhanced contribution

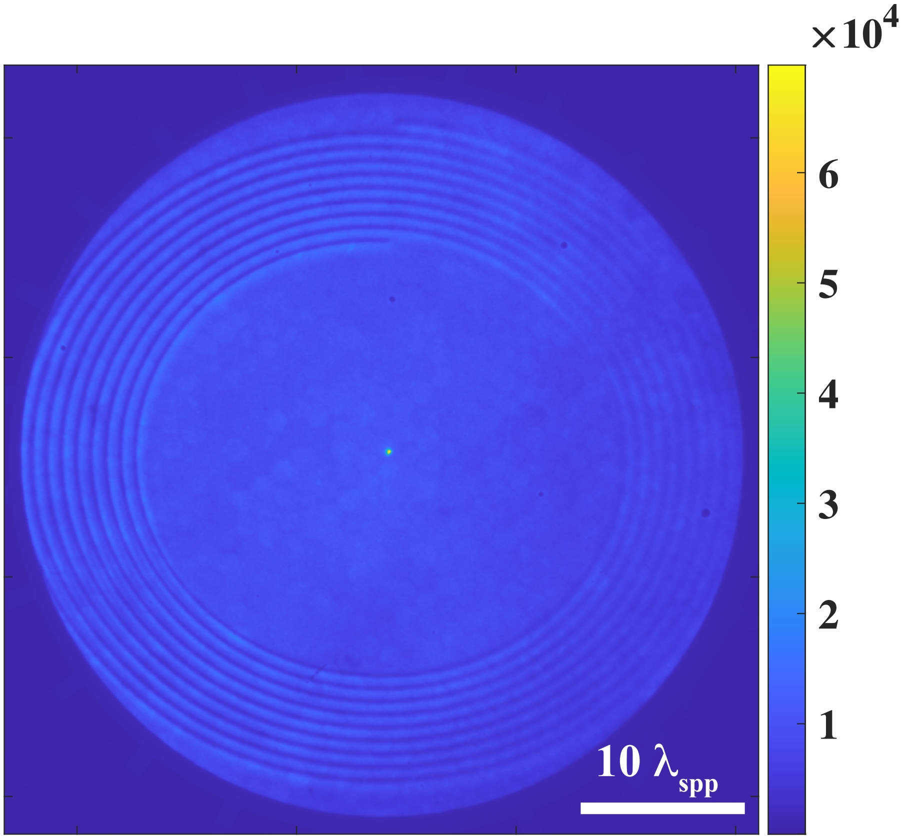

Figure 6.4: Real-space PEEM image taken with Mercury (Hg) lamp and pulsed femtosecond laser. The bright spot at the center of the spiral is due to 5^{th} order non-linear electron emission due to focusing of light to sub-diffraction limited area using plasmonic Archimedean spiral. The Hg lamp image shows the spiral structure. Here $\lambda_{\text{spp}} = 783$ nm.

and thereby lead to enhanced nonlinearities in the photoemission process. Inspection of Au band structure indicates a sharp increase of the joint density of states for total transition energies above 6.4 eV [Ramchandani (1970); Rangel *et al.* (2012); Kupratakuln (1970)]. At least five quanta of SPP are required to overcome the total transition energies ∼6.4 eV. Such 5^{th} order non-linearity in the electron emission process has also been observed previously from Au nano-tips in above threshold photoemission regime [Bormann *et al.* (2010)].

Figure 6.5 (c) shows evolution of rms electron emission spot size as a function of peak laser pulse power. The rms electron emission spot size is ∼50 nm over a wide range of peak

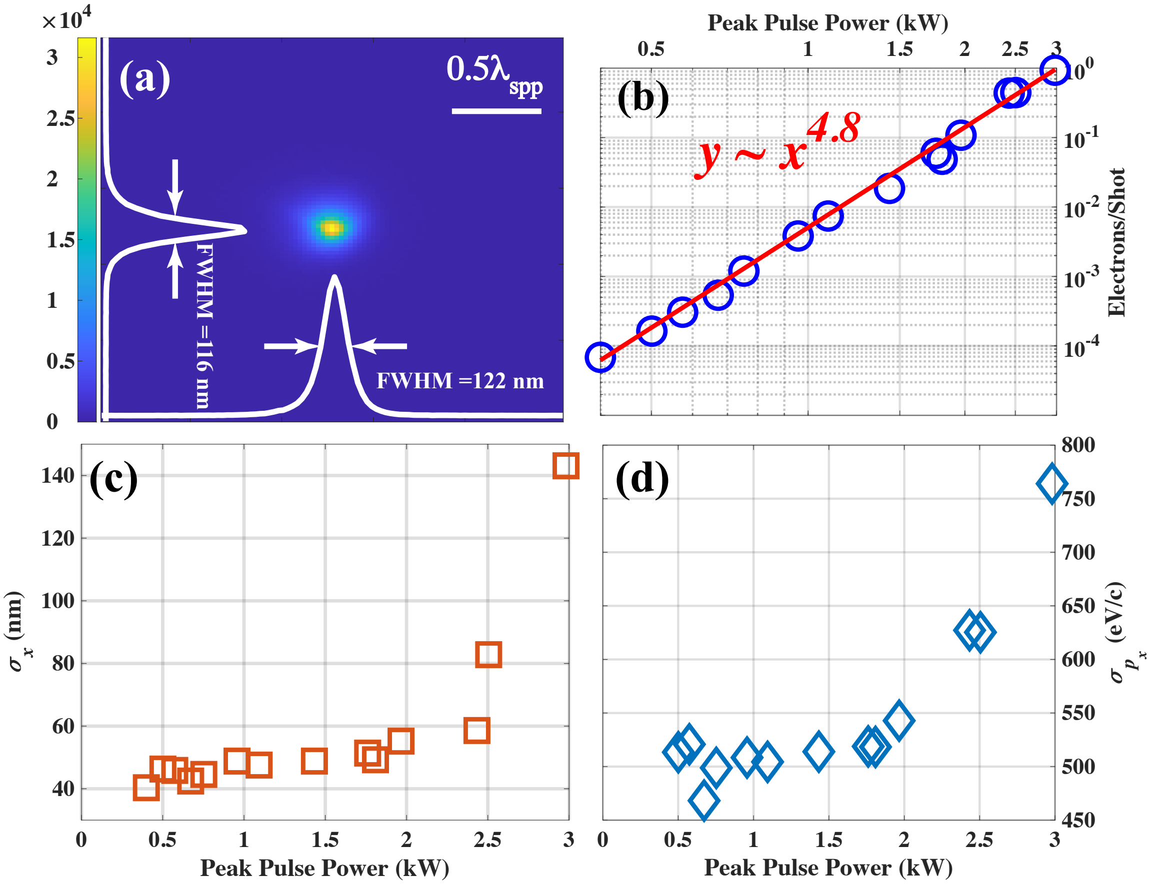

Figure 6.5: (a) Emission profile measured using PEEM with peak pulse power of ∼1.8 kW. (b) Logarithmic representation of electrons per shot emitted from gold Archimedean spiral photocathode as the function of peak laser pulse power. Evolution of experimentally determined (c) rms electron emission spot size and (d) rms momentum spread in the x-direction as a function of peak pulse power of femtosecond laser with the pulse length of 150 fs and central wavelength of 800 nm. Here $\lambda_{\text{spp}} = 783$ nm.

pulse power. Figure 6.5 (d) shows evolution of experimentally determined rms momentum spread of the emitted electrons as a function of peak laser pulse power. The rms momentum spread of the emitted electrons is ∼500 eV/c over a wide range of peak pulse power.

An average of 0.1 electron/shot are emitted up to a peak pulse power of ∼2.5 kW. Considering Poisson statistics, this corresponds to <1 % probability of 2 electrons being emitted per shot. However, beyond 2.5 kW an average of 0.5-1 electron/shot are emitted, and the probability of emission of 2 electrons/shot becomes 8-20 %. This results in Coulomb interaction between the electrons in the pulses with 2 or more electrons. This

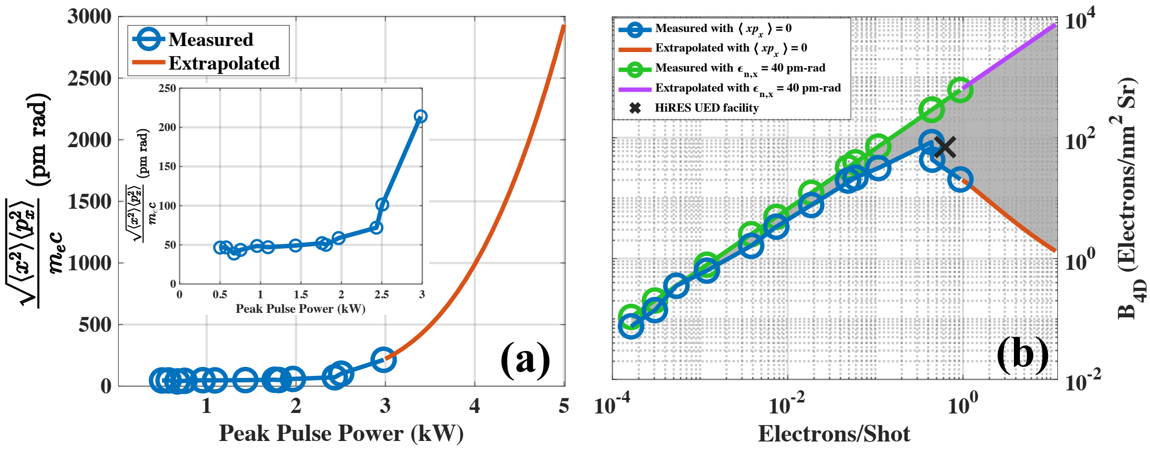

Figure 6.6: (a) Root mean square normalized transverse emittance with $\langle xp_x\rangle = 0$. The blue curve shows the experimental data points and the red curve is the extrapolated data. The inset shows the zoomed version of the experimental data points. (b) 4D-Brightness of the emitted electron bunch as a function of electrons/shot. The black cross (×) shows the 4D-Brightness obtained from HiRES UED facility. The red line is the extrapolated 4D-Brightness with $\langle xp_x\rangle = 0$. The magenta line is the extrapolated 4D-Brightness with $\varepsilon_{n,x} =$ 40 pm-rad. The gray shaded region is where the 4D-Brightness of ASP can potentially lie considering $\langle xp_x\rangle = 0$ or correlated xp_x growth with $\varepsilon_{n,x} =$ 40 pm-rad.

coulomb repulsion results in the increase in the electron emission spot size as well as the rms momentum spread beyond the peak pulse power of ∼2.5 kW as seen in Fig. 6.5 (c) and (d).

Assuming $\langle xp_x\rangle = 0$, we calculate the emittance from equation 6.1. This is plotted as a function of peak laser pulse power in Fig. 6.6 (a). Beyond peak pulse power of ∼2.5 kW, the increase in emittance is attributed to the Coulomb interaction between the emitted electrons. Below ∼2 kW with less than 0.1 electron/shot the emittance is nearly constant at ∼50 pm-rad, with the smallest emittance of 40 pm-rad measured at ∼0.001 electron/shot. These are the smallest emittances achieved from a flat photocathode. At 0.5-1 electrons/shot, the normalized transverse emittance measured was in the range of 70-200 pm rad respectively. It was not possible to reliably measure the σ_x and σ_{p_x} beyond 3 kW due to increased Coulomb interactions. Hence we used a cubic fit to extrapolate the emittance beyond these values as shown by the red curve in Fig. 6.6 (a).

It is informative to compare the emittance achieved from the plasmonic ASP to that of the other nano-tip based electron sources. For example, at 0.0012 electron/shot, normalized transverse emittance of 62 pm-rad with $\sigma_t \sim 230$ fs has been achieved from the silicon nanotip photo-emitter used in conjunction with a compact silicon-based electrostatic lens [Hirano *et al.* (2020)]. By triggering a Schottky emitter with an ultraviolet pulsed laser (λ = 400 nm and pulse energy $\sim$10 nJ), the normalized transverse emittance of $\sim$13.5 pm rad at $\sim$2 electrons/shot and $\sim$1.7 pm rad at <0.01 electrons/shot with $\sigma_t \sim 128$ fs has been achieved after collimation in the TEM gun and column [**?**. ASP is the only geometrically flat photocathode capable of delivering pico-meter scale emittance with $\sigma_t \sim 27$ fs (see Appendix B) that can be used in high electric field RF guns.

In order to characterize the ASP further, we compute the 4D-Brightness of the electron bunch using equation 2 and plot it against the electrons per shot as shown in Fig. 6.6 (b). Our measurements of σ_x and σ_{p_x} do not give us any information on the underlying correlations between x and p_x. In the absence of electron-electron Coulomb interactions the correlation term $\langle xp_x \rangle$ can be assumed to be 0. For bunch charges <0.1 electron/shot the $\langle x^2 \rangle \langle p_x^2 \rangle$ is nearly constant (less than 20% increase) and the brightness increases proportionately with electrons per shot as expected. However, beyond that both x and p_x increases due to Coulomb interactions and $\langle x^2 \rangle \langle p_x^2 \rangle$ blows up. In this region the brightness calculated by assuming $\langle xp_x \rangle = 0$ reaches a maximum of 85 electrons/(nm^{2}Sr) and then reduces due to the increase in $\langle x^2 \rangle \langle p_x^2 \rangle$. This is shown by the blue curve in Fig. 6.6 (b). The red curve corresponds to the brightness obtained from the extrapolated values of $\langle x^2 \rangle \langle p_x^2 \rangle$ in Fig. 6.6 (a). The Coulomb increase in $\langle x^2 \rangle$ and $\langle p_x^2 \rangle$ also results in increased x and p_x correlations causing $\langle xp_x \rangle$ to be greater than 0. The exact calculations or measurements of the correlations in x and p_x are complex and beyond the scope of this paper. If we assume a fully linearly correlated growth of x and p_x, the emittance of 40 pm-rad corresponding to the zero-coulomb-interactions-case (very low charge per bunch) could be recovered even for larger bunch charges using aberration free electron lenses. This gives us an upper limit to the brightness that can be obtained from ASP as shown by the green curve. The purple curve shows the brightness with the electrons/shot extrapolated in the range beyond 3 kW laser peak power. The gray area shows the region in which the brightness from ASPs could lie depending on the nature of the correlations developed in x and p_x due to the Coulomb interactions.

Fig. 6.6 (b) also shows the black cross ($\times$) symbol indicating the 4D-Brightness of the electron bunch obtained in the HiRES UED beamline from a flat cathode after using collimating apertures [Ji *et al.* (2019)]. It should be noted that this point indicates the brightness at the sample whereas the performance of the ASP is at the source.

To-date all electron sources using flat photocathodes have been operated with large μm-mm sized emission areas putting them in the regime where electron-electron Coulomb interactions can be modeled by assuming the electron bunch to be a continuous distribution of charge [Bazarov *et al.* (2009); Dowell (2019)]. In such cases, the accelerating electric field ($\mathscr{E}$) at the cathode limits the maximum charge density (σ_{max}) to $\sigma_{max} = \varepsilon_0 \mathscr{E}$. Here, ε_0 is vacuum permittivity. With an electric field of 6 MV/m as obtained in the PEEM with the small rms spot size of $\sim$50 nm, we get the maximum charge that can be extracted from ASPs to be $\sim$2 electrons/shot within this space charge assumption.

However, the space charge assumption breaks down for a few electrons and it is imperative to consider individual Coulomb interactions between each pair of electrons to a properly account for the Coulomb effects [Meier *et al.* (2023)]. As a result extraction of more than two electrons may be possible even at these small electric fields. Furthermore extraction of higher charges per bunch could be possible with larger electric fields in the range of 20-100 MV/m that are typically found in RF guns [Faillace (2014)].

It is also worth noting that the maximum laser fluence used in this experiment, after accounting for a factor of $\sim$300 in intensity enhancement is 5 mJ/cm^2. This is 20 times lower than the damage threshold of gold which is typically in the range of 100-1000 mJ/cm^2 [Krüger *et al.* (2007)]. Even with 3 times higher laser power, due to the 5th order emission process one can expect 200 times more charge per shot and potentially an increased brightness. The actual increase in charge and the brightness will then be determined by the electron-electron interaction dynamics.

The ultrafast and ultra-coherent ASP is the first step to develop next-generation state of the art ultra-bright electron sources for next-generation accelerator applications. For example, ASP can be combined with high quantum efficiency semiconductor thin films [Saha *et al.* (2022); Cultrera *et al.* (2016)] to further enhance the 4D-brightness of the emitted electron bunch.

Beyond the UED/M applications ASPs can also be used as the electron source for dielectric laser accelerators for the development of next generation compact accelerators which require $<$1 nm-rad normalized transverse emittance [England *et al.* (2014); Simakov *et al.* (2017)]. Additionally, the ASP and other types of plasmonic apertures [Dai *et al.* (2021)] can be arranged in an array to generate transversely shaped electron beams for powering novel coherent x-ray light sources [Graves *et al.* (2020)] as well as the next generation beam driven dielectric wakefield accelerators [Conde *et al.* (2017)].

In summary, we have fabricated and characterized plasmonics based, geometrically flat, ultra-coherent and ultrafast source of electron pulses suitable for UED/M experiments. We achieved a record low rms normalized transverse electron emittance of less than 40 pm-rad from a photocathode – more than three orders of magnitude lower than the best the emittance that has been achieved from a photocathode [Li *et al.* (2012)]. Such a plasmonics based low emittance electron source operating in IR light can impact a wide range of applications ranging from high repetition rate UED/M to next generation particle accelerators.

Chapter 7

PHOTONICS-INTEGRATED PHOTOCATHODES

Parts of this chapter were published in Ref. [Kachwala *et al.* (2023a)]

7.1 Abstract

Integrating the advances made in photonics with efficient electron emitters can result in the development of next generation photocathodes for various accelerator applications. In such photonics-integrated photocathodes, light can be directed using waveguides and other photonic components on the substrate underneath a thin ($<$100 nm) photoemissive film to generate electron emission from specific locations at sub-micron scales and at specific times at 100 femtosecond scales along with triggering novel photoemission mechanisms resulting in brighter electron beams and enabling unprecedented spatio-temporal shaping of the emitted electrons. In this work we have demonstrated photoemission confined in the transverse direction as small as 1 μm using a nanofabricated Si_3N_4 waveguide under a $\sim$5 nm thick cesium antimonide (Cs_3Sb) photoemissive film. This work demonstrates a proof of principle feasibility of such photonics-integrated photocathodes and paves the way to integrate the advances in the field of photonics and nanofabrication with photocathodes to develop next-generation high-brightness electron sources for various accelerator applications.

7.2 Introduction

Photoemission-driven electron sources, also known as photocathodes, play a crucial role in applications such as x-ray free electron lasers (XFELs), ultrafast electron scattering experiments (UES), linear colliders, and advanced acceleration schemes with extremely high gradients. The characteristics of photoemission from photocathodes, in conjunction with the driving laser, largely dictate the brightness and spatio-temporal profile of the generated electron beams. To produce high brightness electron bunches, most of the photoinjectors today use high QE low electron affinity semiconductor photocathodes (such as NEA GaAs) at their operating threshold. While significant efforts have been directed towards developing advanced laser shaping techniques and improving the intrinsic emittance (or MTE) of the cathode materials with high QE and small response time to produce the brightest electron beams with specific spatio-temporal profiles for diverse applications, relatively little attention has been paid to optimizing the interaction between the laser and the photocathode material. In most photoinjectors, the laser typically interacts with the cathode material from the front surface at normal or oblique angles of incidence as shown in Fig. 7.1. In this mode, although high QE and low MTE can be produced simultaneously, it comes at the cost of longer response time [Karkare *et al.* (2013)]. This is because the electrons are emitted from deep within the semiconductor surface at photon energies close to the band-gap due to the low absorption depths ranging beyond a few micrometer. For most of the applications, response time with sub-picosecond to picosecond timescales is desirable [Lessner *et al.* (2017)]. One way to achieve a smaller response time is by emitting from a few hundred's of nanometer within the semiconductor surface at photon energies close to the band-gap. This can be achived by photoemitting in the transmission mode as shown in Fig. 7.1. This can result in low MTE and a smaller response time but comes at the cost of extremely low QE. This is because, all the photons incident are not efficiently absorbed by a thin photoemissive material.

Photonics components nano-fabricated underneath a thin photoemissive film can result in advanced photocathode electron sources for several particle accelerator applications. For example, photonics waveguides under a thin film of a high quantum efficiency semiconductor cathode can cause the photons to be efficiently absorbed very close to the

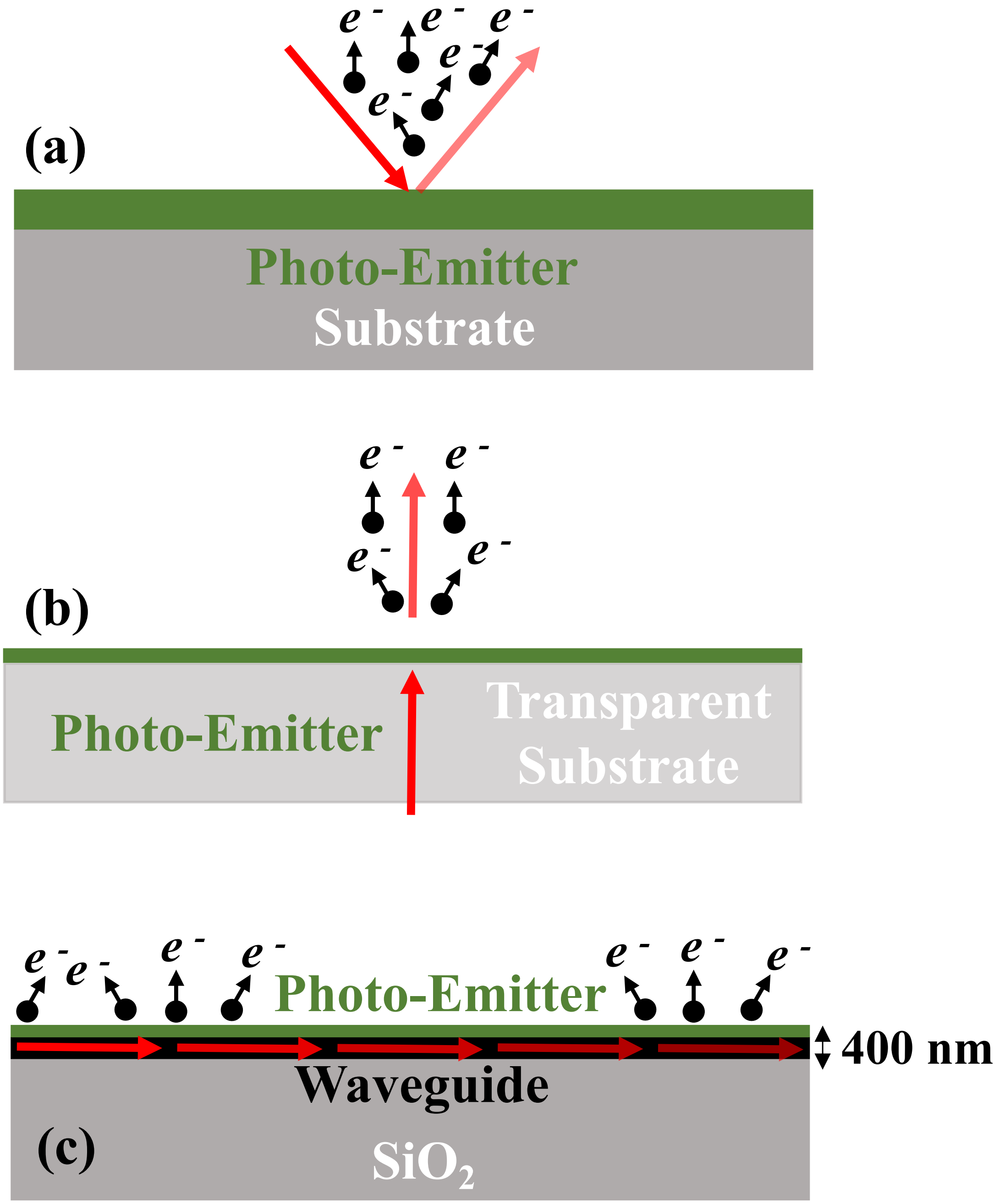

Figure 7.1: Schematic showing different modes of photoemission. (a) Reflective mode where the laser typically interacts with the cathode material from the front surface at normal or oblique angles of incidence. (b) Transmission mode where the laser typically interacts with the cathode material from the back surface at normal angle of incidence and (c) Evanescent mode where the light interacts with the photoemissive material evanescently from the back leading to photoemission from the front end of the photocathode.

surface resulting in high quantum efficiency (QE), low mean transverse energy (MTE) and quick response time simultaneously, thus providing higher brightness electron beams [Blankemeier *et al.* (2019)] by *evanescent mode* photoemission. Photonics components underneath a photoemissive surface can also be used to spatio-temporally shape the emitted electron beam by guiding light pulses to specific locations at the surface with sub-μm spatial and near 100 fs temporal resolution. This can potentially result in a new method for spatio-temporal shaping of electron beams with unprecedented resolution and enable having correlations in the spatial and temporal profiles.

Practically developing such structures has significant technological challenges related to coupling light in the waveguide structures, obtaining a thin photoemissive film on the nano-fabricated photonics substrate and practically using such cathodes in electron guns. In this work I present a design that can be used for coupling light, demonstrate the growth of thin ($\sim$5 nm) film of Cs_3Sb photocathode on the photonics integrated substrates, and finally using a Photoemisison Electron Microscope (PEEM) [Foc (2024)] to show that electron emission can be confined using photonic components like waveguides. The results presented below are a proof-of-principle demonstration of photonics based cathode technology and significantly alleviate the technological barrier towards integrating such sources in electron guns.

7.3 Light Coupling Techniques

Efficient coupling of light into the waveguide fabricated on the cathode substrates is essential to make effective photonics-integrated cathodes. In most photonic applications, this is done by connecting an optical fiber to the waveguide and then coupling light into the fiber [Zhu *et al.* (2016)]. However, as these photocathodes are used under Ultra High Vacuum (UHV) conditions, this technology of coupling light into the waveguide is infeasible as the sample cannot be transferred into the UHV chamber of an electron gun with an optical fiber connected to it. Connecting the fiber to the sample while it is in the electron gun under UHV is also non-trivial. Owing to these constraints, a coupling mechanism was designed using a grating coupler which was tested in the PEEM under UHV. The grating coupling mechanism is also compatible with the geometry of many standard DC and RF electron guns.

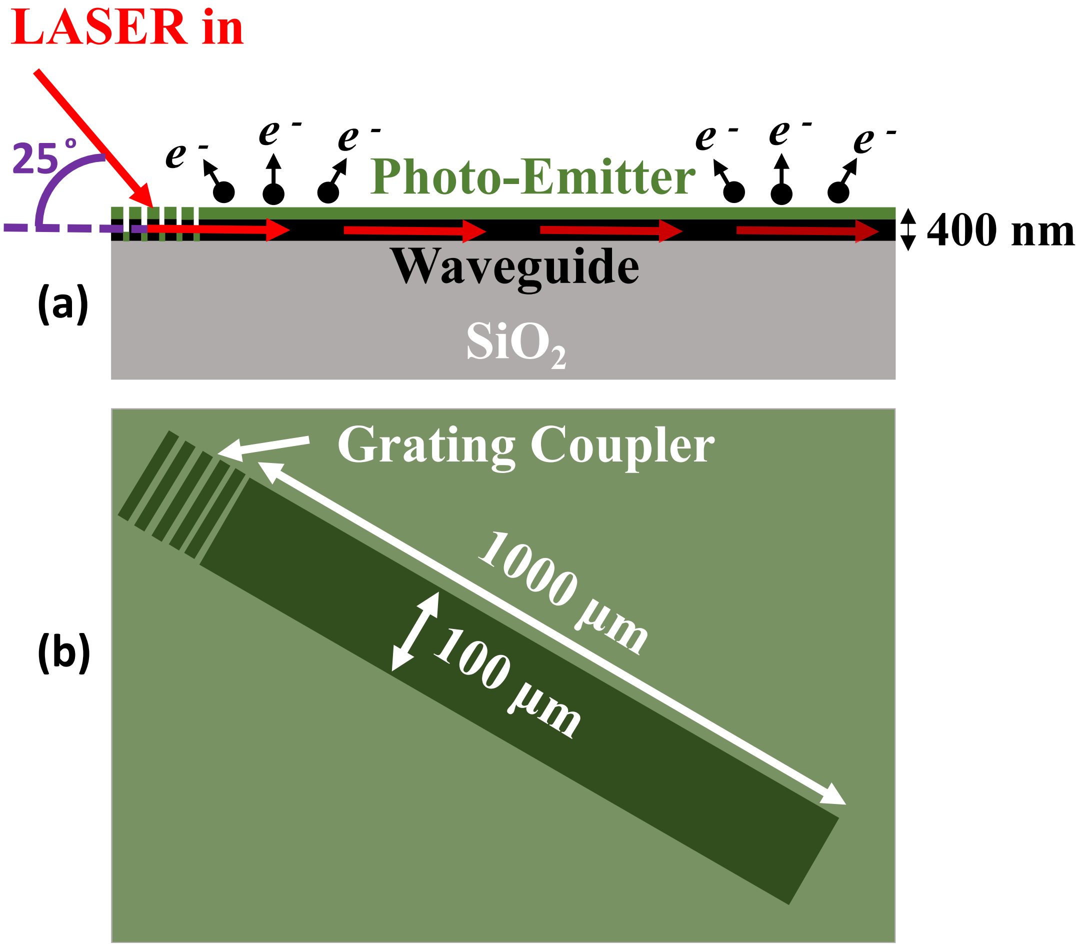

Figure 7.2: (a) Cross sectional view and (b) top view of light coupling into the waveguide using grating coupler.

The mechanism uses a grating coupler on the surface of the cathode with the laser incident at large angles with respect to the normal as shown in Figure 7.2. The grating coupler was designed to couple light at an angle of 65° w.r.t the normal at 532 nm wavelength. The angle of incidence was chosen based on the angle of incidence experimentally available in the PEEM instrument. Many RF and DC electron guns used for accelerators have such large angle of incidence ports [Bhattacharjee *et al.* (2012)].

7.4 Growth of Cesium Antimonide film

In photonics-integrated cathodes, the light from the waveguides nanofabricated on substrates is evanescently absorbed from the back of the photoemissive film to excite electrons. The photoexcited electrons are transported to the top surface of the film from where they are emitted. Hence, for an effective emission process in the transmission mode, it is necessary to have a thin ($<$100 nm) high-QE semiconductor film to be deposited on the waveguide. Simulations show that using a thin film of GaAs activated to negative electron affinity (NEA) placed on a photonic waveguide can simultaneously result in high QE, low MTE and a quick response time simultaneously resulting in high brightness electron beams [Blankemeier *et al.* (2019)]. Such thin NEA-GaAs cathodes are routinely used in the transmission mode in visible light. In the previous work, [Kachwala *et al.* (2022a)] a 40 nm thick Zn doped (p-dopant) epitaxial GaAs film onto the Si_3N_4 waveguide fabricated on SiO_2 substrate was transferred. However, the complex transfer process of epitaxial GaAs film onto the Si_3N_4 waveguide would result in breaking of the film in certain regions after the transfer is complete. As a result, a uniform emission along the length of the waveguide wasn't observed and this process was not easily reproducible. To circumvent this issue, instead of using a GaAs emisison layer, a ($\sim$5 nm) film of Cs_3Sb photocathode deposited directly on the Si_3N_4 waveguide fabricated on SiO_2 substrate. Below I outline the process of growing a $\sim$5 nm thick film of Cs_3Sb photocathode onto the Si_3N_4 waveguide.

The Si_3N_4 waveguide of length 1 mm, width 100 μm and thickness 400 nm along with a grating coupler was fabricated using electron beam lithography on a SiO_2 substrate. The sample fabricated was mounted onto an omicron type sample holder compatible with the PEEM sample stage and the UHV growth chamber used for the growth of Cs_3Sb

photocathode. Prior to the growth, the Si_3N_4 waveguide on SiO_2 substrate was annealed at 450 °C for 2-3 hours in an UHV growth chamber with a base pressure in the low 10^{-10} torr range. The Cs_3Sb cathode was grown via co-deposition of Cs and Sb on the Si_3N_4 waveguide fabricated on SiO_2 substrate. By shining a 5 mW green laser in the reflection mode, the photocurrent emitted from the cathode was measured during the growth to calculate the QE, which serves as a feedback to monitor the growth and performance of the cathodes. The growth was terminated by turning down the source heaters after ~15 minutes of growth. This corresponds to a film thickness of ~5 nm . Further details of the growth process can be found elsewhere [Saha *et al.* (2022)]. The final QE of the Cs_3Sb cathode was ~ 0.5% in green (λ = 530 nm) in the reflection mode before transfer into the PEEM.

After growth, the Cs_3Sb photocathode on Si_3N_4 waveguide fabricated on SiO_2 substrate was transported via a UHV transfer line into the PEEM [Foc (2024)]. The pressure in the transfer line was in 10^{-10} torr range and no QE degradation was observed during the transfer. The base pressure of the PEEM chamber was also in the low 10^{-10} torr range during the measurements.

7.5 Demonstration of Confined Emission using PEEM

PEEM produces images of electrons emitted from a surface with a sub 40-nm lateral resolution. A 500 kHz repetition rate femtosecond pulsed laser with a pulse length of 150 fs and wavelength 532 nm obtained from the LightConversion ORPHEUS optical parametric amplifier pumped by the LightConversion PHAROS was made incident onto the sample at 65° angle of incidence with respect to the normal of the sample surface. The spot size was focused down to 100 μm X 250 μm on the sample surface. All measurements were performed with sufficiently low power to avoid non-linear emission and space charge effects.

Figure 7.3 (a) shows the schematic of Si_3N_4 waveguide. A ~5 nm thick Cs_3Sb film was grown on the sample. To couple light into the waveguide, it was made incident on the grating coupler. Figure 7.3 (b) shows a PEEM image demonstrating that the emission is confined only to regions of the Cs_3Sb photocathode layer over the Si_3N_4 waveguide for coupling wavelength $\lambda = 532$ nm.

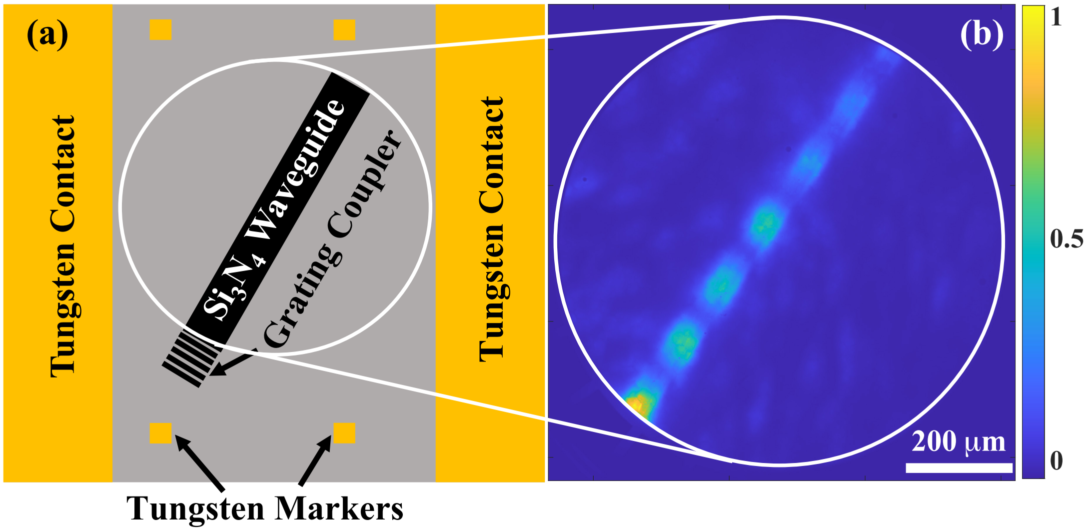

Figure 7.3: (a) Schematic of the fabricated sample and (b) first PEEM image showing confined emission from a ~5 nm thick film of Cs_3Sb photoemitting film for coupling wavelength $\lambda = 532$ nm.

Figure 7.4 shows the graph of beating pattern with spatial period (Λ) as a function of the different coupling wavelengths (λ). As we can see, the period of the pattern increases as we go from $\lambda = 525$ nm to $\lambda = 539$ nm. Si_3N_4 waveguide with the cross section of the order of wavelength and high aspect ratios support fundamental as well as higher order modes at a single wavelength. These transverse patterns are formed due to interference between these co-propagating modes and thereby generating beating patterns with significant evanescent intensities that causes the electron emission. Further theoretical investigation is underway to understand and characterize these patterns.

The *evanescent mode* waveguide confined photoemission can be used to produce any arbitrarily shaped electron beams. To demonstrate a proof-of-concept feasibility, we

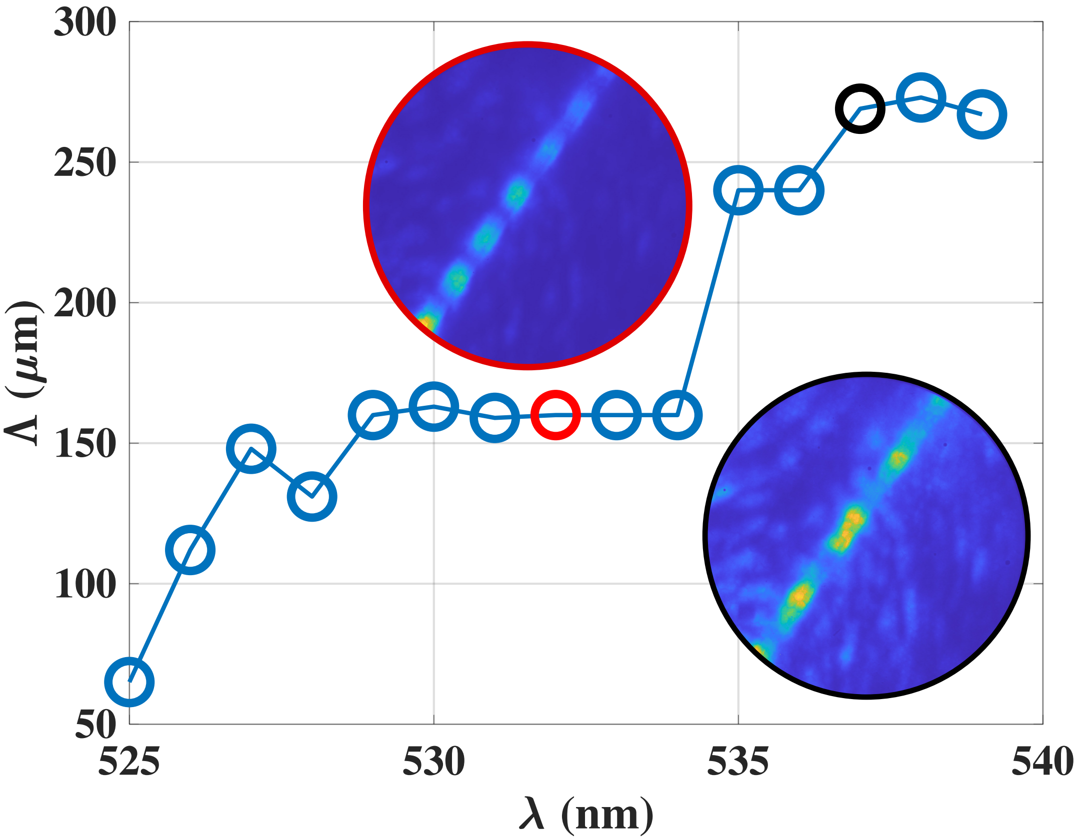

Figure 7.4: Beating pattern with spatial period (Λ) as a function of coupling wavelength (λ).

fabricated a Si_3N_4 waveguide with silicon dioxide (SiO_2) blocks (thickness ~600 nm) deposited on the top of it to block the evanescent light reaching the Cs_3Sb photoemitter. The schematic of the fabricated geometry is shown in Fig. 7.5. A ~5 nm thick film of Cs_3Sb with QE of ~0.5 % was deposited on the top of the waveguide (as well as SiO_2 blocks). Figure 7.6 shows the a series of PEEM images demonstrating that the emission is confined only to regions of the Cs_3Sb photocathode layer over the Si_3N_4 waveguide which is not covered by the SiO_2 blocks. The coupling wavelength (λ) was 522 nm.

The *evanescent mode* waveguide confined photoemission can be used to produce any transversely shaped electron beams with transverse dimensions as small as 1 μm. Figure 7.7 shows the schematic of the fabricated waveguide with dimensions of 1 μm, 2 μm, 5

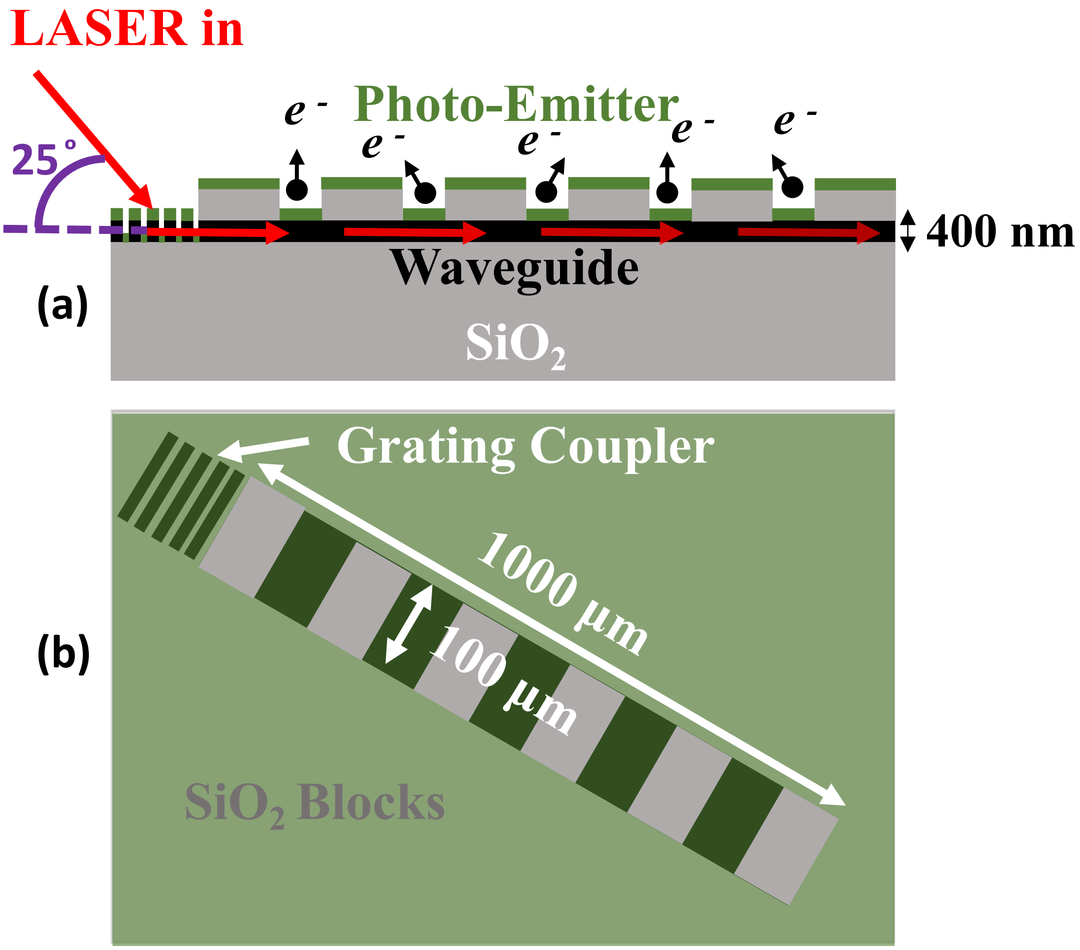

Figure 7.5: (a) Cross sectional view and (b) top view of light coupling into the waveguide using grating coupler with silicon dioxide (SiO_2) blocks (thickness ∼600 nm) deposited on the top of the Si_3N_4 waveguide.

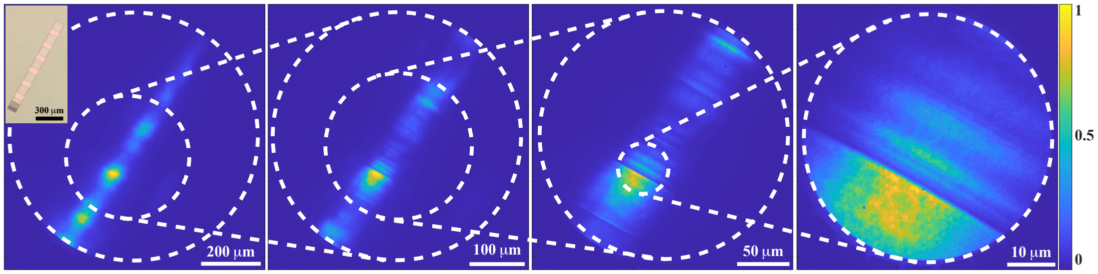

Figure 7.6: Evanescent mode confined photoemission from a ∼5 nm thick film of Cs_3Sb photoemitting film with SiO_2 blocks (thickness ∼600 nm) deposited on the top of the Si_3N_4 waveguide for coupling wavelength $\lambda = 522$ nm. The inset of the figure shows the optical microscope image of the SiO_2 blocks deposited on the top of the Si_3N_4 waveguide.

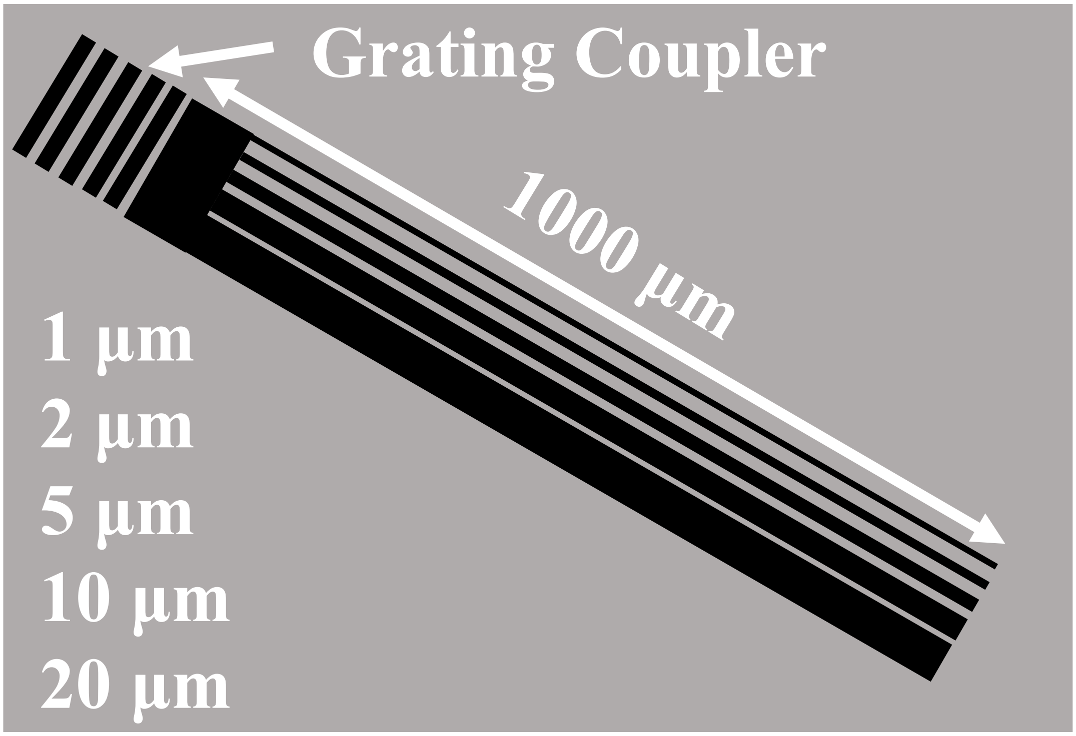

Figure 7.7: Cross-sectional cartoon schematic of the multiple waveguide pattern with the smallest transverse waveguide dimension of 1μm and the largest transverse waveguide dimension of 20μm.

μm, 10 μm and 20 μm. A $\sim$5 nm thick film of Cs_3Sb with QE of $\sim$0.5 % was deposited on the top of the waveguide with multiple transverse dimensions. Figure 7.8 shows the a series of PEEM images demonstrating that the emission can be confined to any arbitrary transverse dimensions with the smallest being 1 μm demonstrated in this thesis. The coupling wavelength (λ) was 522 nm.

7.6 Conclusion and Future Work

In this work, we have developed photonics-integrated photocathodes and demonstrated photoemission confined to the transverse direction using a nanofabricated Si_3N_4 waveguide underneath a $\sim$5 nm thick Cs_3Sb photocathode, thus demonstrating a proof of principle feasibility of tailored emission from photonics-integrated photocathodes. In addition, we

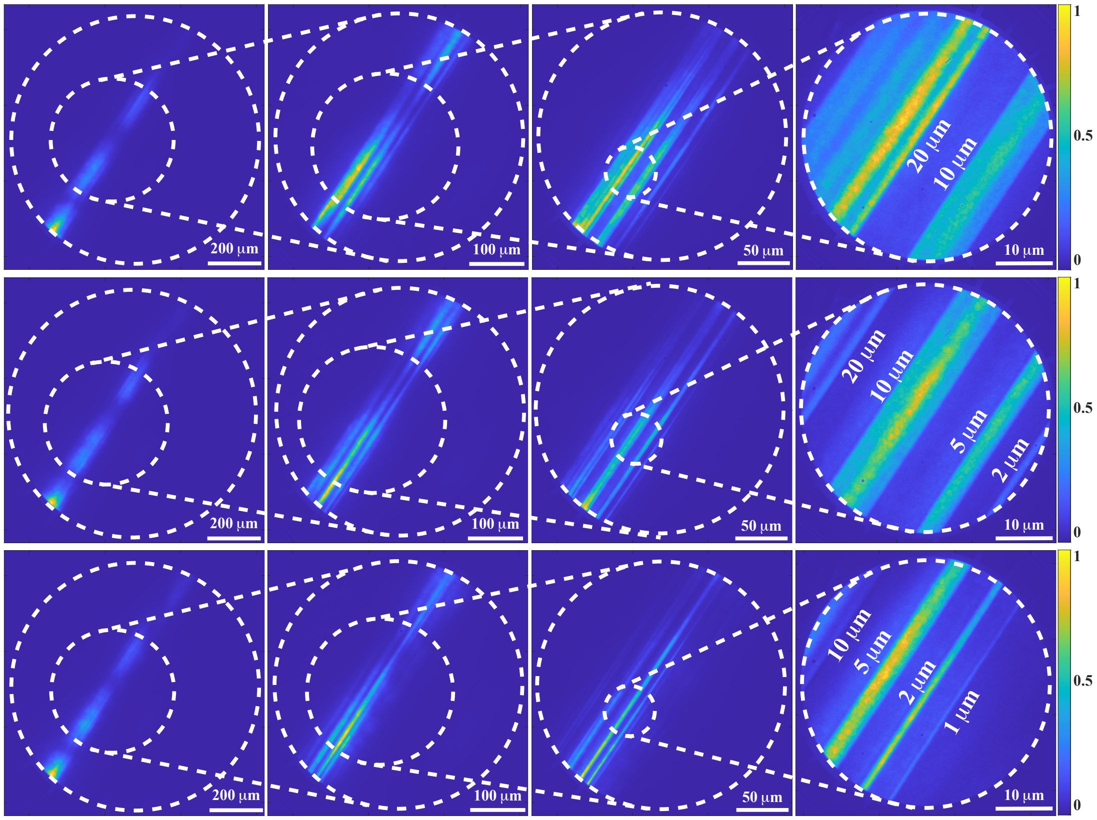

Figure 7.8: Evanescent mode confined photoemission from a ∼5 nm thick film of Cs_3Sb photoemitting film with multiple waveguide pattern with the smallest transverse waveguide dimension of 1 μm and the largest transverse waveguide dimension of 20 μm with ∼300 nm spatial resolution and coupling wavelength $\lambda = 522$ nm.

also demonstrated transverse shaping of the emitted electrons along the length of the waveguide due to interference between the co-propagating modes within the waveguide. Further, we also demonstrated arbitrary shaping of electron beam using SiO_2 blocks on the Si_3N_4 waveguide. We also demonstrated electron emission confined transversely to as small as 1 μm along the length of the waveguide. This proof-of-feasibility of demonstration of photonics based cathodes serves as a first step to make technologically advanced brighter photocathodes by simultaneously having a high QE, low MTE and a quick response time.

Further theoretical investigation is underway to understand the transverse patters along the length of the waveguide due to coupling of co-propogating modes in the waveguide. As a next step, more complex integrated photonic substrate can be designed for advanced spatio-temporal shaping of electron bunches. This includes development of more advanced photonic circuits using multiple passive components like delay lines, combiners and splitters to route photons to desired locations, and mirrors to enable local beam shaping, all embedded into the cathode substrate to achieve advanced spatio-temporal tuning to mitigate space-charge effects and achieve high brightness electron emission. Further, photonics waveguides can be designed for circularly polarized light and integrated with low electron affinity GaAs thin films ($<$100 nm) to generate transversely shaped spin polarized electron beams.

Chapter 8

CONCLUSION AND FUTURE DIRECTIONS

Photoinjectors, renowned for producing electron beams of unparalleled brightness, are pivotal to numerous high-impact scientific endeavors, including free electron lasers, ultrafast electron diffraction and microscopy experiments, and inverse Compton scattering x-ray sources. Among the critical components of a photoinjector, the photocathode plays a central role, as its quantum efficiency, mean transverse energy, response time, electron energy spread of emitted electrons, and lifetime/robustness collectively determine the quality of the electron bunch generated for the aforementioned applications. Notably, a Photoemission Electron Microscope emerges as a standout instrument capable of simultaneously measuring these parameters. In this thesis, for the first time, PEEM was utilized as a tool for characterizing nanostructured electron sources developed for next-generation accelerator applications. Throughout this thesis, we embark on designing and characterizing several nanostructured electron sources with an objective of enhancing their brightness. Nonetheless, numerous avenues within this field remain unexplored. This chapter will provide a succinct overview of some of these promising future research directions.

In Chapter 3 we studied the spectral responses of QE, photoemission electron energy spectra (PEES) and MTE of the (N)UNCD photocathode. With the QE comaparable to that of metal photocathodes and MTE of 70 meV at the threshold, (N)UNCD photocathodes are suitable for various robust photoinjector applications. However, use of these photocathodes at high electric field gradients can significantly increase the MTE of the emitted electrons owing to their surface roughness. Consequently, it can lead to decrease in brightness of the emitted electron beams. Even at low electric fields, the contribution to MTE due to physical and chemical roughness is significant enough to increase MTE beyond the thermal limit at the threshold. One way to reduce MTE and consequently increase the brightness of (N)UNCD photocathodes is by optimizing the growth techniques to produce a smoother film. One way to do this would involve growing (N)UNCD films via tungsten interlayers [Naguib *et al.* (2006)]. As a result, future work can involve growing (N)UNCD films with reduced surface roughness and additional fundamental understanding of their emission mechanism.

In Chapter 4 we measured PEES, MTE and QE of Cs_3Sb photocathodes in the photon energy range of 1.45-2.33 eV. The PEES indicate that the work function of the Cs_3Sb cathodes is 1.5 ± 0.1 eV, significantly lower than the ~ 2.1 eV value that was previously reported based on the QE spectral response. The value of MTE at this work function of 1.5 eV was observed to be $\sim$30 meV - very close to the 25 meV at 300 K within instrumental error. Despite the low MTE, it might not be feasible to operate these cathodes at this photon energy given their low QE of the order of 10^{-7} (comparable to metal cathodes). As a result, the cathodes may need to be operated at photon energies away from the threshold, which would lead to higher MTE as a consequence of higher excess energy. Epitaxial, single-crystalline Cs_3Sb cathodes and other alkali-antimonides may, however, exhibit different photoemission features when operated at the threshold. It would be worthwhile to pursue photoemission studies of these cathodes to pave the way for brighter electron beams.

Exploring the low-temperature characteristics of the above mentioned photocathodes represents a significant future trajectory for the field. Cold photocathodes may exhibit superior properties compared to those operating at room temperature. Cooling them can reduce the size of the Fermi tail of the electron occupation function, potentially lowering the MTE of the photocathodes [Karkare *et al.* (2020)]. Additionally, research indicates that electron-phonon scattering could be a crucial mechanism influencing the MTE of certain semiconductor photocathodes. Cooling the system alters the occupation of phonon modes in the material, which could consequently impact the cathode's properties. The cryogenically cooled DC electron gun at ASU presents a valuable tool for investigating the photoemission behavior of these cathodes at cryogenic temperatures.

Chapter 5 presents non-linear photoemission studies from the (N)UNCD pyramid tip cathode. In this work for the first time, we measured the photoemission electron energy spectra from the (N)UNCD pyramid tip cathode.

In Chapter 6, we showcase the utilization of a plasmonic Archimedean spiral photocathode (ASP), unveiling an emission spot size (σ_x) of approximately 50 nm rms. This achievement leads to a (record low) emittance of less than 40 pm-rad a remarkable advancement exceeding three orders of magnitude compared to the previously demonstrated best emittance of less than 50 nm-rad from a photocathode. The ultrafast and ultra-coherent ASP marks the initial stride toward developing next-generation, state-of-the-art ultra-bright electron sources for advanced accelerator applications. For instance, the ASP can be synergistically combined with high quantum efficiency semiconductor thin films [Saha *et al.* (2022, 2021); Cultrera *et al.* (2011)] to further elevate the 4D-brightness of the emitted electron bunch. Moreover, the exploration of plasmonic bow-tie structures as electron sources or the amalgamation of ASP with plasmonic bow-tie structures to create hybrid plasmonic photocathodes holds promise for further diminishing the emittance of emitted electrons and fostering the development of state-of-the-art ultrabright electron sources [Ghosh and Dhawan (2021)]. To illustrate, even with just 1 electron per shot, featuring σ_x of approximately 10 nm rms and a MTE of around 500 meV, an emittance of less than 10 pm-rad can be achieved. Such a feat would result in a record 4D-Brightness of approximately 10,000 electron/(nm^{2}Sr).

Lastly, in Chapter 7, using PEEM, we demonstrate a new mode, 'evanescent mode' photoemssion from novel photonics integrated cathodes. Here, we demonstrate photoemission confined in the transverse direction as small as 1 μm using a nanofabricated

Si_3N_4 waveguide under a $\sim$5 nm thick Cs_3Sb photoemissive film. This work demonstrates a proof of principle feasibility of such photonics-integrated photocathodes and paves the way to integrate the advances in the field of photonics and nanofabrication with photocathodes to develop next-generation high-brightness electron sources for various accelerator applications.

(N)UNCD pyramid tip cathode as well as ASP and other types of plasmonic apertures [Dai *et al.* (2021)] can be arranged in an array to generate transversely shaped electron beams. The transversely shaped electron beams generated have also been demonstarted from the photonics integrated cathodes. These transversely shaped electron beams can be used for powering novel coherent x-ray light sources [Graves *et al.* (2020)] as well as the next generation beam driven dielectric wakefield accelerators [Conde *et al.* (2017)].

Indeed, achieving the ultimate limit of electron beam brightness dictated by the quantum limit is a significant challenge at present. However, the future holds great promise for the advancement of bright electron sources. With continued material research, innovative accelerator designs as well as use of plasmonic and photonics integrated photocathodes, there exists a potential to improve the brightness of electron beams by as much as 1000 times. Such enhancements could revolutionize the field, making techniques that were once exclusive only to the national labs with billion-dollar budgets accessible to university users. This opens up a new realm of possibilities for time-resolved experiments on complex systems, allowing researchers to delve deeper into the nature of large and dynamic molecular systems as well as imaging complex protein structures. The production of new, brighter electron beams has the power to transform the landscape of atomic-scale science with their integration in the transmission electron microscopes. Photocathodes are likely to play a crucial role in realizing this future. As we continue to push the boundaries of scientific exploration, the development of novel and improved photocathode technologies will be essential for unlocking the full potential of advanced electron beam applications.

REFERENCES

FOCUS-IS-IEF-PEEM, `https://www.focus-gmbh.com` (2024).

Principal Properties of Diamond, `http://www.chm.bris.ac.uk/motm/diamond/diamprop.htm` (2024).

Ansys-Lumerical-FDTD, `https://www.ansys.com` (2024).

Amaldi, U., “The importance of particle accelerators”, europhysics news **31**, 6, 5–9 (2000).

Amiranoff, F., S. Baton, D. Bernard, B. Cros, D. Descamps, F. Dorchies, F. Jacquet, V. Malka, J. Marques, G. Matthieussent *et al.*, “Observation of laser wakefield acceleration of electrons”, Physical Review Letters **81**, 5, 995 (1998).

Andonian, G., “Electron-beam driven dielectric wakefield accelerator experiments in the terahertz regime”, in “AIP Conference Proceedings”, vol. 1507, pp. 94–102 (American Institute of Physics, 2012).

Andrews, H., K. Nichols, D. Kim, E. I. Simakov, S. Antipov, G. Chen, M. Conde, D. Doran, G. Ha, W. Liu *et al.*, “Shaped beams from diamond field-emitter array cathodes”, IEEE Transactions on Plasma Science **48**, 7, 2671–2675 (2020).

Aschenauer, E., M. Baker, A. Bazilevsky, K. Boyle, S. Belomestnykh, I. Ben-Zvi, S. Brooks, C. Brutus, T. Burton, S. Fazio *et al.*, “erhic design study: an electron-ion collider at bnl”, arXiv preprint arXiv:1409.1633 (2014).

Auciello, O., S. Renou, K. Kang, D. Tasat and D. Olmedo, “A biocompatible ultrananocrystalline diamond (uncd) coating for a new generation of dental implants”, Nanomaterials **12**, 5, 782 (2022).

Bae, J., I. Bazarov, L. Cultrera, J. Maxson, P. Musumeci, X. Shen, S. Karkare and H. Padmore, “Multi-photon photoemission and ultrafast electron heating in cu photocathodes at threshold”, TUPML026 (2018).

Bazarov, I. V., B. M. Dunham, Y. Li, X. Liu, D. G. Ouzounov, C. K. Sinclair, F. Hannon and T. Miyajima, “Thermal emittance and response time measurements of negative electron affinity photocathodes”, Journal of Applied Physics **103**, 5, 054901 (2008).

Bazarov, I. V., B. M. Dunham and C. K. Sinclair, “Maximum achievable beam brightness from photoinjectors”, Physical review letters **102**, 10, 104801 (2009).

Benson, S., M. Bruker, A. V. Fedotov, X. Gu, C. Gulliford, J. Guo, A. Hutton, J. Kewisch, D. Kayran, V. Ptitsyn *et al.*, “Low-energy cooling for electron ion collider”, Tech. rep., Brookhaven National Lab.(BNL), Upton, NY (United States) (2020).

Bhattacharjee, D., R. Tiwari, D. Jayaprakash, R. Mishra, A. Tillu, B. Nayak, R. Chavan, S. Chandan, V. Yadav, S. Ghodke *et al.*, “Development of electron guns for linacs and dc accelerator”, in “Journal of Physics: Conference Series”, vol. 390, p. 012071 (IOP Publishing, 2012).

Bionta, M., B. Chalopin, A. Masseboeuf and B. Chatel, “First results on laser-induced field emission from a cnt-based nanotip”, Ultramicroscopy **159**, 152–155 (2015).

Bionta, M. R., S. J. Weber, I. Blum, J. Mauchain, B. Chatel and B. Chalopin, “Wavelength and shape dependent strong-field photoemission from silver nanotips”, New Journal of Physics **18**, 10, 103010 (2016).

Biswas, J., E. Wang, M. Gaowei, W. Liu, O. Rahman and J. T. Sadowski, “High quantum efficiency gaas photocathodes activated with cs, o2, and te”, AIP Advances **11**, 2, 025321 (2021).

Blankemeier, L., F. Rezaeifar, A. Garg and R. Kapadia, “Integrated photonics for low transverse emittance, ultrafast negative electron affinity gaas photoemitters”, Journal of Applied Physics **126**, 3, 033102 (2019).

Bonse, J., J. Krüger, S. Höhm and A. Rosenfeld, “Femtosecond laser-induced periodic surface structures”, Journal of laser applications **24**, 4 (2012).

Booth, L., S. A. Catledge, D. Nolen, R. G. Thompson and Y. K. Vohra, “Synthesis and characterization of multilayered diamond coatings for biomedical implants”, Materials **4**, 5, 857–868 (2011).

Bormann, R., M. Gulde, A. Weismann, S. V. Yalunin and C. Ropers, “Tip-enhanced strong-field photoemission”, Physical review letters **105**, 14, 147601 (2010).

Borowiec, A. and H. Haugen, “Subwavelength ripple formation on the surfaces of compound semiconductors irradiated with femtosecond laser pulses”, Applied Physics Letters **82**, 25, 4462–4464 (2003).

Breuer, J. and P. Hommelhoff, “Laser-based acceleration of nonrelativistic electrons at a dielectric structure”, Physical Review Letters **111**, 13, URL `https://doi.org/10.1103%2Fphysrevlett.111.134803` (2013).

Carter, C. B. and D. B. Williams, *Transmission electron microscopy: Diffraction, imaging, and spectrometry* (Springer, 2016).

Chatelain, R. P., V. R. Morrison, C. Godbout and B. J. Siwick, “Ultrafast electron diffraction with radio-frequency compressed electron pulses”, Applied Physics Letters **101**, 8 (2012).

Che, J., T. Çağın, W. Deng and W. A. Goddard III, “Thermal conductivity of diamond and related materials from molecular dynamics simulations”, The Journal of Chemical Physics **113**, 16, 6888–6900 (2000).

Chen, G., G. Adhikari, L. Spentzouris, K. K. Kovi, S. Antipov, C. Jing, W. Andreas Schroeder and S. V. Baryshev, “Mean transverse energy of ultrananocrystalline diamond photocathode”, Applied Physics Letters **114**, 9, 093103 (2019).

Chen, G., L. Spentzouris, C. Jing, M. Conde, G. Ha, W. Liu, J. Power, E. Wisniewski, A. V. Sumant, S. Antipov *et al.*, "Demonstration of nitrogen-incorporated ultrananocrystalline diamond photocathodes in a rf gun environment", Applied Physics Letters **117**, 17, 171903 (2020).

Chen, W., D. C. Abeysinghe, R. L. Nelson and Q. Zhan, "Experimental confirmation of miniature spiral plasmonic lens as a circular polarization analyzer", Nano letters **10**, 6, 2075–2079 (2010).

Chubenko, O., S. S. Baturin and S. V. Baryshev, "Theoretical evaluation of electronic density-of-states and transport effects on field emission from n-type ultrananocrystalline diamond films", Journal of Applied Physics **125**, 20, 205303 (2019).

Conde, M., S. Antipov, D. Doran, W. Gai, Q. Gao, G. Ha, C. Jing, W. Liu, N. Neveu, J. Power *et al.*, "Research program and recent results at the argonne wakefield accelerator facility (awa)", Proc. IPAC'17 pp. 2885–2887 (2017).

Cultrera, L., I. Bazarov, A. Bartnik, B. Dunham, S. Karkare, R. Merluzzi and M. Nichols, "Thermal emittance and response time of a cesium antimonide photocathode", Applied Physics Letters **99**, 15, 152110 (2011).

Cultrera, L., C. Gulliford, A. Bartnik, H. Lee and I. Bazarov, "Ultra low emittance electron beams from multi-alkali antimonide photocathode operated with infrared light", Applied Physics Letters **108**, 13 (2016).

Cultrera, L., S. Karkare, H. Lee, X. Liu, I. Bazarov and B. Dunham, "Cold electron beams from cryocooled, alkali antimonide photocathodes", Physical Review Special Topics-Accelerators and Beams **18**, 11, 113401 (2015).

Dai, Y., Z. Zhou, A. Ghosh, S. Yang, C.-B. Huang and H. Petek, "Ultrafast nanofemto photoemission electron microscopy of vectorial plasmonic fields", MRS Bulletin **46**, 8, 738–746 (2021).

Davis, P., G. Hairapetian, C. Clayton, C. Joshi, S. Hartman, S. Park, C. Pellegrini and J. Rosenzweig, "Quantum efficiency measurements of a copper photocathode in an rf electron gun", in "Proceedings of International Conference on Particle Accelerators", pp. 2976–2978 (IEEE, 1993).

Dowell, D., I. Bazarov, B. Dunham, K. Harkay, C. Hernandez-Garcia, R. Legg, H. Padmore, T. Rao, J. Smedley and W. Wan, "Cathode r&d for future light sources", Nuclear Instruments and Methods in Physics Research Section A: Accelerators, Spectrometers, Detectors and Associated Equipment **622**, 3, 685–697 (2010).

Dowell, D. H., "Topological cathodes: Controlling the space charge limit of electron emission using metamaterials", Physical Review Accelerators and Beams **22**, 8, 084201 (2019).

Dowell, D. H. and J. F. Schmerge, "Quantum efficiency and thermal emittance of metal photocathodes", Physical Review Special Topics-Accelerators and Beams **12**, 7, 074201 (2009a).

Dowell, D. H. and J. F. Schmerge, "Quantum efficiency and thermal emittance of metal photocathodes", Physical Review Special Topics-Accelerators and Beams **12**, 7, 074201 (2009b).

Drees, A., "Heavy ions in rhic—how to get to higher luminosities?", Acta Physica Hungarica A) Heavy Ion Physics **25**, 2, 475–486 (2006).

Dreher, P., D. Janoschka, B. Frank, H. Giessen and F.-J. Meyer zu Heringdorf, "Focused surface plasmon polaritons coherently couple to electronic states in above-threshold electron emission", Communications Physics **6**, 1, 15 (2023).

Dunham, B., J. Barley, A. Bartnik, I. Bazarov, L. Cultrera, J. Dobbins, G. Hoffstaetter, B. Johnson, R. Kaplan, S. Karkare *et al.*, "Record high-average current from a high-brightness photoinjector", Applied Physics Letters **102**, 3, 034105 (2013).

Durham, D., K. Siddiqui, F. Ji, J. G. Navarro, P. Musumeci, R. Kaindl, A. Minor and D. Filippetto, "Relativistic ultrafast electron diffraction of nanomaterials", Microscopy and Microanalysis **26**, S2, 676–677 (2020).

Durham, D. B., C. M. Pierce, F. Riminucci, S. R. Loria, K. Kanellopulos, I. Bazarov, J. Maxson, S. Cabrini, A. M. Minor and D. Filippetto, "Characterizing plasmon-enhanced photoemitters for bright ultrafast electron beams", in "Plasmonics: Design, Materials, Fabrication, Characterization, and Applications XIX", vol. 11797, pp. 151–156 (SPIE, 2021).

Egerton, R. F., "Electron energy-loss spectroscopy in the tem", Reports on Progress in Physics **72**, 1, 016502 (2008).

Elsayed-Ali, H., T. Norris, M. Pessot and G. Mourou, "Time-resolved observation of electron-phonon relaxation in copper", Physical review letters **58**, 12, 1212 (1987).

Emma, P., R. Akre, J. Arthur, R. Bionta, C. Bostedt, J. Bozek, A. Brachmann, P. Bucksbaum, R. Coffee, F.-J. Decker *et al.*, "First lasing and operation of an ångstrom-wavelength free-electron laser", nature photonics **4**, 9, 641–647 (2010).

England, R. J., D. Filippetto, G. Torrisi, A. Bacci, G. D. Valle, D. Mascali, G. S. Mauro, G. Sorbello, P. Musumeci, J. Scheuer, B. Cowan, L. Schachter, Y.-C. Huang, U. Niedermayer, W. D. Kimura, R. Li, R. Ishebeck, E. I. Simakov, P. Hommelhoff and R. L. Byer, "Laser-driven structure-based accelerators", (2022).

England, R. J., R. J. Noble, K. Bane, D. H. Dowell, C.-K. Ng, J. E. Spencer, S. Tantawi, Z. Wu, R. L. Byer, E. Peralta *et al.*, "Dielectric laser accelerators", Reviews of Modern Physics **86**, 4, 1337 (2014).

Faillace, L., "Recent advancements of rf guns", Physics Procedia **52**, 100–109 (2014).

Fann, W., R. Storz, H. Tom and J. Bokor, "Direct measurement of nonequilibrium electron-energy distributions in subpicosecond laser-heated gold films", Physical review letters **68**, 18, 2834 (1992).

Feist, A., N. Bach, N. R. da Silva, T. Danz, M. Möller, K. E. Priebe, T. Domröse, J. G. Gatzmann, S. Rost, J. Schauss *et al.*, "Ultrafast transmission electron microscopy using a laser-driven field emitter: Femtosecond resolution with a high coherence electron beam", Ultramicroscopy **176**, 63–73 (2017).

Feng, J., S. Karkare, J. Nasiatka, S. Schubert, J. Smedley and H. Padmore, "Near atomically smooth alkali antimonide photocathode thin films", Journal of Applied Physics **121**, 4, 044904 (2017).

Feng, J., J. Nasiatka, W. Wan, S. Karkare, J. Smedley and H. A. Padmore, "Thermal limit to the intrinsic emittance from metal photocathodes", Applied Physics Letters **107**, 13, 134101 (2015).

Ferrini, G., F. Banfi, C. Giannetti and F. Parmigiani, "Non-linear electron photoemission from metals with ultrashort pulses", Nuclear Instruments and Methods in Physics Research Section A: Accelerators, Spectrometers, Detectors and Associated Equipment **601**, 1-2, 123–131 (2009).

Ficek, M., K. J. Sankaran, J. Ryl, R. Bogdanowicz, I.-N. Lin, K. Haenen and K. Darowicki, "Ellipsometric investigation of nitrogen doped diamond thin films grown in microwave ch4/h2/n2 plasma enhanced chemical vapor deposition", Applied Physics Letters **108**, 24 (2016).

Filippetto, D., P. Musumeci, R. Li, B. J. Siwick, M. Otto, M. Centurion and J. Nunes, "Ultrafast electron diffraction: Visualizing dynamic states of matter", Reviews of Modern Physics **94**, 4, 045004 (2022).

Filippetto, D. and H. Qian, "Design of a high-flux instrument for ultrafast electron diffraction and microscopy", Journal of Physics B: Atomic, Molecular and Optical Physics **49**, 10, 104003 (2016).

Galdi, A., J. Balajka, W. J. DeBenedetti, L. Cultrera, I. V. Bazarov, M. A. Hines and J. M. Maxson, "Reduction of surface roughness emittance of cs3sb photocathodes grown via codeposition on single crystal substrates", Applied Physics Letters **118**, 24 (2021).

Gevorkyan, G., S. Karkare, S. Emamian, I. Bazarov and H. Padmore, "Effects of physical and chemical surface roughness on the brightness of electron beams from photocathodes", Physical Review Accelerators and Beams **21**, 9, 093401 (2018).

Ghosh, R. R. and A. Dhawan, "Extremely large near-field enhancements in the vicinity of plasmonic nanoantennas on top of bull's eye structures exhibiting the extraordinary transmission of light", Osa Continuum **4**, 1, 193–211 (2021).

Giustino, F., S. G. Louie and M. L. Cohen, "Electron-phonon renormalization of the direct band gap of diamond", Physical review letters **105**, 26, 265501 (2010).

Gliserin, A., *Towards attosecond 4D imaging of atomic-scale dynamics by single-electron diffraction*, Ph.D. thesis, lmu (2014).

Grames, J., R. Suleiman, P. Adderley, J. Clark, J. Hansknecht, D. Machie, M. Poelker and M. Stutzman, “Charge and fluence lifetime measurements of a dc high voltage gaas photogun at high average current”, Physical Review Special Topics-Accelerators and Beams **14**, 4, 043501 (2011).

Gramotnev, D. K. and S. I. Bozhevolnyi, “Plasmonics beyond the diffraction limit”, Nature photonics **4**, 2, 83–91 (2010).

Graves, W., J. Bessuille, P. Brown, S. Carbajo, V. Dolgashev, K.-H. Hong, E. Ihloff, B. Khaykovich, H. Lin, K. Murari *et al.*, “Compact x-ray source based on burst-mode inverse compton scattering at 100 khz”, Physical Review Special Topics-Accelerators and Beams **17**, 12, 120701 (2014).

Graves, W., J. Chen, P. Fromme, M. Holl, R. Kirian, L. Malin, K. Schmidt, J. Spence, M. Underhill, U. Weierstall *et al.*, “Asu compact xfel”, in “Proc. 38th International Free-Electron Laser Conference (FEL’17)”, (2017).

Graves, W., P. Fromme, M. Holl, L. Malin, M. Messerschmidt, E. Nanni, A. Sandhu, S. Tantawi, S. Tilton and J. Spence, “The asu compact xfel project”, Bulletin of the American Physical Society **65** (2020).

Gruner, S. M., D. Bilderback, I. Bazarov, K. Finkelstein, G. Krafft, L. Merminga, H. Padamsee, Q. Shen, C. Sinclair and M. Tigner, “Energy recovery linacs as synchrotron radiation sources”, Review of Scientific Instruments **73**, 3, 1402–1406 (2002).

Gujrati, A., A. Sanner, S. R. Khanal, N. Moldovan, H. Zeng, L. Pastewka and T. D. Jacobs, “Comprehensive topography characterization of polycrystalline diamond coatings”, Surface Topography: Metrology and Properties **9**, 1, 014003 (2021).

Guo, Z., Z. Li, J. Zhang, K. Guo, F. Shen, Q. Zhou and H. Zhou, “Review of the functions of archimedes’ spiral metallic nanostructures”, Nanomaterials **7**, 11, 405 (2017).

Harniman, R. L., O. J. Fox, W. Janssen, S. Drijkoningen, K. Haenen and P. W. May, “Direct observation of electron emission from grain boundaries in cvd diamond by peakforce-controlled tunnelling atomic force microscopy”, Carbon **94**, 386–395 (2015).

Harrison, M., S. Peggs and T. Roser, “The rhic accelerator”, Annual Review of Nuclear and Particle Science **52**, 1, 425–469 (2002).

Hirano, T., K. E. Urbanek, A. C. Ceballos, D. S. Black, Y. Miao, R. Joel England, R. L. Byer and K. J. Leedle, “A compact electron source for the dielectric laser accelerator”, Applied Physics Letters **116**, 16 (2020).

Holzer, B., “Introduction to particle accelerators and their limitations”, arXiv preprint arXiv:1705.09601 (2017).

Huang, C., H. Andrews, R. Baker, R. Fleming, D. Kim, T. Kwan, V. Pavlenko, A. Piryatinski, E. Simakov *et al.*, “Physics of electron beam generation and dynamics from diamond field emitter arrays”, in “Proceedings of 10th Int. Particle Accelerator Conf.”, pp. 2137–2139 (2019a).

Huang, C.-K., H. L. Andrews, R. C. Baker, R. L. Fleming, D. Kim, T. J. Kwan, A. Piryatinski, V. Pavlenko and E. I. Simakov, “Modeling of diamond field emitter arrays for a compact source of high brightness electron beams”, Journal of Applied Physics **125**, 16 (2019b).

Huang, J., Y. Liu, S. Jin, Z. Wang, Y. Qi, J. Zhang, K. Wang and R. Qiu, “Uniformity control of laser-induced periodic surface structures”, Frontiers in Physics **10**, 932284 (2022).

Ischenko, A., V. Golubkov, V. Spiridonov, A. Zgurskii, A. Akhmanov, M. Vabischevich and V. Bagratashvili, “A stroboscopical gas-electron diffraction method for the investigation of short-lived molecular species”, Applied Physics B **32**, 161–163 (1983).

Ischenko, A. A., L. Schafer, J. Y. Luo and J. D. Ewbank, “Structural and vibrational kinetics by stroboscopic gas electron diffraction: The 193 nm photodissociation of cs2”, The Journal of Physical Chemistry **98**, 35, 8673–8678 (1994).

Jarvis, J. D., H. Andrews, B. Ivanov, C. Stewart, N. De Jonge, E. Heeres, W.-P. Kang, Y.-M. Wong, J. Davidson and C. Brau, “Resonant tunneling and extreme brightness from diamond field emitters and carbon nanotubes”, Journal of Applied Physics **108**, 9 (2010).

Ji, F., D. B. Durham, A. M. Minor, P. Musumeci, J. G. Navarro and D. Filippetto, “Ultrafast relativistic electron nanoprobes”, Communications Physics **2**, 1, 54 (2019).

Johnson, P. B. and R.-W. Christy, “Optical constants of the noble metals”, Physical review B **6**, 12, 4370 (1972).

Kachwala, A., R. Ahsan, P. Bhattacharyya, H. U. Chae, O. Chubenko, R. Kapadia, S. Karkare and P. Saha, “Photonics-Integrated Photocathodes”, JACoW **IPAC2023**, TUPL189 (2023a).

Kachwala, A., R. Ahsan, H. Chae, O. Chubenko, R. Kapadia and S. Karkare, “On-Chip Photonics Integrated Photocathodes”, in “Proc. NAPAC’22”, No. 5 in International Particle Accelerator Conference, pp. 767–769 (JACoW Publishing, Geneva, Switzerland, 2022a), URL `https://jacow.org/napac2022/papers/wepa65.pdf`.

Kachwala, A., O. Chubenko, D. Kim, E. Simakov and S. Karkare, “Quantum efficiency, photoemission energy spectra, and mean transverse energy of ultrananocrystalline diamond photocathode”, Journal of Applied Physics **132**, 22 (2022b).

Kachwala, A., O. Chubenko, D. Kim, E. Simakov and S. Karkare, “Ultrafast laser triggered electron emission from ultrananocrystalline diamond pyramid tip cathode”, Journal of Applied Physics **135**, 12 (2024).

Kachwala, A., P. Saha, P. Bhattacharyya, E. Montgomery, O. Chubenko and S. Karkare, “Demonstration of thermal limit mean transverse energy from cesium antimonide photocathodes”, Applied Physics Letters **123**, 4 (2023b).

Karkare, S., G. Adhikari, W. A. Schroeder, J. K. Nangoi, T. Arias, J. Maxson and H. Padmore, “Ultracold electrons via near-threshold photoemission from single-crystal cu (100)”, Physical review letters **125**, 5, 054801 (2020).

Karkare, S. and I. Bazarov, "Effects of surface nonuniformities on the mean transverse energy from photocathodes", Physical Review Applied **4**, 2, 024015 (2015).

Karkare, S., L. Boulet, L. Cultrera, B. Dunham, X. Liu, W. Schaff and I. Bazarov, "Ultrabright and ultrafast iii–v semiconductor photocathodes", Physical review letters **112**, 9, 097601 (2014).

Karkare, S., D. Dimitrov, W. Schaff, L. Cultrera, A. Bartnik, X. Liu, E. Sawyer, T. Esposito and I. Bazarov, "Monte carlo charge transport and photoemission from negative electron affinity gaas photocathodes", Journal of Applied Physics **113**, 10, 104904 (2013).

Karkare, S., J. Feng, J. Maxson and H. Padmore, "Development of a 3-d energy-momentum analyzer for mev-scale energy electrons", Review of Scientific Instruments **90**, 5 (2019).

Kawata, S., *Near-field optics and surface plasmon polaritons*, vol. 81 (Springer Science & Business Media, 2001).

Kealhofer, C., S. M. Foreman, S. Gerlich and M. A. Kasevich, "Ultrafast laser-triggered emission from hafnium carbide tips", Physical Review B **86**, 3, 035405 (2012).

Kim, D., H. L. Andrews, B. K. Choi, R. L. Fleming, C.-K. Huang, T. J. Kwan, J. Lewellen, K. Nichols, V. Pavlenko and E. I. Simakov, "Divergence study and emittance measurements for the electron beam emitted from a diamond pyramid", Nuclear Instruments and Methods in Physics Research Section A: Accelerators, Spectrometers, Detectors and Associated Equipment **953**, 163055 (2020a).

Kim, D., H. L. Andrews, B. K. Choi and E. I. Simakov, "Fabrication of micron-scale diamond field emitter arrays for dielectric laser accelerators", in "2018 IEEE Advanced Accelerator Concepts Workshop (AAC)", pp. 1–3 (IEEE, 2018).

Kim, H. W., N. A. Vinokurov, I. H. Baek, K. Y. Oang, M. H. Kim, Y. C. Kim, K.-H. Jang, K. Lee, S. H. Park, S. Park *et al.*, "Towards jitter-free ultrafast electron diffraction technology", Nature photonics **14**, 4, 245–249 (2020b).

Kirchner, F., *Ultrashort and coherent single-electron pulses for diffraction at ultimate resolutions*, Ph.D. thesis, lmu (2013).

Knill, C., S. Karkare, H. Padmore *et al.*, "Near-threshold nonlinear photoemission from cu (100)", in "12th International Particle Accelerator Conference (IPAC'21), Campinas, SP, Brazil, 24-28 May 2021", pp. 2822–2825 (JACOW Publishing, Geneva, Switzerland, 2021).

Knill, C. J., "Practical limitations of low mean transverse energy metallic photocathodes", Tech. rep., Arizona State University (2023).

Knill, C. J., S. Douyon, K. Kawahara, H. Yamaguchi, G. Wang, H. Ago, N. Moody and S. Karkare, "Effects of nonlinear photoemission on mean transverse energy from metal photocathodes", Phys. Rev. Accel. Beams **26**, 093401, URL `https://link.aps.org/doi/10.1103/PhysRevAccelBeams.26.093401` (2023a).

Knill, C. J., H. Yamaguchi, K. Kawahara, G. Wang, E. Batista, P. Yang, H. Ago, N. Moody and S. Karkare, "Near-threshold photoemission from graphene-coated cu (110)", Physical Review Applied **19**, 1, 014015 (2023b).

Knill, C. J., H. Yamaguchi, K. Kawahara, G. Wang, E. Batista, P. Yang, H. Ago, N. Moody and S. Karkare, "Near-threshold photoemission from graphene-coated Cu(110)", Phys. Rev. Appl. **19**, 014015, URL `https://link.aps.org/doi/10.1103/PhysRevApplied.19.014015` (2023c).

Krüger, J., D. Dufft, R. Koter and A. Hertwig, "Femtosecond laser-induced damage of gold films", Applied surface science **253**, 19, 7815–7819 (2007).

Krüger, M., *Attosecond physics in strong-field photoemission from metal nanotips*, Ph.D. thesis, lmu (2013).

Kupratakuln, S., "Relativistic electron band structure of gold", Journal of Physics C: Solid State Physics **3**, 2S, S109 (1970).

Larson, D., "Electron cooling for a muon collider", (2011).

Lessner, E., X. Wang and P. Musumeci, "Future of electron sources", US Department of Energy, Washington, DC (United States) (2017).

Li, R., K. Roberts, C. Scoby, H. To and P. Musumeci, "Nanometer emittance ultralow charge beams from rf photoinjectors", Physical Review Special Topics-Accelerators and Beams **15**, 9, 090702 (2012).

Li, W., C. Duncan, M. Andorf, A. Bartnik, E. Bianco, L. Cultrera, A. Galdi, M. Gordon, M. Kaemingk, C. Pennington *et al.*, "A kiloelectron-volt ultrafast electron micro-diffraction apparatus using low emittance semiconductor photocathodes", Structural Dynamics **9**, 2 (2022).

Liu, L., X. Ouyang, J. Zhang, X. Zhang and Y. Zhong, "Polycrystalline cvd diamond detector: Fast response and high sensitivity with large area", AIP Advances **4**, 1, 017114 (2014).

Maxson, J., P. Musumeci, L. Cultrera, S. Karkare and H. Padmore, "Ultrafast laser pulse heating of metallic photocathodes and its contribution to intrinsic emittance", Nuclear Instruments and Methods in Physics Research Section A: Accelerators, Spectrometers, Detectors and Associated Equipment **865**, 99–104 (2017).

McDonald, K. and D. Russell, "Methods of emittance measurement", in "Frontiers of Particle Beams; Observation, Diagnosis and Correction: Proceedings of a Topical Course Held by the Joint US-CERN School on Particle Accelerators at Anacapri, Isola di Capri, Italy, October 20–26, 1988", pp. 122–132 (Springer, 2005).

McNeur, J., M. Kozák, N. Schönenberger, K. J. Leedle, H. Deng, A. Ceballos, H. Hoogland, A. Ruehl, I. Hartl, R. Holzwarth *et al.*, "Elements of a dielectric laser accelerator", Optica **5**, 6, 687–690 (2018).

Meier, S., J. Heimerl and P. Hommelhoff, “Few-electron correlations after ultrafast photoemission from nanometric needle tips”, Nature Physics **19**, 10, 1402–1409 (2023).

Mengui, U., R. Campos, K. Alves, E. Antunes, M. Hamanaka, E. Corat and M. Baldan, “Combined effect of nitrogen doping and nanosteps on microcrystalline diamond films for improvement of field emission”, Applied Surface Science **334**, 222–226 (2015).

Musumeci, P., L. Cultrera, M. Ferrario, D. Filippetto, G. Gatti, M. Gutierrez, J. Moody, N. Moore, J. Rosenzweig, C. Scoby *et al.*, “Multiphoton photoemission from a copper cathode illuminated by ultrashort laser pulses in an rf photoinjector”, Physical review letters **104**, 8, 084801 (2010).

Musumeci, P., J. G. Navarro, J. Rosenzweig, L. Cultrera, I. Bazarov, J. Maxson, S. Karkare and H. Padmore, “Advances in bright electron sources”, Nuclear Instruments and Methods in Physics Research Section A: Accelerators, Spectrometers, Detectors and Associated Equipment **907**, 209–220 (2018).

Naguib, N. N., J. W. Elam, J. Birrell, J. Wang, D. S. Grierson, B. Kabius, J. M. Hiller, A. V. Sumant, R. W. Carpick, O. Auciello *et al.*, “Enhanced nucleation, smoothness and conformality of ultrananocrystalline diamond (uncd) ultrathin films via tungsten interlayers”, Chemical Physics Letters **430**, 4-6, 345–350 (2006).

Nangoi, J., M. Gaowei, A. Galdi, J. Maxson, S. Karkare, J. Smedley and T. Arias, “Ab initio study of the crystal and electronic structure of mono-and bi-alkali antimonides: Stability, goldschmidt-like tolerance factors, and optical properties”, arXiv preprint arXiv:2205.14322 (2022).

Nichols, K., H. L. Andrews, D. Kim, E. I. Simakov, M. Conde, D. S. Doran, G. Ha, W. Liu, J. Power, J. Shao *et al.*, “Demonstration of transport of a patterned electron beam produced by diamond pyramid cathode in an rf gun”, Applied Physics Letters **116**, 2, 023502 (2020).

Nitti, M., M. Colasuonno, E. Nappi, A. Valentini, E. Fanizza, F. Bénédic, G. Cicala, E. Milani and G. Prestopino, “Performance analysis of poly-, nano-and single-crystalline diamond-based photocathodes”, Nuclear Instruments and Methods in Physics Research Section A: Accelerators, Spectrometers, Detectors and Associated Equipment **595**, 1, 131–135 (2008).

Parzyck, C., A. Galdi, J. Nangoi, W. DeBenedetti, J. Balajka, B. Faeth, H. Paik, C. Hu, T. Arias, M. Hines *et al.*, “Single-crystal alkali antimonide photocathodes: High efficiency in the ultrathin limit”, Physical Review Letters **128**, 11, 114801 (2022a).

Parzyck, C. T., A. Galdi, J. K. Nangoi, W. J. I. DeBenedetti, J. Balajka, B. D. Faeth, H. Paik, C. Hu, T. A. Arias, M. A. Hines, D. G. Schlom, K. M. Shen and J. M. Maxson, “Single-crystal alkali antimonide photocathodes: High efficiency in the ultrathin limit”, Phys. Rev. Lett. **128**, 114801, URL `https://link.aps.org/doi/10.1103/PhysRevLett.128.114801` (2022b).

Pavlenko, V., H. Andrews, D. Gorelov, R. Fleming, D. Kim, E. Simakov, K. Leedle and D. Black, “Characterization of femtosecond-laser-induced electron emission from diamond nano-tips”, in “North American Particle Accelerator Conference (NAPAC’19), Lansing, MI, USA, 01-06 September 2019”, pp. 228–231 (JACOW Publishing, Geneva, Switzerland, 2019).

Pavlenko, V., D. Kim, H. L. Andrews, D. V. Gorelov and E. I. Simakov, “Strong-field photoemission experiment using diamond field emitter arrays”, arXiv preprint arXiv:2107.00128 (2021).

Pérez Quintero, K. J., S. Antipov, A. V. Sumant, C. Jing and S. V. Baryshev, “High quantum efficiency ultrananocrystalline diamond photocathode for photoinjector applications”, Applied Physics Letters **105**, 12, 123103 (2014).

Pierce, C. M., B. Daniel, A. Kachwala, S. Karkare, I. Bazarov, J. Maxson, A. M. Minor *et al.*, “Towards high brightness from plasmon-enhanced photoemitters”, in “Proceedings of the 5th North American Particle Accelerator Conference”, (2022).

Pierce, C. M., D. B. Durham, F. Riminucci, S. Dhuey, I. Bazarov, J. Maxson, A. M. Minor and D. Filippetto, “Experimental characterization of photoemission from plasmonic nanogroove arrays”, Physical Review Applied **19**, 3, 034034 (2023).

Pinault, M.-A., J. Barjon, T. Kociniewski, F. Jomard and J. Chevallier, “The n-type doping of diamond: present status and pending questions”, Physica B: Condensed Matter **401**, 51–56 (2007).

Power, J., “Overview of photoinjectors”, in “AIP Conference Proceedings”, vol. 1299, pp. 20–28 (American Institute of Physics, 2010).

Qian, H., C. Li, Y. Du, L. Yan, J. Hua, W. Huang and C. Tang, “Experimental investigation of thermal emittance components of copper photocathode”, Physical Review Special Topics-Accelerators and Beams **15**, 4, 040102 (2012).

Ramchandani, M., “Energy band structure of gold”, Journal of Physics C: Solid State Physics **3**, 1S, S1 (1970).

Rangel, T., D. Kecik, P. Trevisanutto, G.-M. Rignanese, H. Van Swygenhoven and V. Olevano, “Band structure of gold from many-body perturbation theory”, Physical Review B **86**, 12, 125125 (2012).

Rani, R., K. Panda, N. Kumar, K. A. Titovich, K. V. Ivanovich, S. A. Vyacheslavovich and I.-N. Lin, “Tribological properties of ultrananocrystalline diamond films: mechanochemical transformation of sliding interfaces”, Scientific reports **8**, 1, 1–16 (2018).

Reutzel, M., A. Li and H. Petek, “Above-threshold multiphoton photoemission from noble metal surfaces”, Physical Review B **101**, 7, 075409 (2020).

Russell, S. J., “Overview of high-brightness, high-average-current photoinjectors for fels”, in “Free Electron Lasers 2002”, pp. 304–309 (Elsevier, 2003).

Saha, P., O. Chubenko, G. Gevorkyan, A. Kachwala, S. Karkare, C. Knill, E. Montgomery, H. Padmore, S. Poddar *et al.*, "Optical and surface characterization of alkali-antimonide photocathodes", in "12th International Particle Accelerator Conference (IPAC'21), Campinas, SP, Brazil, 24-28 May 2021", pp. 4037–4040 (JACOW Publishing, Geneva, Switzerland, 2021).

Saha, P., O. Chubenko, G. S. Gevorkyan, A. Kachwala, C. J. Knill, C. Sarabia-Cardenas, E. Montgomery, S. Poddar, J. T. Paul, R. G. Hennig *et al.*, "Physically and chemically smooth cesium-antimonide photocathodes on single crystal strontium titanate substrates", Applied Physics Letters **120**, 19, 194102 (2022).

Saha, P., O. Chubenko, J. Kevin Nangoi, T. Arias, E. Montgomery, S. Poddar, H. A. Padmore and S. Karkare, "Theory of photoemission from cathodes with disordered surfaces", Journal of Applied Physics **133**, 5 (2023).

Sakata, T., "Studies on the cs3sb photo-cathode", Journal of the Physical Society of Japan **8**, 6, 723–730 (1953).

Schneider, M. E., *Advancing Field Emission Technology for High Power Injectors Operating in GHz and Beyond*, Ph.D. thesis, Michigan State University (2022).

Sciaini, G. and R. D. Miller, "Femtosecond electron diffraction: heralding the era of atomically resolved dynamics", Reports on Progress in Physics **74**, 9, 096101 (2011).

Shamsa, M., S. Ghosh, I. Calizo, V. Ralchenko, A. Popovich and A. Balandin, "Thermal conductivity of nitrogenated ultrananocrystalline diamond films on silicon", Journal of Applied Physics **103**, 8 (2008).

Shen, L. and Z. Chen, "An investigation of grain size and nitrogen-doping effects on the mechanical properties of ultrananocrystalline diamond films", International Journal of Solids and Structures **44**, 10, 3379–3392 (2007).

Siddiqui, K., D. Durham, F. Cropp, F. Ji, S. Paiagua, C. Ophus, N. Andresen, L. Jin, J. Wu, S. Wang *et al.*, "Relativistic ultrafast electron diffraction at high repetition rates", arXiv preprint arXiv:2306.04900 (2023).

Silari, M., "Applications of particle accelerators in medicine", Radiation protection dosimetry **146**, 4, 440–450 (2011).

Silfies, J. S., S. A. Schwartz and M. W. Davidson, "The diffraction barrier in optical microscopy", Nikon Inc.,[Online]. Available: https://www. microscopyu. com/articles/superresolution/diffractionbarrier. html.[Accessed 28. 10. 2015] (2019).

Simakov, E., H. Andrews, R. Fleming, D. Kim, V. Pavlenko, D. Black and K. Leedle, "Observations of the femtosecond laser-induced emission from the diamond field emitter tips", in "10th Int. Particle Accelerator Conf.(IPAC'19), Melbourne, Australia", (2019).

Simakov, E. I., H. L. Andrews, M. J. Herman, K. M. Hubbard and E. Weis, "Diamond field emitter array cathodes and possibilities of employing additive manufacturing for dielectric laser accelerating structures", in "AIP Conference Proceedings", vol. 1812 (AIP Publishing, 2017).

Smedley, J., M. Gaowei, J. Sinsheimer, K. Attenkofer, J. Walsh, J. Kuhn, E. Muller, Z. Ding, H. Frisch, H. Bhandari *et al.*, "Sputter growth of alkali antimonide photocathodes: an in operando materials analysis", in "Proceeding of the 2015 International Particle Accelerator Conference", (2015).

Sood, A., X. Shen, Y. Shi, S. Kumar, S. J. Park, M. Zajac, Y. Sun, L.-Q. Chen, S. Ramanathan, X. Wang *et al.*, "Universal phase dynamics in vo2 switches revealed by ultrafast operando diffraction", Science **373**, 6552, 352–355 (2021).

Soomary, L., D. Juarez-Lopez, C. Welsch, L. Jones and T. Noakes, "Performance characterisation of a cu (100) single–crystal photocathode", in "Proceedings of IPAC 2021 conference, Campinas, Brazil", pp. 2860–2862 (2021).

Spicer, W. E., "Photoemissive, photoconductive, and optical absorption studies of alkali-antimony compounds", Physical review **112**, 1, 114 (1958).

Sprangle, P., G. Joyce, E. Esarey and A. Ting, "Laser wakefield acceleration and relativstic optical guiding", in "AIP Conference Proceedings", vol. 175, pp. 231–239 (American Institute of Physics, 1988).

Stratton, R., "Theory of field emission from semiconductors", Physical Review **125**, 1, 67 (1962).

Suleiman, R., P. Adderley, J. Grames, J. Hansknecht, M. Poelker and M. Stutzman, "High current polarized electron source", in "AIP Conference Proceedings", vol. 1970, p. 050007 (AIP Publishing LLC, 2018).

Sun, T., F. A. Koeck, C. Zhu and R. J. Nemanich, "Combined visible light photo-emission and low temperature thermionic emission from nitrogen doped diamond films", Applied Physics Letters **99**, 20, 202101 (2011).

Tafel, A., S. Meier, J. Ristein and P. Hommelhoff, "Femtosecond laser-induced electron emission from nanodiamond-coated tungsten needle tips", Physical Review Letters **123**, 14, 146802 (2019).

Tajima, T., X. Yan and T. Ebisuzaki, "Wakefield acceleration", Reviews of Modern Plasma Physics **4**, 1–72 (2020).

Tan, S., A. Argondizzo, J. Ren, L. Liu, J. Zhao and H. Petek, "Plasmonic coupling at a metal/semiconductor interface", Nature Photonics **11**, 12, 806–812 (2017).

Tóth, S., J. Budai, M. Veres and M. Koós, "Optical properties of nano-and ultrananocrystalline diamond thin layers in the uv and visible spectral range", in "IOP Conference Series: Materials Science and Engineering", vol. 426, p. 012049 (IOP Publishing, 2018).

van der Weide, J., Z. Zhang, P. Baumann, M. Wensell, J. Bernholc and R. Nemanich, "Negative-electron-affinity effects on the diamond (100) surface", Physical Review B **50**, 8, 5803 (1994).

Vecchione, T., D. Dowell, W. Wan, J. Feng and H. Padmore, "Quantum efficiency and transverse momentum from metals", Proc. of FEL2013 pp. p–424 (2013).

Weathersby, S., G. Brown, M. Centurion, T. Chase, R. Coffee, J. Corbett, J. Eichner, J. Frisch, A. Fry, M. Gühr *et al.*, "Mega-electron-volt ultrafast electron diffraction at slac national accelerator laboratory", Review of Scientific Instruments **86**, 7 (2015).

Wen-Xi, L., Z. Peng-Fei, W. Xuan, N. Shou-Hua, Z. Zhong-Chao, C. Rick, C. Jian-Ming, S. Zheng-Ming and Z. Jie, "Ultrafast electron diffraction with spatiotemporal resolution of atomic motion", Chinese Physics Letters **26**, 2, 020701 (2009).

Wootton, K. P., Z. Wu, B. M. Cowan, A. Hanuka, I. V. Makasyuk, E. A. Peralta, K. Soong, R. L. Byer and R. J. England, "Demonstration of acceleration of relativistic electrons at a dielectric microstructure using femtosecond laser pulses", Optics letters **41**, 12, 2696–2699 (2016).

Wort, C. J. and R. S. Balmer, "Diamond as an electronic material", Materials today **11**, 1-2, 22–28 (2008).

Yuan, W., L. Fang, Z. Feng, Z. Chen, J. Wen, Y. Xiong and B. Wang, "Highly conductive nitrogen-doped ultrananocrystalline diamond films with enhanced field emission properties: triethylamine as a new nitrogen source", Journal of Materials Chemistry C **4**, 21, 4778–4785 (2016).

Zhang, Z. and C. Tang, "Analytical study on emittance growth caused by roughness of a metallic photocathode", Physical Review Special Topics-Accelerators and Beams **18**, 5, 053401 (2015).

Zhu, T., Y. Hu, P. Gatkine, S. Veilleux, J. Bland-Hawthorn and M. Dagenais, "Ultrabroadband high coupling efficiency fiber-to-waveguide coupler using si _{3} n _{4}/sio _{2} waveguides on silicon", IEEE Photonics Journal **8**, 5, 1–12 (2016).

APPENDIX A

MATHEMATICAL FUNCTIONS

In this section I summarize some equations and functions which were used to determine the resolution of the PEEM instrument when operated in the real space mode, k-space mode and that of the energy spectra obtained using imaging energy filter capability of the PEEM.

Gauss-Step Funtion

The resolution of the PEEM image in real space and k-space mode was determined using the convolution of the Heaviside step and the Gaussian function. The Gaussian function is represented as,

$$G(x) = \frac{1}{\sqrt{2\pi}\sigma} \exp \frac{-x^2}{2\sigma^2} \tag{A.1}$$

Here, standard deviation σ, represents the resolution of the microscope For the rising edge, the Heaviside step function is represented by,

$$H(x) = \left\{ \begin{array}{ll} 0, & \text{for } x < b \\ 1, & \text{for } x \geq b \end{array} \right. \tag{A.2}$$

and for the falling edge, the Heaviside step function is represented by,

$$H(x) = \left\{ \begin{array}{ll} 1, & \text{for } x < b \\ 0, & \text{for } x \geq b \end{array} \right. \tag{A.3}$$

The convolution of the Heaviside step function (with step height, I_0, and at position x=b) with the Gaussian function is given by,

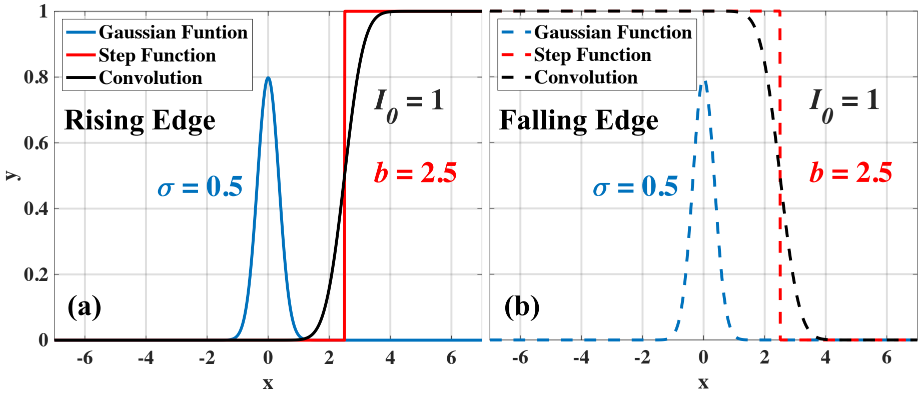

Figure A.1: The convolution of the Heaviside step function and the Gaussian function resulting in error function which is used to determine the resolution of the PEEM instrument when operated in the real space and k-space mode.

$$C(x) = I_0 \int_{-\infty}^{\infty} H(t-b)G(x-t)\,dt = \left\{ \begin{array}{ll} \frac{I_0}{2}\left(1 + erf\left(\frac{x+b}{\sqrt{2}\sigma}\right)\right), & \text{for } \textit{Rising Edge} \\ \frac{I_0}{2}\left(1 - erf\left(\frac{x-b}{\sqrt{2}\sigma}\right)\right), & \text{for } \textit{Falling Edge} \end{array} \right. \tag{A.4}$$

All four functions are plotted in figure A.1 for exemplary case ($I_0 = 1$, $\sigma = 0.5$ and $b = 2.5$). An example for use of the above functions is shown in Fig. 2.4 (d-e)

Spectral Fit Function

The energy resolution of the photoemission spectrum is determined by fitting a function S(x).

$$S(x) = \frac{I_0}{4}\left(1 + erf\left(\frac{x + b_{wr}}{\sqrt{2}\sigma_{wr}}\right)\right)\left(1 - erf\left(\frac{x - b_{wf}}{\sqrt{2}\sigma_{wf}}\right)\right) \tag{A.5}$$

Here, the subscripts *wr* and *wf* correspond to the *rising* and the *falling* edge of the photoemision spectra. An example for use of this function is shown in Fig. 2.7 (b-c)

APPENDIX B

SUPPLEMENTARY INFORMATION FOR CHAPTER SIX

Tilt-Compensation

The characterization of Archimedean spiral photocathode (ASP) was performed using commercially available photoemission electron microscope (PEEM) [Foc (2024)]. This commercially available PEEM set up has the capability of 4° angle of incidence. The design of ASP was compensated for this 4° angle of incidence. Figure B.1 (a) shows the simplified in-plane (x-y) schematic of the Archimedean spiral geometry. Figure B.1 (b) shows the simplified cross-sectional (x-z) schematic of the Archimedean spiral geometry. Generalizing for incidence angle θ, from Fig. B.1 (b), we can write [Durham *et al.* (2021)]:

$$\frac{\Delta p}{c} = \frac{\Delta r}{v_{spp}}, \tag{B.1}$$

Here, Δp is the path difference of the incident laser pulse due to the angle of incidence (θ), Δr is the path travelled by the surface plasmon polariton, c is the speed of light and v_{spp} is the speed of surface plasmon polariton. In terms of wavelength, from Fig. B.1 (b), equation B.1 can be written as [Kawata (2001)]:

$$\Delta r = \frac{\Delta x sin(\theta)\lambda_{spp}}{\lambda}, \tag{B.2}$$

Here λ_{spp} = 783 nm and λ = 800 nm. From equation B.2, the tilt-compensation equation for ASP in Cartesian form can be written as:

$$x' = rcos(\phi) + rcos(\phi)sin(\theta)\frac{\lambda_{spp}}{\lambda}cos(\phi) \tag{B.3}$$

$$y' = rsin(\phi) + rcos(\phi)sin(\theta)\frac{\lambda_{spp}}{\lambda}sin(\phi) \tag{B.4}$$

Here, x' and y' are the transformed Cartesian co-ordinates for the tilt compensated spiral. Figure B.2 shows the comparison between symmetric spiral and the transformed spiral which accounts for tilt compensation θ = 4°.

Finite Difference Time Domain Simulation

To determine the optimal ASP structure, 3D finite-difference time domain (FDTD) simulations were performed using a commercial software suite (Lumerical) [Lum (2024)]. The simulated structure reported here provides an optimal balance between high optical performance and ease of fabrication. Tilt compensated spiral with thickness of 120 nm and starting radius R_0 = 12.5 μm was designed with silicon as the substrate. The ASP consisted of a single groove that completes nine revolutions around the ASP center to maximize the SPP excitation efficiency beyond which the increase in intensity enhancement is minimal. The optical constants of gold was taken from Johnson and Christy [Johnson and Christy (1972)]. Circularly polarized Gaussian pulse with a pulse length of 150 fs and central wavelength of 800 nm was made incident at 4° angle of incidence. Figure 1 (a) shows the intensity enhancement due to surface plasmon polariton (SPP) focus at the center of ASP calculated using FDTD simulation. The intensity(I) enhancement was calculated as I_{max}/I_0, where I_{max} is the maximum intensity in the measurement plane and I_0 is the

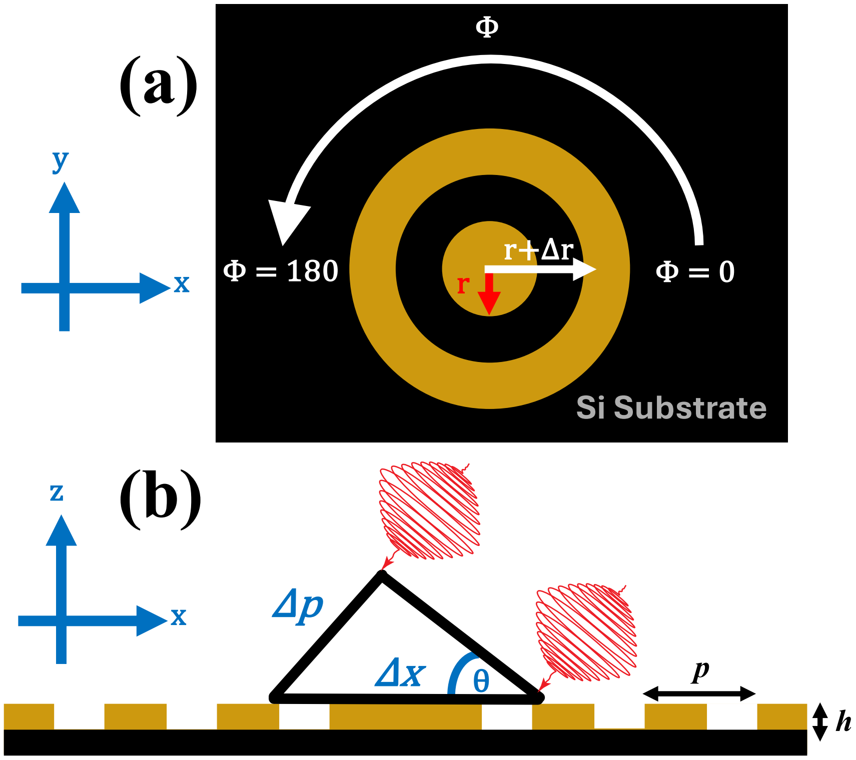

Figure B.1: (a) Simplified in-plane (x-y) and (b) cross-sectional (x-z) schematic of the Archimedean spiral geometry. Here p is the pitch of the spiral and it varies according to equation B.3 and B.4. h =120 nm is the thickness of gold layer on the silicon (Si) substrate.

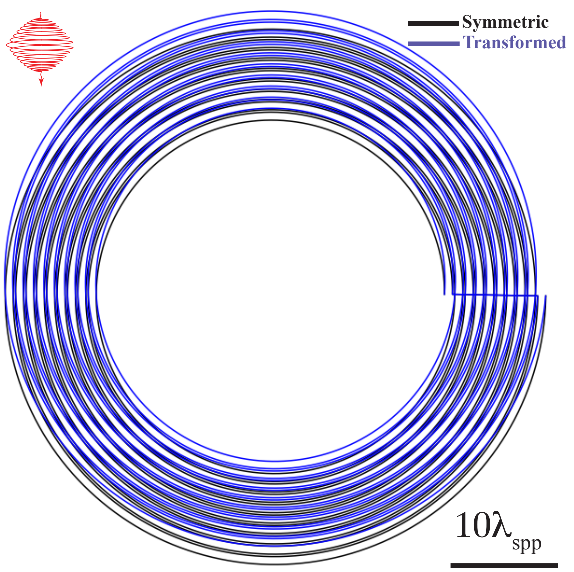

Figure B.2: Comparison between symmetric and the transformed Archimedean spiral which accounts for tilt compensation θ = 4°. Here λ_{spp} = 783 nm.

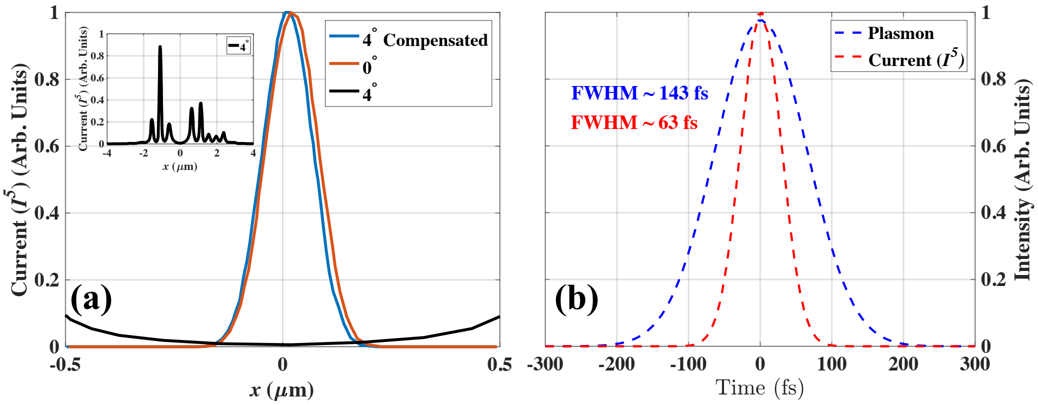

Figure B.3: FDTD simulation showing (a) Current enhancement considering 5^{th} order non-linearity in the electron emission process. The blue solid curve shows the current profile for compensated spiral as per equation B.3 and B.4 with $\theta = 4°$. The red solid curve shows the current profile for uncompensated spiral with $\theta = 0°$ and the black curve shows the current profile for uncompensated spiral with $\theta = 4°$. The inset of the figure shows the expanded x-axis showing the current profile for uncompensated spiral with $\theta = 4°$. (b) Time response of ASP to a 150 fs excitation computed with FDTD (plasmon). Estimated current profile considering 5^{th} order non-linearity in the electron emission process.

maximum intensity of the incoming excitation pulse. The spatial extent of the electron emission considering 5^{th} order non-linearity for compensated and uncompensated spiral designed using equation B.3 and B.4 is shown in Fig. B.3 (a). The time response of electron emission was considering 5^{th} order non-linearity in the electron emission process as shown in Fig. B.3 (b). Perfectly matched layers were used for all the boundaries.

APPENDIX C

AUTHOR’S DECLARATION

The work presented in Chapter 3 was originally published as Kachwala *et al.* (2022b). The work presented in Chapter 4 was originally published as Kachwala *et al.* (2023b). The work presented in Chapter 5 was originally published as Kachwala *et al.* (2024). For the work presented in Chapter 6, the manuscript is currently under preparation with plans to submit to a journal. For the work presented in Chapter 7, the manuscript is currently under preparation with plans to submit to a journal, and parts of it has been published in conference proceedings as Kachwala *et al.* (2023a). I have obtained permission from all coauthors of these works to submit the contents of the publications as chapters of this dissertation.